E.O. Paton Electric Welding Institute of the National Academy of Science of Ukraine
International Association “Welding”

The Paton Welding Journal

01
2025

International Scientific-Technical and Production Journal ♦ Founded in January 2000 (12 Issues Per Year)

EDITORIAL BOARD

Editor-in-Chief
Igor Krivtsun
E.O. Paton Electric Welding Institute of the NASU, Kyiv, Ukraine

Deputy Editor-in-Chief
Michael Gasik
Aalto University, Espoo, Finland

Deputy Editor-in-Chief
Jacob Kleiman
Integrity Testing Laboratory, Markham, Canada

Editorial Board Members

Serhii Akhonin
E.O. Paton Electric Welding Institute of the NASU, Kyiv, Ukraine

Chunlin Dong
Guangzhou Jiao Tong University, China

Shiyi Gao
China-Ukraine Institute of Welding,
Guangdong Academy of Sciences, Guangzhou, China

Len Gelman
The University of Huddersfield, UK

Andrey Gumenyuk
Bundesanstalt für Materialforschung und –prüfung (BAM),
Berlin, Germany

Vitalii Knysh
E.O. Paton Electric Welding Institute of the NASU, Kyiv, Ukraine

Volodymyr Korzhyk
E.O. Paton Electric Welding Institute of the NASU, Kyiv, Ukraine

Victor Kvasnytskyi
NTUU «Igor Sikorsky Kyiv Polytechnic Institute», Ukraine

Yuliia Kvasnytska
Physico-Technological Institute of Metals and Alloys
of the NASU, Kyiv, Ukraine

Leonid Lobanov
E.O. Paton Electric Welding Institute of the NASU, Kyiv, Ukraine

Eric Macdonald
The University of Texas at El Paso, USA

Anatoliy Maistrenko
V. Bakul Institute for Superhard Materials
of the NASU, Kyiv, Ukraine

Serhiy Maksymov
E.O. Paton Electric Welding Institute of the NASU, Kyiv, Ukraine

Dhanesh G. Mohan
School of Engineering University of Sunderland England,
United Kingdom

João Pedro Oliveira
Universidade NOVA de Lisboa, Portugal

Valerii Peremitko
Dniprovsky State Technical University, Kamianske, Ukraine

Valeriy Pozniakov
E.O. Paton Electric Welding Institute of the NASU, Kyiv, Ukraine

Uwe Reisgen
Welding and Joining Institute, Aachen, Germany

Massimo Rogante
Rogante Engineering, Civitanova Marche, Italy

Cezary Senderowski
Mechanics and Printing Institute, Warsaw University
of Technology, Poland

Magdalena Speicher
Kempten University of Applied Sciences, Germany

Mattias Thuvander
Chalmers University of Technology, Goteborg, Sweden

Valentyn Uchanin
Karpenko Physico-Mechanical Institute of the NASU, Lviv, Ukraine

Gerald Wilhelm
University of Applied Sciences of Munich, Germany

Yongqiang Yang
South China University of Technology, Guangzhou, China

Executive Editor
Oleksandr Zelnichenko
International Association “Welding”, Kyiv, Ukraine

Address of Editorial Office
E.O. Paton Electric Welding Institute, 11 Kazymyr Malevych Str., 03150, Kyiv, Ukraine
Tel.: (38044) 205 23 90, E-mail: patonpublishinghouse@gmail.com; journal@paton.kiev.ua
https://patonpublishinghouse.com/eng/journals/tpwj

The Journal was registered by the National Council of Ukraine on Television and Radio Broadcasting on 09.05.2024, carrier identifier R30-04569. ISSN 0957-798X (Print), ISSN 3041-2293 (Online). DOI: http://dx.doi.org/10.37434/tpwj

Subscriptions, 12 issues per year:
348 Euro — annual subscription for the printed (hard copy) version, air postage and packaging included;
288 Euro — annual subscription for the electronic version (sending issues in pdf format or providing access to IP addresses).

Representative Offices of “The Paton Welding Journal”:

BRAZIL, Arc Dynamics
Address: Nova Iguacu, Rio de Janeiro, Brazil
Daniel Adolpho, Tel.: +55 21 9 6419 5703, E-mail: dadolpho@arcdynamics.com.br

BULGARIA, Bulgarian Welding Society
Address: Blvd. Asen Yordanov No.10, Sofia 1592, Bulgaria
Pavel Popgeorgiev, Tel.: +359 899 96 22 20, E-mail: office@bws-bg.org

CHINA, China-Ukraine Institute of Welding, Guangdong Academy of Sciences
Address: Room 210, No. 363 Changxing Road, Tianhe, Guangzhou, 510650, China
Zhang Yupeng, Tel.: +86-20-61086791, E-mail: patonjournal@gwi.gd.cn

POLAND, PATON EUROPE Sp. z o. o.
Address: ul. Kapitałowa 4, 35-213, Rzeszów, Poland
Anton Stepakhno, Tel.: +38067 509 95 67, E-mail: Anton.Stepakhno@paton.ua

---

The content of the Journal includes articles received from authors from around the world in the field of welding, cutting, cladding, soldering, brazing, coating, 3D additive technologies, electrometallurgy, material science, NDT and selectively includes translations into English of articles from the following journals, published in Ukrainian:

- «Avtomatychne Zvaryuvannya» (Automatic Welding), https://patonpublishinghouse.com/eng/journals/as;
- «Suchasna Elektrometalurhiya» (Electrometallurgy Today), https://patonpublishinghouse.com/eng/journals/sem;
- «Tekhnichna Diahnostyka ta Neruinivnyi Kontrol» (Technical Diagnostics & Nondestructive Testing), https://patonpublishinghouse.com/eng/journals/tdnk.

© E.O. Paton Electric Welding Institute of NASU, 2025
© International Association “Welding” (Publisher), 2025

CONTENTS

ORIGINAL ARTICLES

INFORMATION

---

*Translated Article(s) from “Avtomatychne Zvaryuvannya” (Automatic Welding), No. 6, 2024.

**Translated Article(s) from “Suchasna Elektrometalurhiya” (Electrometallurgy Today), No. 4, 2024.

Indexing: The electronic edition of the Journal is stored in the V.I. Vernadsky National Library of Ukraine (eVerLib), included in the OPEN UKRAINIAN CITATION INDEX database and international databases: CROSSREF, EBSCO, Google Scholar, INDEX COPERNICUS, IET Inspec, ULRICHSWEB.

DOI: https://doi.org/10.37434/tpwj2025.01.01

DIFFUSION BONDING OF Ti6-4 ALLOY THROUGH MULTILAYER INTERLAYERS OF AN EUTECTIC COMPOSITION BASED ON Ti–Cu SYSTEM

T.V. Melnychenko, A.I. Ustinov, O.Yu. Klepko, O.V. Samofalov

E.O. Paton Electric Welding Institute of the NASU
11 Kazymyr Malevych Str., 03150, Kyiv, Ukraine

ABSTRACT

The regularities of diffusion bonding of the titanium alloy Ti6-4 through multilayer interlayers of eutectic composition based on Ti–Cu system, produced by electron beam deposition under vacuum, were investigated in this work. The microstructure and mechanical properties of the joints were analyzed using scanning electron microscopy and by determining their shear strength. It is shown that multilayer interlayers provide defect-free joints without degradation of titanium alloy properties at a temperature of 920–950 °C, corresponding to the melting range of the interlayer. It is established that the nature of the reaction interaction of the components of the interlayer and Ti6-4 alloy during heating depends on the temperature and melting range of the multilayer interlayer and determines the microstructure and phase composition of the joint. Absence of continuous layers of intermetallics (TiCu, Ti_2Cu) in the joint and formation of a dispersed Widmanstätten structure with copper and nickel content of < 7 at.% provide the joint strength at the level of the Ti6-4 alloy.

KEYWORDS: multilayer foil, EB-PVD, Ti6-4 alloy, diffusion bonding, microstructure, shear strength

INTRODUCTION

Ti6-4 titanium alloy belongs to α+β type that ensures its high values of room temperature impact toughness and high temperature creep strength. Owing to its low specific weight, high corrosion resistance and specific strength, the alloy is widely used in the aerospace, automotive, ship-building industries, nuclear power engineering, medicine, etc. [1, 2]. According to statistics, more than 50 % of titanium applied in the aerospace industry is Ti6-4 alloy, used to produce large-sized welded and prefabricated structures of flying vehicles, high-pressure cylinders operating in the temperature range of 196–450 °C, and other structural elements. However, manufacturing modern products, in particular complex-shaped and thick-walled ones, requires the technology of joining their individual elements, which, on the one hand, will prevent degradation of the structural and mechanical characteristics of the alloy, and, on the other hand, is reliable and low-cost. Ti6-4 alloy joining is performed by different methods: arc, electron beam, laser, diffusion welding and brazing [3, 4]. Welding of Ti6-4 titanium alloy by the traditional methods is conducted at a high temperature and it is accompanied by structural transformations in the material, grain growth, formation of brittle intermetallics, metastable phases, defects and pores that leads to lowering of the alloy strength values and formation of residual stresses in the joint [5, 6]. The most acceptable method for formation of the alloy joint is vacuum brazing, as the process runs in vacuum that prevents the alloy oxidation and does not require application of flux with further cleaning of the joint surface from contamination and corrosion products. Absence of considerable compressive forces allows joining thin-walled and complex-shaped parts. Considering the high temperature of α↔β transformation in Ti6-4 alloy (970–1010 °C [7]), brazing is performed with application of braze alloys, the most common of which are those based on Ti–Cu–Ni an Ti–Zr–Cu–Ni systems, at the temperature of 980–1040 °C close to the temperature of phase transformation. These braze alloys are the most acceptable to produce joints used at the temperature of ~ 600 °C in an aggressive medium, and they have the shear strength of ~ 50–70 % of that of the base material [8]. Application of braze alloys at certain technological parameters, ensures high values of joint strength [9], and additional heat treatment is performed to form a duplex structure and to recover the mechanical properties of the titanium alloy [10]. However, it is desirable to conduct brazing of thin-walled structural elements and those made from strain-hardened alloys at a lower temperature, because of the possible degradation of the titanium alloy structure. Lowering of the brazing temperature is also required during the fabrication of structures, consisting of elements of different chemical composition. Therefore, development of new methods of joining Ti6-4 alloy that will ensure a lowering of the level of thermal impact on the alloy is urgent. It is known that application of intermediate multilayers, in which at heating the diffusion processes of the component mixing proceed at an anomalously high rate, allows lowering the temperature of the joint formation process [11]. From this viewpoint, it is rational to perform joining of Ti6-4 alloy with application of multilayers based on systems with an eutectic with melting temperature < 980 °C, which will prevent degradation of the alloy structural characteristics. The advantage of such an approach is fast formation of a thin interlayer of the liquid phase in the butt, due to intensive diffusion mixing of the components of the multilayer that will ensure wetting of the joint surfaces and their physical contact at a low compressive force. The work is a study of the regularities of formation of the structure and mechanical properties of Ti6-4 alloy joints, produced by diffusion bonding through intermediate multilayers based on systems with Ti–Cu and Ti–Cu–Ni eutectic in the temperature range of 920–950 °C.

MATERIALS AND METHODS

Interlayers in the form of multilayer foil (MF) of a chemical composition close to that of binary eutectics I and II of Ti–Cu system (Figure 1, *a*) and ternary eutectic III of Ti–Cu–Ni system (Figure 1, *b*) were produced by the method of layer-by-layer electron beam deposition of components into a rotating substrate, described in detail in [14]. Scheme of producing the MF is shown in Figure 1, *c*.

The thickness ratio of binary MF component layers is determined by the ratio of their vapour flow intensities. The layer alternation period (sum of the two component layer thicknesses) at a certain evaporation intensity is determined by the substrate evaporation rate. Pressure in the chamber during deposition is maintained at the level of 10^{-3} Pa. Substrate temperature was kept below 300 °C that prevented diffusion mixing of the component layers. At substrate rotation speed of 2 min^{-1} an MF with layer alternation period of 500 nm and 35 μm thickness was produced. The required chemical composition of ternary Ti–Cu–Ni MF was ensured by cladding the Ti–Cu interlayer with layers of nickel of a certain thickness by evaporation of an additional nickel ingot. Figure 2, *a* shows the microstructure of a binary Ti–Cu MF, and Figure 2, *b* is the general view of a ternary Ti–Cu–Ni foil. Table 1 gives the chemical composition of binary and ternary MF. Foil melting temperature was determined by the method of differential thermal analysis (DTA) in VDTA-2000 unit. Figure 2, *c* shows fragments of DTA curves in the melting range of foils of different composition, and Table 1 gives their melting ranges.

Bonding of Ti6-4 alloy was conducted by heating an assembly, which consisted of samples of the alloy and MF placed between them, in a vacuum chamber in a fixture which allowed fixing the position of the samples and the foil (Figure 3, *a*). Sample dimensions are shown in Figure 3, *b*.

Grinding of the sample surfaces on R1200 abrasive paper and ultrasonic cleaning of the samples and

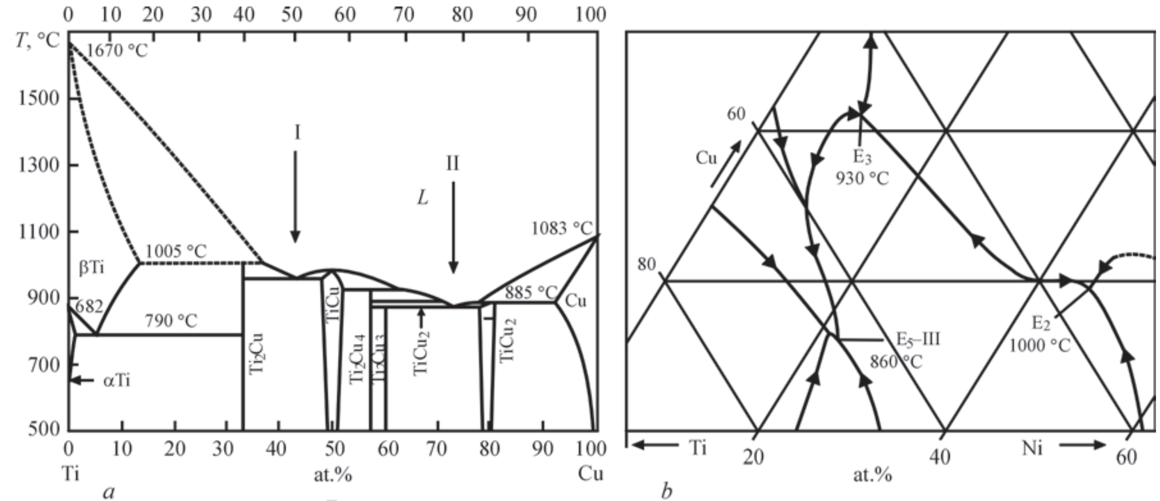

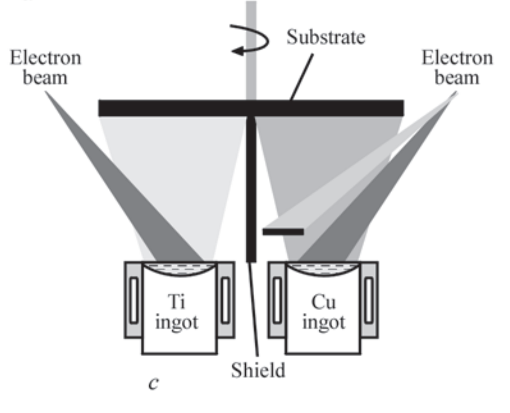

Figure 1. Constitutional diagram of Ti–Cu [12] (*a*), Ti–Cu–Ni [13] (*b*) and scheme of producing MF (*c*)

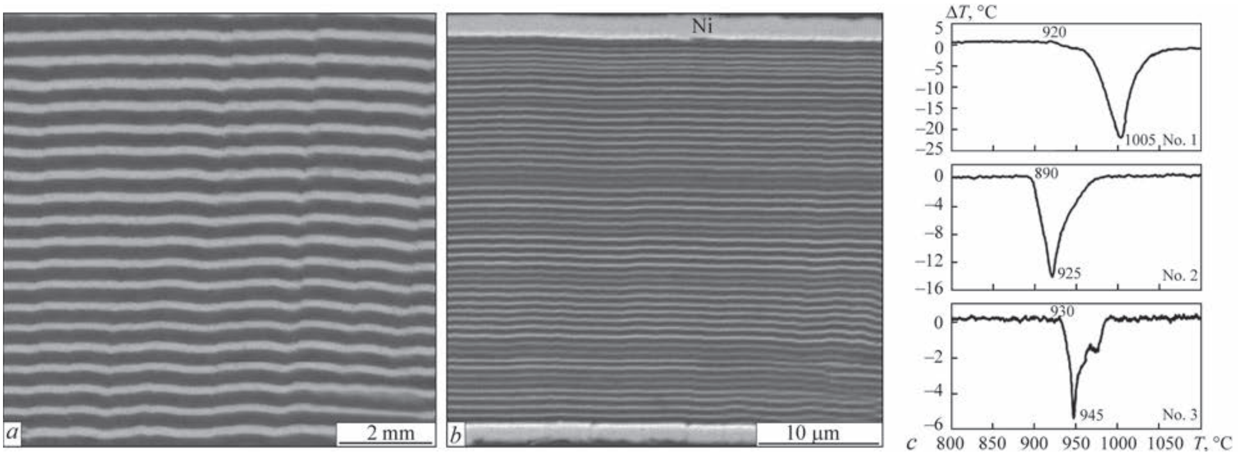

Figure 2. SEM image of the cross-section of Ti–Cu MF No. 1 with 500 nm layer period (*a*), Ti–Cu–Ni MF No. 3 (*b*), fragments of MF DTA curves (*c*)

Table 1. MF characteristics

MF number	MF structure	MF overall chemical composition, at.%			Melting range, °C
		Ti	Cu	Ni	
1	Ti/Cu	55.7	44.3	–	920–1005
2	Ti/Cu	22.6	77.4	–	890–925
3	Ni+Ti/Cu+Ni	67.1	18.1	14.8	930–945

the foil in acetone were performed before the bonding process. The bonding process was conducted at temperatures of 920 and 950 °C for 60 min, and 980 °C for 30 min at the compressive force of 70 kPa. The process temperature was selected according to MF melting temperature. The vacuum in the chamber was maintained at the level of 10^{-3} Pa.

The microstructure and chemical composition of different regions of the joint were studied with application of scanning electron microscope CamScan-4, fitted with energy-dispersive analysis system EDX INCA 200. Samples for metallographic investigations were prepared by a standard procedure in grinding-polishing equipment of Struers Company. Shear testing of the samples using special fixtures was conducted to assess the quality of the joints (Figure 3, *c*). Tensile strength of samples of a standard shape to GOST was determined in ZDM 4 tensile testing machine. Average strength value was found by the results of testing not less than three samples.

EXPERIMENTAL RESULTS AND THEIR DISCUSSION

Table 2 gives the characteristics of the joints produced with MF application in different modes.

Figures 4–6 show the joint microstructure. Chemical and phase composition of the respective regions of the diffusion zone are given in Tables 3–5. At bonding through MF No. 1 and No. 2 regions of different chemical and phase composition form in the diffusion zone (Figures 4, 5) that is the consequence of diffusion mixing of the components of MF and titanium alloy due to the alloy surface wetting by the liquid phase which forms at MF melting.

In the diffusion zone central part a layer based on Ti_2Cu and TiCu intermetallics forms as a result of re-

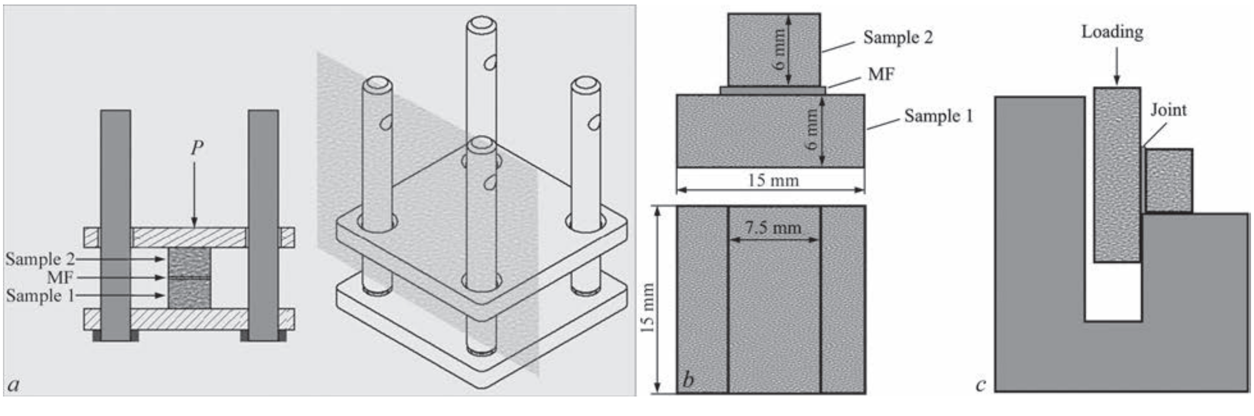

Figure 3. Schematic image of the fixture for conducting the bonding process (*a*), samples (*b*) and fixture for shear testing (*c*)

Table 2. Properties of joints produced in different modes

MF number	Temperature, °C	Duration, min	Diffusion zone width, μm	Shear strength τ, MPa
1	920	60	120	180
	950	60	150	190
2	920	60	123	160
	950	60	190	409
3	920	60	190	453
	950	60	250	532

action interaction of MF components at heating and counter diffusion of copper and titanium on MF/alloy interface. The thickness and phase composition of the intermetallic layer were determined by MF chemical composition and heating temperature. At temperature rise the intermetallic layer thickness decreases and its fragmentation takes place. Its simultaneous enrichment in titanium leads to formation of Ti_2Cu intermetallic. Note that the intensity of diffusion mixing of titanium and copper at application of MF No. 2 is two times higher. This is attributable to increase of the

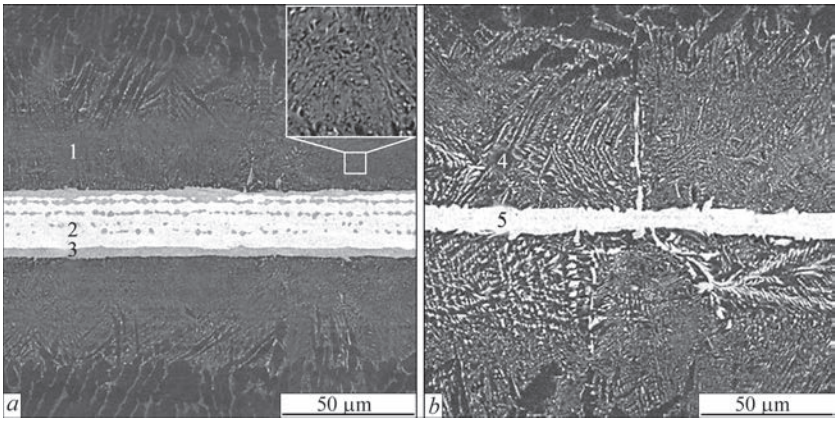

Figure 4. Microstructure of the joints produced using intermediate MF No. 1 in the following modes: 920 °C, 60 min (*a*) and 950 °C, 60 min (*b*)

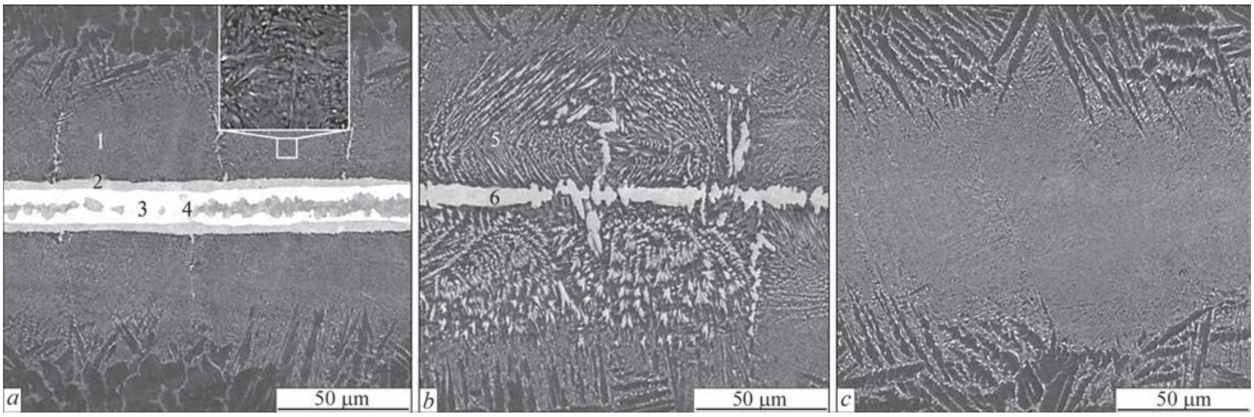

Figure 5. Microstructure of joints produced with application of intermediate MF No. 2 in the following modes: 920 °C, 60 min (*a*), 950 °C, 60 min (*b*), 980 °C, 30 min (***c***)

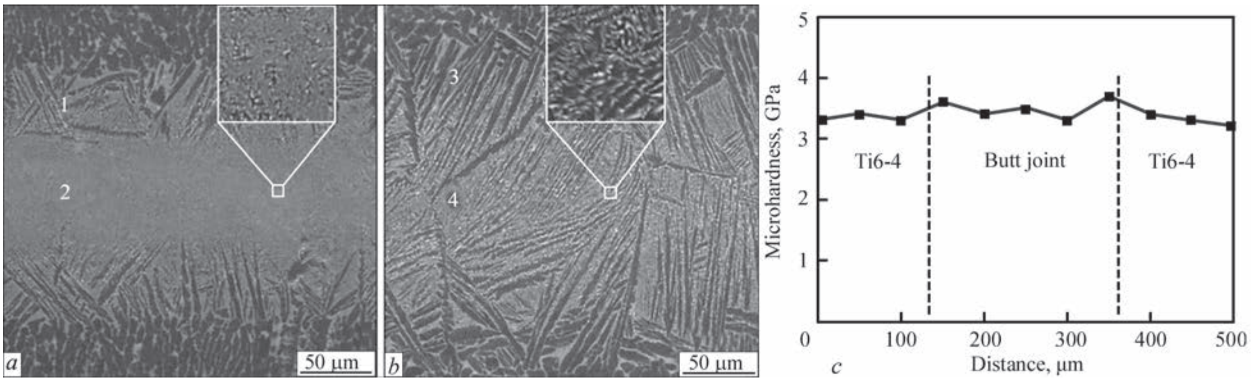

Figure 6. Microstructure of joints produced with application of intermediate MF No. 3 in the following modes: 920 °C, 60 min (*a*) and 950 °C, 60 min (*b*) and microhardness distribution in the butt joint (*c*)

Table 3. Chemical and phase composition of regions of the joints in Figure 4

Region	Chemical composition, at.%				Phase composition	*HV*20, GPa
	Al	Ti	V	Cu		
1	7.81	80.6	3.1	8.49	α-Ti+Ti_2Cu	3.7
2	–	53.96	–	46.04	TiCu+Ti_2Cu	3.4
3	1.95	66.4	–	31.65	Ti_2Cu	–
4	7.31	80.11	2.54	10.04	α-Ti+Ti_2Cu	3.8
5	2.37	67.69	–	29.94	Ti_2Cu	3.0

Table 4. Chemical and phase composition of joint regions in Figure 5

Region	Chemical composition, at.%				Phase composition	*HV*20, GPa
	Al	Ti	V	Cu		
1	8.95	77.29	4.21	9.55	α-Ti+Ti_2Cu	3.7
2	2.43	65.66	–	31.91	Ti_2Cu	–
3	–	50.43	–	49.57	TiCu	3.2
4	7.6	59.09	–	33.31	Ti_2Cu	3.0
5	8.64	77.53	3.57	10.27	α-Ti+Ti_2Cu	3.9
6	2.7	66.81	–	30.49	Ti_2Cu	3.2

Table 5. Chemical and phase composition of regions of the joints in Figure 6

Region	Chemical composition, at.%					Phase composition
	Al	Ti	V	Ni	Cu	
1	7.86	82.03	3.51	3.35	3.25	α-Ti+Ti_2Cu+Ti_2Ni
2	5.99	81.52	2.52	4.03	5.94	
3	9.44	83.87	3.64	1.47	1.59	
4	8.07	82.46	2.5	2.61	4.35	

volume fraction of the liquid phase in the butt joint at heating temperature of 920–950 °C that is ensured by smaller melting range of MF No. 2 (Table 1).

Intermetallic layer formation in the butt joint can be explained as follows. At Ti–Cu MF heating up to the melting temperature appearance of the liquid phase in the butt joint promotes titanium diffusion from the alloy into the interlayer, leading to formation of excess TiCu and Ti_2Cu intermetallics with melting temperature higher than that of the bonding process. We can assume that this leads to reduction of the liquid phase volume fraction in the butt and limits diffusion mixing of the components. This assumption is supported by absence of an intermetallic layer in the joint produced at the temperature of 980 °C (Figure 5, *c*) that is higher than the melting temperature of TiCu and Ti_2Cu intermetallics. Copper diffusion into the titanium alloy leads to lowering of α↔β transformation temperature. It results in βTi decomposition in the diffusion zone during cooling by an eutectoid reaction of $\beta Ti \rightarrow \alpha Ti + Ti_2Cu$ with formation of an eutectoid of hyper eutectoid composition with a dispersed structure (region 1 and its enlarged view in Figures 4, *a* and 5, *a*), the phase components of which become larger at temperature rise (regions 4 in Figures 4, *b* and 5, *b*). A region with Widmanstatten structure forms between the region of eutectic structure and Ti6-4, as a result of βTi transformation into acicular αTi.

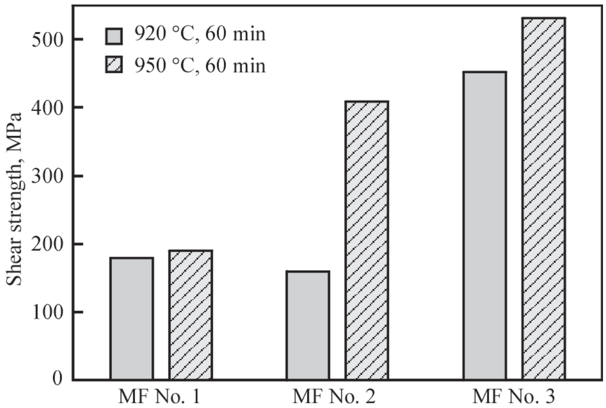

Figure 7. Shear strength of the joints

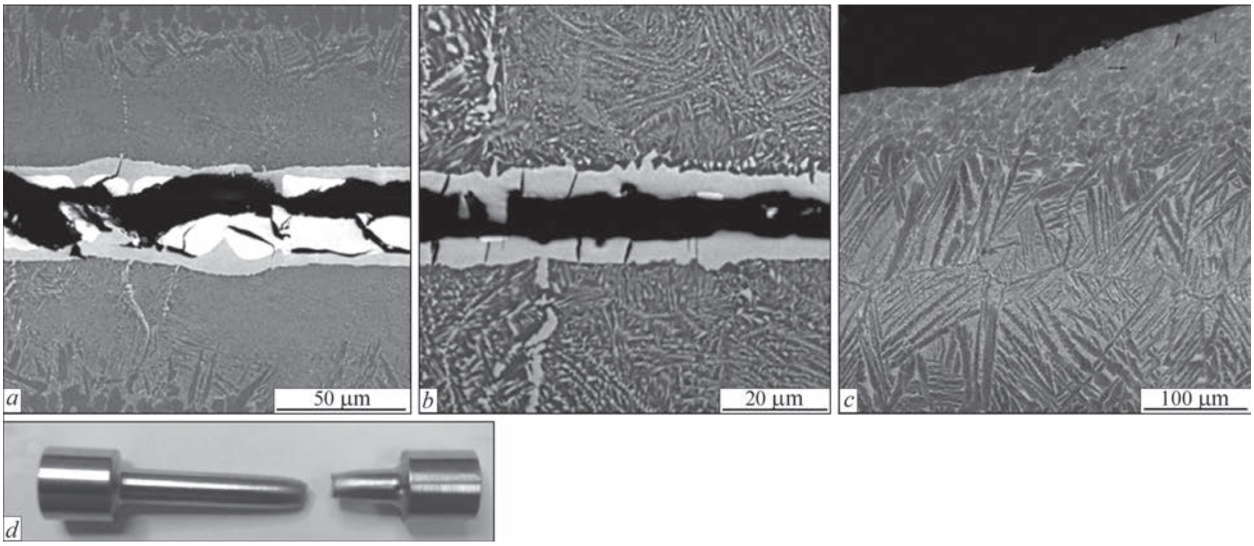

Figure 8. Joint microstructure after shear testing: MF No. 1, $T = 920$ °C (*a*), MF No. 1, $T = 950$ °C (*b*), MF No. 3, $T = 950$ °C (*c*) and sample image (MF, No. 3, $T = 950$ °C) after tensile testing (*d*)

No formation of an intermetallic layer in the butt joint is observed at Ti6-4 alloy bonding through MF No. 3 at the temperature of 920 and 950 °C (Figure 6).

It can be assumed that a significant volume of the liquid phase of a homogeneous composition forms at foil melting that is indicative of a narrow melting range of the foil (Table 1). This ensures intensive diffusion mixing between the foil and alloy components and formation of a continuous βTi interlayer in the butt joint as a result of a lowering of α→β transformation temperature. Two structural regions form in the joint at cooling. In the joint central part (regions 2, 4 in Figure 6, *a*, *b*) an eutectoid with a dispersed structure forms by eutectoid reaction of $\beta Ti \rightarrow \alpha Ti + Ti_2(Cu) + Ti_2(Ni)$. A region with Widmanstatten structure is present between the eutectoid region and the alloy metal. At increase of process temperature, a coarsening of structural components of the regions takes place (Figure 6, *b*). On the other hand, temperature rise ensures an increase of the intensity of diffusion mixing of MF and alloy components and of the diffusion zone width and formation of the Widmanstatten structure over its entire width that promotes the homogeneity of the chemical composition and microhardness of the butt joint (Figure 6, *b*, *c*).

Shear testing of the joints was conducted to assess their mechanical properties. Figure 7 shows a comparative diagram of shear strength of the joints produced at application of different MF.

One can see that formation of a continuous intermetallic layer in the butt joint results in the low strength of the joint. The latter fails in the area of the intermetallic layer (Figure 8, *a*, *b*), which has the microhardness lower than that of the adjacent regions (Tables 3, 4). One can assume that formation of Ti_2Cu and TiCu intermetallics as a result of reaction diffusion of titanium and copper at heating is accompanied by formation of vacancy type defects and pores, owing to volume effect at phase transformations. Note that formation of a fragmented intermetallic interlayer in the butt joint (Figure 5, *b*) promotes an increase of the joint shear strength. Absence of an intermetallic interlayer in the butt joint and formation of a homogeneous structure of the diffusion zone ensures an increase of the joint mechanical properties. So, the highest shear strength (532 MPa) and tensile strength (930 MPa) is demonstrated by the joint produced using MF No. 3 at the temperature of 950 °C, in which the content of intermetallic-forming components (Ni+Cu) in the butt joint is < 7 at.%. The joint strength corresponds to the strength level of Ti6-4 alloy ($\sigma = 935$ MPa in tensile testing) that is ensured by homogeneity of mechanical properties of the joint regions (Figure 6, *c*).

At shear and tensile testing the joint fails in the region of Ti6-4 alloy (Figure 8, *c*, *d*). Our result is in agreement with experimental data of the authors of [15] obtained at brazing Ti6-4 alloy using traditional Ti–Zr–Ni–Cu braze alloys at the temperature of 950–990 °C. The advantage of the diffusion bonding method with application of an intermediate MF layer of eutectic composition is the possibility of lowering the temperature required to produce an equal-strength and defect-free joint of the titanium alloy.

CONCLUSIONS

1. Application of intermediate multilayers of eutectic composition based on Ti–Cu and Ti–Cu–Ni systems ensures production of a permanent and defect-free joint of Ti6-4 alloy by the method of diffusion bonding at the temperature of 920–950 °C.

2. Joint microstructure depends on MF temperature and melting range, and it is determined by reac-

tion interaction of the foil and titanium alloy components at heating. Formation of a layer of Ti_2Cu and TiCu intermetallics in the butt joint leads to lowering of the joint mechanical properties.

3. Producing a joint with shear and tensile strength matching that of Ti6-4 alloy, is ensured by formation in the butt of a dispersed Widmanstatten structure with copper and nickel content < 7 at.% and homogeneous microhardness distribution.

REFERENSES

1. Leyens, C., Peters, M. (2003) *Titanium and titanium alloys: Fundamentals and applications*. WILEY-VCH, Weinheim.
2. Lutjering, G., Williams, J.C. (2007) *Titanium*. 2 Ed. Springer-Verlag, Berlin.
3. Balasubramanian, T., Balasubramanian, V., Muthumanikkam, M. (2011) Fatigue performance of gas tungsten arc, electron beam, and laser beam welded Ti–6Al–4V alloy joints. *J. Mater. Eng. and Performance*, **20**, 1620–1630. DOI: https://doi.org/10.1007/s11665-010-9822-y
4. Ahmed, Y.M., Salleh, K., Sahari, M., Ishak, M. (2012) Welding of titanium (Ti–6Al–4V) alloys: A review. In: *Proc. of the National Graduate Conf., Kajang, Malaysia*, 8–10.
5. Zamkov, V.N., Prilutsky, V.P., Petrichenko, I.K. et al. (2001) Effect of the method of fusion welding on properties of welded joints in alloy Ti–6AI–4V. *The Paton Welding J.*, **4**, 2–6.
6. Murthy, K.K., Potluri, N.B., Sundaresan, S. (1997) Fusion zone microstructure and fatigue crack growth behaviour in Ti–6Al–4V alloy weldments. *Mater. Sci. and Technol.*, 13(**6**), 503–510. DOI: https://doi.org/10.1179/mst.1997.13.6.503
7. Borisova, E.A. (1980) *Titanium alloys. Metallography of titanium alloys*. Metallurgiya, Moscow [in Russian].
8. Shapiro, A., Rabinkin, A. (2003) State of the art of titanium-based brazing filler metals. *Welding J.*, 82(**10**), 36–43.
9. Elrefaey, A., Tillmann, W. (2009) Effect of brazing parameters on microstructure and mechanical properties of titanium joints. *J. of Materials Proc. Technology*, **209**, 4842–4849. DOI: https://doi.org/10.1016/j.jmatprotec.2009.01.006
10. Shapiro, A.E. (2016) Brazing of conventional titanium alloys. *ASM Metal Handbook*, **6**, 1–25.
11. Ustinov, A.I., Falchenko, Yu.V., Ishchenko, A.Ya et al. (2008) Diffusion welding of γ-TiAl based alloys through nano-layered foil of Ti/Al system. *Intermetallics*, **16**, 1043–1045. DOI: https://doi.org/10.1016/j.intermet.2008.05.002
12. Murray, J.L. (1983) The Cu–Ti (copper-titanium) system. *Bulletin of Alloy Phase Diagrams*, 4(**1**), 81–95.
13. Cacciamani, G., Schuster, J.C., Effenberg, G., Ilyenko, S. (2006) Cu–Ni–Ti (copper–nickel–titanium). *Light Metal Ternary Systems: Phase Diagrams, Crystallographic and Thermodynamic Data*, **11**, 266–283.
14. Ustinov, A.I., Melnychenko, T.V., Demchenkov, S.A. (2021) Structural mechanism of plastic deformation of Al/α-Si multilayer foils at heating under load. *Materials Sci. and Eng.*: A, **810**, 141030. DOI: https://doi.org/10.1016/j.msea.2021.141030
15. Ganjeh, E., Sarkhosh, H., Bajgholi, M.E. et al. (2012) Increasing Ti–6Al–4V brazed joint strength equal to the base metal by Ti and Zr amorphous filler alloys. *Mater. Charact.*, **71**, 31–40. DOI: https://doi.org/10.1016/j.matchar.2012.05.016

ORCID

T.V. Melnychenko: 0000-0002-1460-5532,
A.I. Ustinov: 0000-0002-8855-3499,
O.Yu. Klepko: 0000-0003-2014-1938

CONFLICT OF INTEREST

The Authors declare no conflict of interest

CORRESPONDING AUTHOR

T.V. Melnychenko
E.O. Paton Electric Welding Institute of the NASU
11 Kazymyr Malevych Str., 03150, Kyiv, Ukraine.
E-mail: melnychenko21@ukr.net

SUGGESTED CITATION

T.V. Melnychenko, A.I. Ustinov, O.Yu. Klepko, O.V. Samofalov (2025) Diffusion bonding of Ti6-4 alloy through multilayer interlayers of an eutectic composition based on Ti–Cu system. *The Paton Welding J.*, **1**, 3–9.
DOI: https://doi.org/10.37434/tpwj2025.01.01

JOURNAL HOME PAGE

https://patonpublishinghouse.com/eng/journals/tpwj

Received: 31.07.2024
Received in revised form: 23.10.2024
Accepted: 23.01.2025

DOI: https://doi.org/10.37434/tpwj2025.01.02

COMPENSATION OF SPATIAL DEFORMATION IN PRODUCTS AT ADDITIVE ELECTRON BEAM SURFACING

V.A. Matviichuk

E.O. Paton Electric Welding Institute of the NASU
11 Kazymyr Malevych Str., 03150, Kyiv, Ukraine

ABSTRACT

The aim of the work is to analyze and optimize the shaping of GTE blade in the process of fabrication using additive electron beam technology. Using the method of computer simulation in the Simufact Additive software, the influence of technological printing parameters on product shaping was investigated, and shrinkage phenomena that occur during the printing process were analyzed. The printing simulation was performed and the results were compared to the reference model. The optimized computer models of GTE blades were created. According to the calculation results, when optimized models are used, the deviation in the geometric dimensions of printed blades does not exceed the product size tolerances of ±0.3 mm.

KEYWORDS: additive technologies, electron beam, surfacing, simulation, shaping, 3D printer

INTRODUCTION

When metal products are created by the additive manufacturing method, local shrinkage phenomena occur at the process of layer-by-layer heating and cooling, resulting in overall residual deformations — distortion of linear dimensions of the printed part [1–3]. In order to compensate for residual deformations, it becomes necessary to correct the product model by taking the expected deformations into account.

A number of factors influence the shape of products at the printing process:

- material from which a part is made;
- technological parameters of printing;
- spatial position of a product relative to the platform;
- location of a part in the product assembly;
- shape of technological supports;
- overall temperature of the product assembly and the environment.

Given that products usually have a complex geometric shape, it becomes problematic to fabricate the end product with the required dimensions within tolerances. To solve this problem, it is planned to apply computer simulation methods of the printing process with the subsequent correction of the model, based on which a product will be printed [2].

THE AIM

of this work is to analyze and optimize the GTE blade shaping in the process of fabrication using additive electron beam technology.

The software product Simufact Additive, developed by MSC Software, was used in the work. This is a specialized software package designed to simulate 3D printing of metal parts using Powder Bed Fusion technology, including Selective Laser Melting (SLM), Direct Metal Laser Sintering (DMLS), Selective Laser CUSING of metal powder materials, Electron Beam Melting (EBM) and a number of other processes [4].

Simufact Additive provides an opportunity to:

- calculate deformations of a part and reduce or avoid distortion of its shape;
- compare simulation results with the reference shape;
- select the optimal printing direction;
- optimize the supporting structures (supports);
- obtain the state of a part after heat treatment, removal of the base plate and supporting structure;
- minimize residual stresses.

The MARC solver [5] is the basis of the Simufact Additive software. MARC has advanced capabilities for conducting a coupled temperature and thermomechanical analysis of the stress-strain state of a product at layer-by-layer printing, taking into account thermal deformations and material properties depending on temperature.

A special voxel mesh generator is used for calculations. Voxels are elementary cells that make up the studied product model. A regular mesh is created, that is used to simulate layer-by-layer printing of a part. The MARC solver has added the ability to sequentially activate voxel layers. New methods for simulation of the cutting process have also been added, which are necessary to simulate the process of removing the base plate and supporting structure.

Simufact Additive uses two approaches for prompt calculation of product deformations during printing [4]: on the base of the approximate method of shrinkage (Mechanical inherent strain approach) within the mechanical problem of elasticity theory or as a result

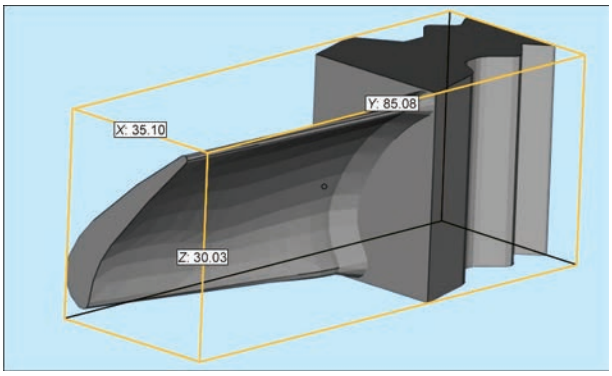

Figure 1. GTE stator blade model

of a more general coupled analysis of the thermoplastic deformation of a product material during printing, assuming the same simplified thermal printing cycle for each voxel.

The first approach is based on the determination of the shrinkage function (residual plastic deformations) from printing a single elementary volume (voxel) depending on the technological parameters of a layer-by-layer product formation by means of experimental calibration of the mentioned deformations on a standard printed sample of a beam type of a limited size. The heating kinetics of a product during printing is not calculated; residual deformations and stresses are determined as a result of solving the mechanical loading problem of the finite element model of a product by additional shrinkage deformations for each printed voxel, which allows significantly reducing the calculation time while maintaining sufficient accuracy from an engineering point of view.

The second calculation approach is more general and is based on a coupled thermal and thermomechanical analysis at layer-by-layer printing of a product. However, to reduce the calculation time, the assumption of an identical (simplified) thermal cycle for each voxel of the printed material is used, which gives an opportunity not to analyze the nonstationary thermal conductivity problem for the entire model during the printing process. As a result of the calculation using this approach, the approximate kinetics of heating, as well as stresses and deformations of a product are determined.

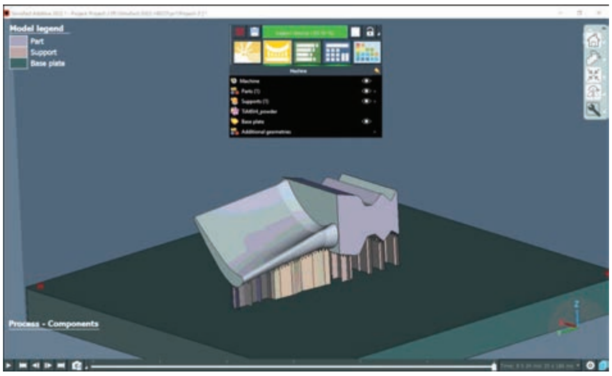

Figure 3. Interface of the Simufact Additive software with the integrated GTE blade model

In order to compensate for residual deformations of a product, it is possible to export a model of the deformed geometry with any scale factor. Therefore, it is possible to select the initial shape of a part, which, after the printing process, gives a minimum deviation from the required shape, compensating for deformations that occur during creation of this part [3].

Using the Simufact Additive software product, it is possible to determine the influence of printing technological parameters on the end product parameters and predict deformations of the part shape. In this work, a model of a gas turbine engine (GTE) blade was used (Figure 1).

Using the Materialise Magics software product, technological supports for further printing of a product were generated. Several spatial positions of the parts shown in Figure 2 were used.

The models in Figure 2, *a*, *b* provide the shortest time for building a product in the printing process. The model of Figure 2, *c* provides an opportunity to place on the printer platform and print the largest quantity of parts in one production cycle.

The files of product models and technological supports were exported in STL format to the Simufact Additive software.

The further actions are aimed at optimizing the geometric shape of a part and obtaining information on the impact of technological parameters on the shaping of products and their properties.

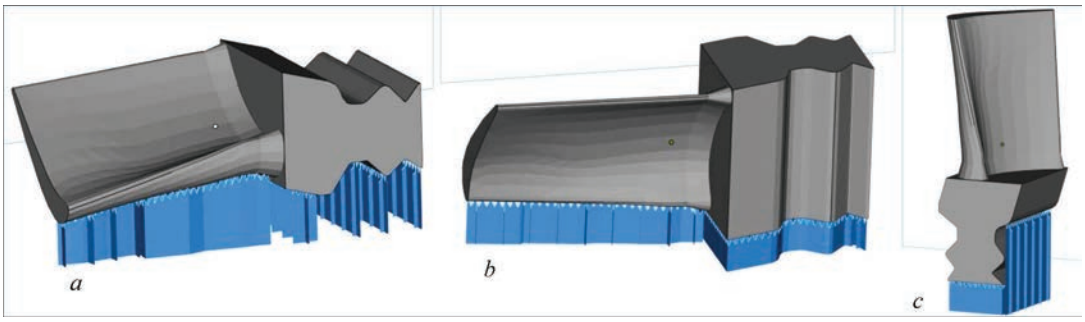

Figure 2. Product models with technological supports

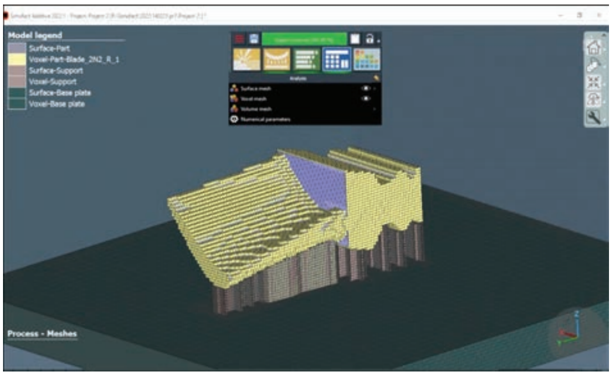

Figure 4. Creation of elementary cells — voxels

In the Simufact Additive interface, a project is created, settings are set, where the parameters of equipment and technological process, part and platform materials are specified, and product models are imported along with technological supports (Figure 3).

The technological parameters like power, speed and diameter of electron beam, powder layer thickness, scanning method, thermal characteristics of printing are set in the interface settings in the Build-Properties tab.

Further, voxels (elementary cells that make up the model of a studied product) were generated by the software (Figure 4).

The next step was simulating the layer-by-layer printing of a product. The graphical interface of Simufact Additive, which displays the printing process, is shown in Figure 5.

Shrinkage strains were determined using a different, more general approach to the analysis of thermoplastic deformation of the material. Therefore, the procedure for calibrating shrinkage strains for material voxels was not carried out, but the analysis of the kinetics of the temperature problem of product heating at layer-by-layer shaping and the coupled thermoplastic analysis of the stress-strain state were performed.

The colour corresponds to the temperature value of a product, technological supports and platform at each stage of the printing simulation. The colour palette with temperature values is shown in Figure 5 in the Temperature table.

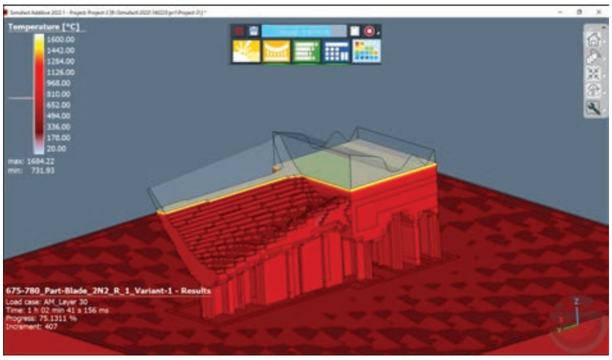

675-780_Part-Blade_2N2_R_1_Variant-1 - Results
Load case: AM_Layer 30
Time: 1 h 02 min 41 s 156 ms
Progress: 75.1311 %
Increment: 407

Figure 5. Graphic representation of printing GTE blade in the Simufact Additive software

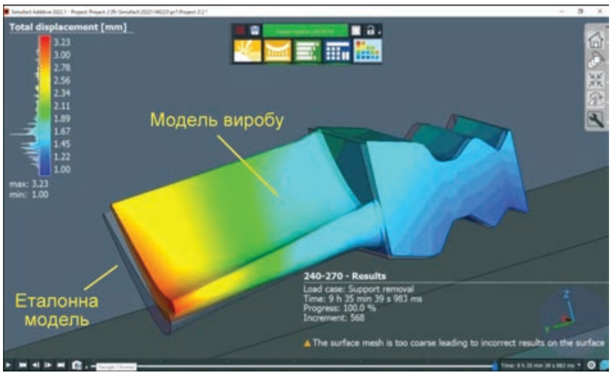

240-270 - Results
Load case: Support removal
Time: 9 h 35 min 39 s 983 ms
Progress: 100.0 %
Increment: 568

The surface mesh is too coarse leading to incorrect results on the surface

Figure 6. Deviation of the printed product model dimensions from the reference model

Based on the simulation results, a file was obtained (Figure 6), where deviations of the GTE blade dimensions from the reference model were calculated. Deviations in dimensions arise due to the product shape deformation at the printing process. The values of possible deformations correspond to the colour and are shown on the palette in the Total displacement table.

The next stage of research is correction of the model, calculation of spatial deformations of the corrected model and its comparison with the reference model.

The GTE blade model is corrected to compensate for spatial deformations in the Shape comparison menu of the Simufact Additive software. The model obtained as a result of the additive process simulation is compared with the reference model. In the programme interface, the deviation in the dimensions of the corrected model from the reference one is displayed by the colour palette (Figure 7).

The obtained model is then processed by the software. A new file is created taking into account the shape optimization. The printing simulation process is consistently repeated. The next GTE blade model is created, which is compared with the reference model.

If the obtained model does not match the reference model within the tolerances, the process is repeated.

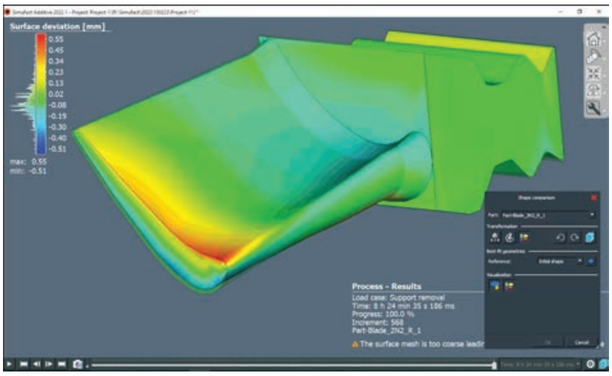

Process - Results
Load case: Support removal
Time: 8 h 24 min 35 s 186 ms
Progress: 100.0 %
Increment: 568
Part-Blade_2N2_R_1

The surface mesh is too coarse leadi

Figure 7. Shape comparison menu of the Simufact Additive software

The dimensional deviation of printed products from the reference model should not exceed ±0.3 mm.

The corrected model file is exported in stl format and accepted for printing.

Comparing the reference (base) and optimized models of the GTE blade, it can be noted that linear dimensions of the end product model have been increased from (35.1; 85.08 and 30.03) mm in the *X*, *Y*, *Z* coordinates to (35.69; 85.378 and 30.411) mm. I.e., the model has been enlarged with taking into account the compensation of shrinkage phenomena and other factors that lead to deforming the product shape at the printing process.

INFLUENCE OF TECHNOLOGICAL PARAMETERS ON THE SHAPE OF PRODUCTS

The technological parameters of printing products from titanium alloy Ti–6A1–4V ELI powders, which are defined in [6] and given in Table 1, were used in the study.

To simulate printing of the products shown in Figure 2, *a*, three projects with different technological parameters were created in the Simufact Additive software. In each project, spatial deformations and deviations of the GTE blade dimensions during printing were determined, which differ depending on technological parameters of printing (Table 2).

The spatial deformations for each of the technological modes are individual. Therefore, it is necessary to study printing of each of the products shown in Figure 2, for all the modes indicated in Table 1. Then, the shape of products should be corrected and the end models of the GTE blade should be obtained. The created models will be suitable for further printing.

OPTIMIZATION OF DIGITAL MODELS OF THE GTE BLADE

Using the software product Simufact Additive, optimized computer models of the GTE blade were obtained in accordance with the applied technological modes of printing and spatial position of the parts. The simulation results are shown in Table 3.

The optimized models of product assembly with technological supports are exported in stl format and are suitable for further printing.

Table 1. Technological parameters for printing products

Product number	Beam power, W	Travel speed, mm/s	Trajectory shift, mm	Layer thickness, mm	Power density, J/mm^3
1	240	270	0.2	0.1	44.4
2	495	540	0.2	0.1	45.8
3	675	780	0.2	0.1	43.3

Table 2. Spatial deformation values

Product number	Beam power, W	Travel speed, mm/s	Dimensional deviation, mm	
			from	to
1	240	270	1.00	3.23
2	495	540	0.97	2.85
3	675	780	0.98	2.70

Table 3. Results of GTE blade models optimization

Product number	Spatial position in accordance with Figure 2	Beam power, W	Travel speed, mm/s	Dimensional deviation, mm	
				from	to
1	*a*	240	270	–0.03	0.13
2	*a*	495	540	–0.02	0.08
3	*a*	675	780	–0.03	0.09
4	*b*	240	270	–0.05	0.11
5	*c*	240	270	–0.26	0.14
6	*c*	495	540	–0.25	0.14
7	*c*	675	780	–0.25	0.13

Table 4. Dimensions of the digital model and the product “GTE blade”

Parameter	Digital model, mm	Printed product, mm	Dispersion, mm	Tolerance, mm	Compliance mark
Height	35.1	35.21	0.11	±0.3	Matches
Width	30.03	30.16	0.13	±0.3	
Length	85.08	85.06	–0.02	±0.3	

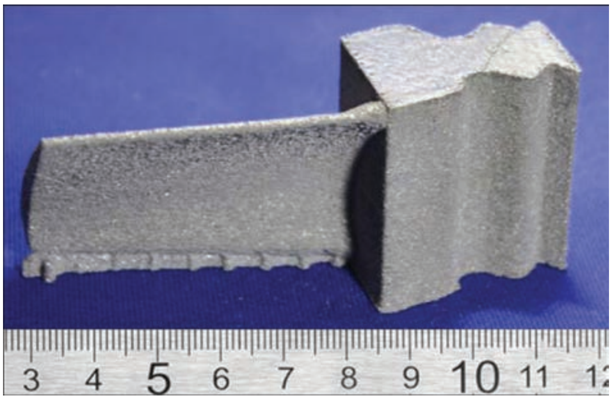

Figure 8. GTE blade

FABRICATION AND STUDY OF THE GTE BLADE GEOMETRY

Based on the optimized computer model (Figure 2, *b*), in accordance with the specified technological parameters (Table 1, product No. 2), GTE blades were fabricated by the method of additive electron beam surfacing (Figure 8).

An analysis of the product shaping was carried out. The geometrical dimensions of the reference computer model and the printed product "GTE blade" are given in Table 4.

It was determined that dimensions of the printed GTE blade match the digital model. According to the calculation results, when using the optimized models, the deviation of the geometric dimensions of printed blades does not exceed the product size tolerances of ±0.3 mm.

CONCLUSIONS

In terms of the technological preparation for the additive manufacturing of experimental samples of GTE working blades, a computer simulation of printing was carried out using the Simufact Additive software product and the obtained results were compared with the reference model. The optimized computer models of the GTE blade were obtained taking into account the spatial deformations that occur during the printing process. According to the calculation results, using the optimized models, the deviation of the geometric dimensions of printed blades does not exceed the tolerances for the product size of ±0.3 mm.

REFERENCES

1. Makhnenko, O.V., Milenin, A.S., Velikoivanenko, E.A. et al. (2017) Modelling of temperature fields and stress-strain state of small 3D sample in its layer-by-layer forming. *The Paton Welding J*., **3**, 7–14. DOI: https://doi.org/10.15407/tpwj2017.03.02
2. Sahini, D.K., Ghose, J., Jha, S.K., Behera, A., Mandal, A. (2020) Optimization and simulation of additive manufacturing processes: challenges and opportunities – A review. In: *Additive Manufacturing Applications for Metals and Composites*, 187–209. DOI: https://doi.org/10.4018/978-1-7998-4054-1.ch010
3. Derrer, J.P. et al. (2022) *Simufact engineering provides the green team & renishaw with a complete AM process simulation solution. SIMUFACT Case study*. https://enteknograte.com/wp-content/uploads/2022/06/hexagon_mi_simufact_casestudy_renishaw_a4_en_screen.pdf
4. *Simufact additive*. https://hexagon.com/products/simufact-additive
5. *MSC. Marc volume A: Theory and user information*. https://simcompanion.hexagon.com/customers/s/article/msc-marc-volume-a--theory-and-user-information-doc9245
6. Matviichuk, V., Nesterenkov, V., Berdnikova, O. (2022) Determining the influence of technological parameters of the electron-beam surfacing process on quality indicators. *Eastern-European J. of Enterprise Technologies*, **1**, 21–30. DOI: https://doi.org/10.15587/1729-4061.2022.253473

ORCID

V.A. Matviichuk: 0000-0002-9304-6862

CORRESPONDING AUTHOR

V.A. Matviichuk
E.O. Paton Electric Welding Institute of the NASU
11 Kazymyr Malevych Str., 03150, Kyiv, Ukraine.
E-mail: matviychuk@technobeam.com.ua

SUGGESTED CITATION

V.A. Matviichuk (2025) Compensation of spatial deformation in products at additive electron beam surfacing. *The Paton Welding J*., **1**, 10–14.
DOI: https://doi.org/10.37434/tpwj2025.01.02

JOURNAL HOME PAGE

https://patonpublishinghouse.com/eng/journals/tpwj

Received: 12.06.2024
Received in revised form: 14.10.2024
Accepted: 23.01.2025

DOI: https://doi.org/10.37434/tpwj2025.01.03

PECULIARITIES OF CALCULATION OF STRESS CONCENTRATION FACTORS IN THIN-SHEET BUTT WELDED JOINTS WITH THE CONSIDERATION OF INITIAL ANGULAR DEFORMATION

A.V. Moltasov, P.M. Tkach, M.M. Dyman, V.G. Kot, I.G. Tkach

E.O. Paton Electric Welding Institute of the NASU
11 Kazymyr Malevych Str., 03150, Kyiv, Ukraine

ABSTRACT

The paper is devoted to studying the influence of initial angular deformation caused by uneven transverse sagging of the butt weld during cooling on the stress concentration factors (SCF) in the transition zones from the face reinforcement and the weld root to the base metal (BM). An analysis of the existing formulas was carried out to determine the factor that considers the influence of initial angular deformation on the SCF on the fusion line of the weld with the BM. An analysis of the available formulas was carried out to determine the factor that takes into account the effect of initial angular deformation on the SCF on the fusion line of the weld with the BM. As a result, it was found that these formulas were developed for joints with a butt weld symmetrical relative to the median plane of the plates being welded and cannot be used for calculations near the weld root. A theoretical justification is given that initial angular deformation should lead to a decrease in stresses on the root side of the joint. New analytical formulas for the determination of the SCF on the fusion line of the weld root with the BM are proposed, considering initial angular deformation. A specific example was used to show that the presence of initial angular deformation really results in a decrease in stresses on the root side of the joint. The results of analytical calculations were confirmed by numerical calculations using the finite element method.

KEYWORDS: butt welded joint, angular deformation, stress concentration, tension, bending, weld root

INTRODUCTION

During fusion welding of butt welds without edge preparation or with V-shaped edge preparation, the amount of molten metal grows from the back to the facial side of the joint, which causes uneven transverse sagging across the thickness of the joined plates during cooling [1]. As a result, the parts of the joint parallel to the welding are rotated relative to each other by an angle γ, forming an angle between the facial surfaces of < 180° (Figure 1).

Such deviations in geometric shape lead to an increase in stresses in welded joints under their axial loading due to the occurrence of additional bending stresses [2]. It is shown [3], that deviations in the geometric shape occurring during welding have a significant negative impact on fatigue life, especially for thin-sheet structures with low bending stiffness.

Since stress concentration is one of the basic factors that determine the fatigue resistance of welded joints [4], the justification of a procedure for correct assessing the effect of initial angular deformation on the stress concentration factors (SCF) in the transition zones from structural elements of a butt weld to the base metal (BM) is a relevant scientific and technical task in the field of strength, reliability and durability of welded structures.

ANALYSIS OF EXISTING APPROACHES AND MODERN CALCULATIONS

Taking into account the translational and angular mutual displacements of welded plates during the formation of a butt joint, the generalised formula for determination of the theoretical SCF is as follows [5]:

$$\alpha_\sigma = \alpha_{\sigma w} \alpha_m \alpha_\gamma, \quad (1)$$

where $\alpha_{\sigma w}$, α_m and α_γ are the SCF from the weld shape, transverse displacement of welded edges and angular deformation, respectively.

To determine the factor α_γ in joints with a weld symmetrical relative to the median surface of the joined plates, the following formula was proposed in [6]:

$$\alpha_\gamma = 1 + \frac{3l}{\delta} \sin\gamma, \quad (2)$$

where $l/2$ is the distance from the weld edge to the point of application of the axial load P; δ is the thickness of the joined plates (Figure 2).

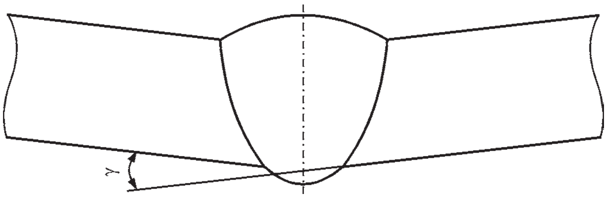

Figure 1. Angular displacement as a result of uneven transverse sagging of the metal during the formation of a butt weld

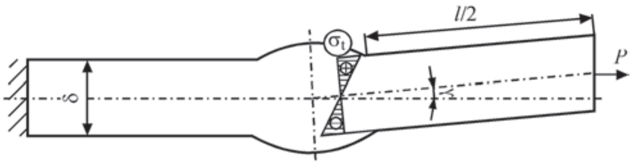

Figure 2. Calculation scheme of a butt welded joint with symmetrical reinforcement and initial angular deformation

According to the recommendations of the International Institute of Welding (IIW) [7], to determine α_γ, the following formula is used:

$$\alpha_\gamma = 1 + \frac{3l\gamma}{\delta}\frac{\tanh(\beta)}{\beta}, \tag{3}$$

where the non-linear factor depending on β takes into account the effect of reducing the initial angle γ as a result of the vertical displacement of the section, to which the axial force is applied [8].

Given that the angle usually does not exceed 5° [9], we can take $\sin\gamma \approx \gamma$ up to the fourth decimal place. Thus, without taking into account the effect of rectification, formulas (2) and (3) can be considered identical.

Considering Figure 2, it can be clearly seen that due to the angular deformation under the action of the axial force P, a bending moment M_γ also occurs, which on the fusion line of weld metal (WM) with the BM will be determined by the formula:

$$M_\gamma^f = \frac{Pl}{2}\sin\gamma. \tag{4}$$

Then, tensile stresses from the axial force in the section corresponding to the fusion line are:

$$\sigma^T = \frac{P}{b\delta},$$

and the bending stress in this section from the action of the bending moment is:

$$\sigma^B = \frac{3Pl}{b\delta^2}\sin\gamma,$$

where T is the tensile; B is bending; b is the width of the joined plates.

Therefore, the total stress on the upper side of the joint will be determined as the sum of tensile and bending stresses:

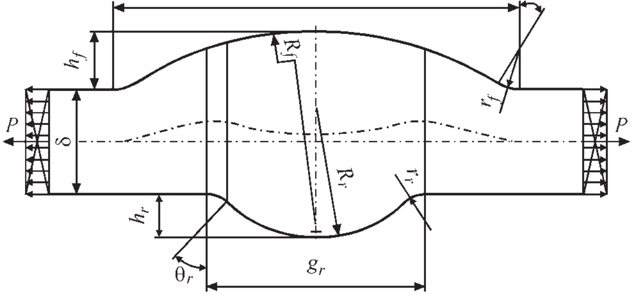

Figure 3. Geometric parameters of an idealised model of a butt joint made by one-sided fusion welding

$$\sigma^\Sigma = \frac{P}{b\delta}\left(1 + \frac{3l}{\delta}\sin\gamma\right). \tag{5}$$

As we can see, in the brackets of formula (5), we have the factor α_γ from the formula (2).

Since [6] considered a symmetrical weld, the stresses on the lower side of the joint left ignored, because it is obvious that they will show the difference in tensile and bending stresses (see the diagram in Figure 2) and will be less than stresses on the upper side. At the same time, in [10, 11], when calculating the SCF on the root side of the joints made by one-sided welding, the SCF from the weld shape was also multiplied by the SCF from the angular deformation, as a result of which the total SCF increased, although in fact the initial angular deformation should lead to its reduction near the weld root.

It is known [12, 13] that under both static and cyclic loads, the fracture of thin-sheet welded joints begins namely in the transition zones from the weld root to the BM, so it is necessary to quantitatively consider the effect of initial angular deformation on the value of stresses in these zones.

THEORETICAL FUNDAMENTALS FOR DETERMINATION OF SCF NEAR THE WELD ROOT

According to [14], the bending moment caused by the eccentricity of the axial load applied in the area with the weld on the fusion line of the weld root with the BM in a butt joint without initial angular deformation (Figure 3) will be determined by the formula:

$$M_e = \frac{P}{2}\left(h_f - R_f + \sqrt{R_f^2 - \frac{g_r^2}{4}}\right), \tag{6}$$

where h_f is the height of the facial reinforcement; R_f is the radius of the convex part of the facial reinforcement; g_r is the width of the weld root.

Taking into account the distance between the fusion lines of the facial reinforcement and the weld root with the BM, which is $(g_f - g_r)/2$ (see Figure 3), the bending moment from the initial angular deformation on the fusion line of the weld root with the BM will be determined by the formula:

$$M_\gamma^r = \frac{P\left(l + g_f - g_r\right)}{2}\sin\gamma, \tag{7}$$

where g_f is the width of the facial reinforcement.

Since the direction of the bending moment associated with the initial angular deformation is opposite to the direction of the moment caused by the eccentricity, the final moment on the fusion line of the weld root with the BM is determined as the difference of moments (6) and (7):

$$M = M_e - M_\gamma^r = \\ = \frac{P}{2}\left[h_f - R_f + \sqrt{R_f^2 - \frac{g_r^2}{4}} - \left(l + g_f - g_r\right)\sin\gamma\right]. \quad (8)$$

If we introduce:

$$m = \delta + h_f - R_f + \sqrt{R_f^2 - \frac{g_r^2}{4}},$$

then, the bending stress on the fusion line of the weld root with the BM for joining a unit width according to [14] at $b_0 \leq \delta/2$ is determined by the formula:

$$\sigma_r^B = \\ = \frac{Mm}{2r_r\left[\left(r_r + \frac{m}{2}\right)^2 \ln\frac{r_r + b_0}{r_r} - b_0\left(r_r + m\right) + \frac{b_0^2}{2} + \frac{m^3 + \left(m - 2b_0\right)^3}{24\left(r_r + b_0\right)}\right]}, \quad (9)$$

and at $b_0 > \delta/2$ — by the formula:

$$\sigma_r^B = \\ = \frac{Mm}{2r_r\left[\left(r_r + \frac{m}{2}\right)^2 \ln\frac{2r_r + m}{2r_r} - \frac{m}{2}\left(r_r + m\right) + \frac{m^2}{8} + \frac{m^3}{12\left(2r_r + m\right)}\right]}, \quad (10)$$

where r_r is the radius of the transition arc from the weld root to the BM; b_0 is a parameter that characterizes the concentrator sharpness near the weld root and is determined by the formula:

$$b_0 = 4\sqrt{2}\frac{r_r h_r}{\sqrt{g_r^2 + 4h_r^2}},$$

where h_r is the height of the weld root.

Substituting the expression for bending moment (8) into (9) and (10), we obtain formulas for the determination of bending stresses on the fusion line of the weld root with the BM in the joint with initial angular deformation, respectively, at $b_0 \leq \delta/2$:

$$\sigma_r^B = \\ = \frac{P\left[m - \delta - \left(l + g_f - g_r\right)\sin\gamma\right]m}{4r_r\left[\left(r_r + \frac{m}{2}\right)^2 \ln\frac{r_r + b_0}{r_r} - b_0\left(r_r + m\right) + \frac{b_0^2}{2} + \frac{m^3 + \left(m - 2b_0\right)^3}{24\left(r_r + b_0\right)}\right]} \quad (11)$$

and at $b_0 > \delta/2$

$$\sigma_r^B = \\ = \frac{P\left[m - \delta - \left(l + g_f - g_r\right)\sin\gamma\right]m}{4r_r\left[\left(r_r + \frac{m}{2}\right)^2 \ln\frac{2r_r + m}{2r_r} - \frac{m}{2}\left(r_r + m\right) + \frac{m^2}{8} + \frac{m^3}{12\left(2r_r + m\right)}\right]}. \quad (12)$$

The tensile stresses on the fusion line of the weld root with the BM at $b_0 \leq \delta/2$ and at $b_0 > \delta/2$ are determined, respectively, by the following formulas [14]:

$$\sigma_r^T = \frac{P}{r_r\left(\ln\frac{r_r + b_0}{r_r} + \frac{m - b_0}{r_r + b_0}\right)} \quad (13)$$

and

$$\sigma_r^T = \frac{P}{r_r\left(\ln\frac{2r_r + m}{2r_r} + \frac{m}{2r_r + m}\right)}. \quad (14)$$

Therefore, the theoretical SCF on the fusion line of the weld root with the BM at $b_0 \leq \delta/2$ will be determined as the ratio of the sum of bending (11) and tensile stresses to the nominal stress $\sigma_{nom} = P/\delta$ (13):

$$\alpha_\sigma^r = \frac{\delta}{r_r}\left(\frac{1}{\ln\frac{r_r + b_0}{r_r} + \frac{m - b_0}{r_r + b_0}} + \right. \\ \left. + \frac{m\left[m - \delta - \left(l + g_f - g_r\right)\sin\gamma\right]}{4\left[\left(r_r + \frac{m}{2}\right)^2 \ln\frac{r_r + b_0}{r_r} - b_0\left(r_r + m\right) + \frac{b_0^2}{2} + \frac{m^3 + \left(m - 2b_0\right)^3}{24\left(r_r + b_0\right)}\right]}\right), \quad (15)$$

and at $b_0 > \delta/2$ — of the sum of stresses (12) and (14):

$$\alpha_\sigma^r = \frac{\delta}{r_r}\left(\frac{1}{\ln\frac{2r_r + m}{2r_r} + \frac{m}{2r_r + m}} + \right. \\ \left. + \frac{m\left[m - \delta - \left(l + g_f - g_r\right)\sin\gamma\right]}{4\left[\left(r_r + \frac{m}{2}\right)^2 \ln\frac{2r_r + m}{2r_r} - \frac{m}{2}\left(r_r + m\right) + \frac{m^2}{8} + \frac{m^3}{12\left(2r_r + m\right)}\right]}\right). \quad (16)$$

REFINED APPROACH TO DETERMINATION OF SCF ON THE FACIAL SIDE OF A JOINT

The use of formulas such as (1), which involve multiplying the theoretical SCF at tension by other factors considering additional bending stresses, is not fully correct, since it is known [15] that the theoretical SCFs for tensile and bending stresses in the same concentrator are different.

According to [16], the bending stress on the fusion line of the facial reinforcement with the BM for joining a unit width at $a_0 \leq \delta/2$ is determined by the formula:

$$\sigma_f^B = \\ = \frac{M\delta}{2r_f\left[\left(r_f + \frac{\delta}{2}\right)^2 \ln\frac{r_f + a_0}{r_f} - a_0\left(r_f + \delta\right) + \frac{a_0^2}{2} + \frac{\delta^3 + \left(\delta - 2a_0\right)^3}{24\left(r_f + a_0\right)}\right]}, \quad (17)$$

and at $a_0 > \delta/2$ — by the formula:

$$\sigma_f^B = \\ = \frac{M\delta}{2r_f\left[\left(r_f + \frac{\delta}{2}\right)^2 \ln\frac{2r_f + \delta}{2r_f} - \frac{\delta}{2}\left(r_f + \delta\right) + \frac{\delta^2}{8} + \frac{\delta^3}{12\left(2r_f + \delta\right)}\right]}, \quad (18)$$

where r_f is the radius of the transition arc from the facial reinforcement to the BM; a_0 is a parameter that characterises the concentrator sharpness near the facial reinforcement and is determined by the formula:

$$a_0 = 4\sqrt{2}\frac{r_f h_f}{\sqrt{g_f^2 + 4h_f^2}}.$$

The tensile stresses on the fusion line of the facial reinforcement with the BM at $a_0 \le \delta/2$ and at $a_0 > \delta/2$ are determined, respectively, by the following formulas [16]:

$$\sigma_f^T = \frac{P}{r_f\left(\ln\frac{r_f + a_0}{r_f} + \frac{\delta - a_0}{r_f + a_0}\right)} \qquad (19)$$

and

$$\sigma_f^T = \frac{P}{r_f\left(\ln\frac{2r_f + \delta}{2r_f} + \frac{\delta}{2r_f + \delta}\right)}. \qquad (20)$$

It is obvious that the eccentricity on the fusion line is equal to zero, so the bending moment at this point is caused only by the initial angular deformation and is determined by the formula (4).

Since the direction of stresses from the bending moment caused by the initial angular deformation on the facial side of the joint coincides with the direction of stresses from the axial force, the theoretical SCF on the fusion line of the facial reinforcement with the BM at $a_0 \le \delta/2$ will be determined as the ratio of the sum of bending stresses (17), taking into account (4) and tensile stresses (19), to the nominal stresses:

$$\alpha_\sigma^f = \frac{\delta}{r_f}\left(\frac{1}{\ln\frac{r_f + a_0}{r_f} + \frac{\delta - a_0}{r_f + a_0}} + \frac{\delta l \sin\gamma}{4\left[\left(r_f + \frac{\delta}{2}\right)^2 \ln\frac{r_f + a_0}{r_f} - a_0\left(r_f + \delta\right) + \frac{a_0^2}{2} + \frac{\delta^3 + \left(\delta - 2a_0\right)^3}{24\left(r_f + a_0\right)}\right]}\right), \qquad (21)$$

and at $a_0 > \delta/2$ — of the sum of stresses (18), taking into account (4) and (20):

$$\alpha_\sigma^f = \frac{\delta}{r_f}\left(\frac{1}{\ln\frac{2r_f + \delta}{2r_f} + \frac{\delta}{2r_f + \delta}} + \frac{\delta l \sin\gamma}{4\left[\left(r_f + \frac{\delta}{2}\right)^2 \ln\frac{2r_f + \delta}{2r_f} - \frac{\delta}{2}\left(r_f + \delta\right) + \frac{\delta^2}{8} + \frac{\delta^3}{12\left(2r_f + \delta\right)}\right]}\right). \qquad (22)$$

CALCULATION RESULTS AND THEIR DISCUSSION

Let us consider a butt welded joint of aluminium AMg6M alloy with a thickness of 1.8 mm, for which theoretical SCFs were calculated in [14] on the fusion lines of the facial reinforcement and the weld root with the BM without considering the initial angular deformation (Table 1), and postulate the initial angular deformation $\gamma = 2°$ and the distance from the fusion line of the facial reinforcement with the BM to the point of applying the axial load $l/2 = 3$ mm.

Since $b_0 \le \delta/2$ (see Table 1), the SCF on the fusion line of the weld root with the BM in the studied joint will be determined by formula (15), and as a result, it will be found to be 1.92. If we introduce $\gamma = 0$ in formula (15), we find that in a similar joint without initial angular deformation, the SCF on the fusion line of the weld root is 2.4, which is confirmed by the results of the finite element method (FEM) calculations conducted in [14]. Thus, the presence of initial angular deformation leads to a 20 % reduction in stresses near the weld root.

Also, for this joint $a_0 \le \delta/2$ (see Table 1), so the SCF on the fusion line of the facial reinforcement with the BM will be determined by formula (21), and as a result, it will be found to be 2.14. Introducing $\gamma = 0$ in formula (21), we find that in a similar joint without initial angular deformation, the SCF on the fusion line of the facial reinforcement with the BM is 1.62, which is also confirmed by the results of the FEM calculations carried out in [14]. Thus, the initial angular deformation leads to a 32 % increase in stresses on the facial side of the joint.

The obtained analytical results are in good agreement with the results of numerical calculations by the finite element method (FEM), according to which the maximum stress near the weld root was 2.01 MPa, and near the reinforcement — 2.22 MPa (Figure 4).

Table 1. Geometric dimensions of structural elements of butt joint weld of aluminium AMg6M alloy made by TIG welding

Joint side	Projection width g, mm	Projection height h, mm	Radius of transition from WM to BM r, mm	Radius of the convex part R, mm	Concentrator sharpness parameter a_0 (b_0), mm
Facial (f)	7.000	1.000	0.690	5.935	0.536
Root (r)	3.750	0.750	0.490	2.229	0.515

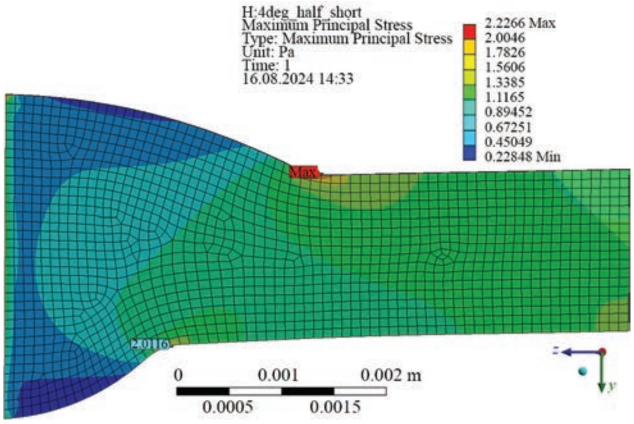

Figure 4. Calculated stress fields in the studied joint with initial angular deformation obtained by FEM

Thus, the stress on the facial side of the joint differ by 3.8 %, and on its root side — by 4.7 %.

The applied axial load was 1.8 N in order that the rated stress in a 1.8 mm thick joint of a unit width was 1 MPa. Thus, the obtained stress values in the concentrator zones were equal to the values of the corresponding SCF, which helped to simplify the comparison of analytical and numerical results.

To prevent the influence of the finite element mesh sizes on the values of maximum local stresses, it was refined during the analysis until the difference between the stress values in the final and previous models was less than 5 % [17]. As a result, the linear size of the final model element was 0.1 mm, and the model itself had 16848 elements with 70308 nodes.

Since $\alpha_m = 1$, the total SCF $\alpha_\sigma = 2.14$, and the theoretical SCF of the weld shape $\alpha_{\sigma w} = 1.62$, according to formula (1), the SCF of angular deformation α_γ according to the refined theory is 1.32, and according to formula (2), which does not take into account the difference between the SCF at tension and bending, this value is almost 1.35. It is expected that the refined calculations are less conservative, as far as for butt welded joints, the SCF at bending is slightly lower than the SCF at tension [18].

CONCLUSIONS

1. An analysis of existing formulas was carried out to determine the factors that take into account the influence of initial angular deformation caused by uneven thermal sagging of butt welds across the joint thickness on the total stress concentration. Taking into account the nature of the analysed formulas, it was theoretically justified that initial angular deformation should lead not only to an increase in stresses on the facial side of the joints, but also to their decrease on the root side.

2. For the first time, analytical formulas for determination of the theoretical stress concentration factor on the fusion line of the weld root with the base metal, which take into account the initial angular deformation, were obtained.

3. The analytical formulas for evaluating the effect of initial angular deformation on the theoretical stress concentration factor on the fusion line of the facial weld reinforcement with the base metal were improved in terms of considering the difference between the stress concentration factors of tensile and bending stresses.

4. On the example of a thin-sheet butt welded joint of aluminium AMg6M alloy, made by TIG welding, it is shown that the presence of initial angular deformation with a value of 2° leads to an increase in stresses on the facial side of the joint by 32 % and to their decrease by 20 % near the weld root compared to the joint without initial angular deformation. The obtained results are confirmed by numerical calculations using the finite element method with a discrepancy of not more than 5 %.

REFERENCES

1. Vershinsky, S.V., Vinokurov, V.A., Kurkin, S.A. et al. (1975) *Design of welded structures in mechanical engineering*. Ed. by S.A. Kurkin. Moscow, Mashinostroenie [in Russian].
2. Zhu, J., Barsoum, I., Barsoum, Z., Khurshid, M. (2022) Evaluation of local stress-based fatigue strength assessment methods for cover plates and T-joints subjected to axial and bending loading. *Fatigue and Fracture of Engineering Materials and Structures*, 9 (**45**), 2531–2548. DOI: https://doi.org/10.1111/ffe.13764
3. Remes, H., Romanoff, J., Lillemäe, I. et al. (2017) Factors affecting the fatigue strength of thin-plates in large structures. *Inter. J. Fatigue*, **101**, 397–407. DOI: https://doi.org/10.1016/j.ijfatigue.2016.11.019
4. Trufiakov, V.I., Dvoretsky, V.I., Mikheev, P.P. et al. (1990) *Strength of welded joints under variable loads*. Ed. by V.I. Trufiakov. Kyiv, Naukova Dumka [in Russian].
5. Makarov, I.I. (1977) Method of calculating the coefficient of stress concentration in butt-welded joints. *Welding Production*, 4(**24**), 6–8.
6. Colchen, D. (1999) Actual effect of weld defects on the fatigue behavior of aluminium butt welds. *Welding in the World*, 6(**43**), 25–32.
7. Hobbacher, A.F. (2016) *Recommendations for fatigue design of welded joints and components*. 2nd Ed., Berlin, Springer. DOI: https://doi.org/10.1007/978-3-319-23757-2
8. Lillemäe, I., Lammi, H., Molter, L., Remes, H. (2012) Fatigue strength of welded butt joints in thin and slender specimens. *Inter. J. Fatigue*, **44**, 98–106. DOI: https://doi. org/10.1016/j.ijfatigue.2012.05.009
9. Mancini, F., Remes, H., Romanoff, J., Reinaldo Goncalves, B. (2020) Stress magnification factor for angular misalignment between plates with welding-induced curvature. *Welding in the World*, 4(**64**), 729–751. DOI: https://doi.org/10.1007/s40194-020-00866-7
10. Knysh, V.V., Klochkov, I.N., Pashulya, M.P., Motrunich, S.I. (2014) Increase of fatigue resistance of sheet welded joints of aluminum alloys using high-frequency peening. *The Paton Welding J.*, **5**, 21–27. DOI: https://doi.org/10.15407/tpwj2014.05.04

11. Knysh, V.V., Solovei, S.A. (2017) *Improving the durability of welded joints with fatigue damage*: Monography. Kyiv, Politekhnika [in Russian].
12. Lukianenko, A., Labur, T.M., Pokliatskyi, A.G. et al. (2019) Investigation of fatigue strength and norms of emission of harmful substances in the air during MIG and TIG welding of 1460 aluminum-lithium alloy. *FME Transact*., 3(**47**), 608–612. DOI: https://doi.org/10.5937/fmet1903608L
13. Motrunich, S., Klochkov, I., Pokliatsky, A. (2020) High cycle fatigue behaviour of thin sheet joints of aluminium-lithium alloys under constant and variable amplitude loading. *Welding in the World*, 12(**64**), 1971–1979. DOI: https://doi.org/10.1007/s40194-020-00976-2
14. Moltasov, A., Tkach, P., Ustynenko, O., Protasov, R. (2022) Effect of load eccentricity on stress condition of butt welded joint with asymmetrical reinforcement. *Strojnicky Casopis*, 1(**72**), 99–108. DOI: https://doi.org/10.2478/scjme-2022-0010
15. Goyal, R., El-Zein, M., Glinka, G. (2016) A robust stress analysis method for fatigue life prediction of welded structures. *Welding in the World*, 2(**60**), 299–314. DOI: https://doi.org/10.1007/s40194-016-0295-y
16. Moltasov, A.V. (2019) Stressed state of a butt-welded joint with regard for displacements of the centers of inertia. *Mater. Sci*., 3(**55**), 358–366. DOI: https://doi.org/10.1007/s11003-019-00310-2
17. Baumgartner, J., Bruder, T. (2013) An efficient meshing approach for the calculation of notch stresses. *Welding in the World*, 57(**1**), 137–145.
18. Molski, K.L., Tarasiuk, P. (2020) Stress concentration factors for butt-welded plates subjected to tensile, bending and shearing loads. *Materials*, 13(**8**), 1798.

ORCID

A.V. Moltasov: 0000-0002-5025-4055,
P.M. Tkach: 0000-0002-1069-4128,
M.M. Dyman: 0000-0002-5886-1124,
V.G. Kot: 0000-0002-4759-9992,
I.G. Tkach: 0009-0007-1026-9205

CONFLICT OF INTEREST

The Authors declare no conflict of interest

CORRESPONDING AUTHOR

A.V. Moltasov
E.O. Paton Electric Welding Institute of the NASU
11 Kazymyr Malevych Str., 03150, Kyiv, Ukraine.
E-mail: moltasov@gmail.com

SUGGESTED CITATION

A.V. Moltasov, P.M. Tkach, M.M. Dyman, V.G. Kot, I.G. Tkach (2025) Peculiarities of calculation of stress concentration factors in thin-sheet butt welded joints with the consideration of initial angular deformation. *The Paton Welding J*., **1**, 15–20.
DOI: https://doi.org/10.37434/tpwj2025.01.03

JOURNAL HOME PAGE

https://patonpublishinghouse.com/eng/journals/tpwj

Received: 25.09.2024
Received in revised form: 22.10.2024
Accepted: 22.01.2025

Welding Exhibitions in Europe in 2025

WELDING Kielce
25–28 March 2025, Kielce, Poland
Trade fair for welding technology
https://www.targikielce.pl/en/industrial-spring/welding

International Industrial Forum
27–29 May 2025, Kyiv, Ukraine, International Exhibition Centre Forum of the metal working, welding, machine building and related fields
https://www.iec-expo.com.ua/en/pfen-2025.html

LAMIERA 2025
May 07–10, 2025, Milan, Italy,
Fiera Milano, Rho
Machines, Plants, Tools for Machining Sheets, Tubes, Sections Wires and Steel Structural Work, the Dies, Welding, Heat Treatments, Surface Treatments and Finishing

Welding Poznań
03–06 June 2025, Poznan, Poland
International Trade Fair for Welding
https://www.tradefairdates.com/Welding-M3150/Pozna.html

Metal Show & TIB Bucharest
13–16 May 2025, Bucharest, Romania
Fair of the metalworking industry and international technical fair
https://www.ntradeshows.com/tib-bucharest/

Schweissen & Schneiden Essen
15–19 September 2025, Essen, Germany
World Leading Fair for Joining, Cutting, and Coating
https://www.schweissen-schneiden.com/joining-cutting-surfacing/

DOI: https://doi.org/10.37434/tpwj2025.01.04

MASTERING THE TECHNOLOGY OF PRODUCING INGOTS FROM HEAT-RESISTANT ALLOYS KhN38VT AND KhN60VT BY THE ELECTRON BEAM MELTING METHOD

S.V. Akhonin[1], **V.O. Berezos**[1], **M.I. Medvedev**[2], **O.S. Bobukh**[2], **D.S. Ivanov**[3], **O.G. Yerokhin**[1]

[1]E.O. Paton Electric Welding Institute of the NASU
11 Kazymyr Malevych Str., 03150, Kyiv, Ukraine
[2]Ukrainian State University of Science and Technologies
2 Lazaryan Str., 49010, Dnipro, Ukraine
[3]Zaporizhzhia Casting-Mechanical Plant
72 Pivdenne Prosp., 69008, Zaporizhzhia, Ukraine

ABSTRACT

In order to optimize the technology of production of nickel- and iron-based heat-resistant alloys, the E.O. Paton Electric Welding Institute conducted melting of a batch of ingots of Kh38VT and Kh60VT grades. The ingots were produced using the technology of cold hearth electron beam melting and portioned feed of liquid metal to a water-cooled crucible. The conducted work showed that the electron beam melting method allows producing high-quality defect-free ingots of nickel-based heat-resistant alloys that meet the requirements of the standards, and it can be used instead of secondary vacuum-arc remelting. When using ingots of primary induction remelting as the initial charge billet, it is not necessary to add alloying elements with high vapor pressure to ensure a chemical composition that meets GOST 5632–72. In addition, the level of mechanical properties of KhN60VT alloy bars almost completely satisfies the requirements of TU 14-3-571–2004 on "Seamless cold-deformed pipes from the KhN60VT (EI868) alloy and KhN60VT-VD alloy for the aviation industry".

KEYWORDS: heat-resistant alloy, charge billet, ingot, electron beam melting, cold hearth, refining, impurities, metal quality

INTRODUCTION

Development of new technological processes, ensuring removal of impurities, nonmetallic inclusions and the production of physically and chemically homogeneous ingots, is of great importance in improving the service and technological properties of heat-resistant steels [1].

Vacuum metallurgy has a prominent place among the metallurgical methods of improvement of the quality of steels and alloys [2, 3]. Vacuum melting of the metal, on the one hand, prevents its interaction with atmospheric gases, and on the other hand, intensifies the degassing and evaporation reactions. Moreover, remelting in a vacuum environment enables additional cleaning of the metal from nonmetallic inclusions, producing ingots and finished products with a homogeneous dense structure without any macrodefects [4].

New processes of electron beam melting (EBM) allow producing metal of an even higher quality [5, 6].

Electron beam melting, which combines the best features of vacuum-induction and vacuum-arc melting, is an efficient method of furnace vacuum metallurgy. At EBM the liquid metal contact with fire-resistant materials is absent, and the heating and melting processes are controlled independently of each other, that allows varying the liquid metal temperature and vacuuming time in a broad range [7]. These advantages in combination with continuous metal feed ensure producing ingots of maximally high purity with defect-free structure during EBW.

Application of EMB technology to improve the quality of special steels and complex alloys based on iron and nickel allows practically completely removing many of the low-melting impurities (lead, zinc, bismuth, tin, etc.) and even lowering the nonmetallic inclusion content simultaneously with an abrupt lowering of the content of hydrogen, nitrogen, and oxygen at remelting of these materials. Owing to a high degree of refining and formation of ingots with a more homogeneous structure and chemical composition, EBM results in an essential improvement of the physical-mechanical properties of the metals and alloys [8]. Their technological plasticity is increased, particularly at pressure treatment. So, remelting of tool and bearing steels provides: an improvement in hot deformability; lowering of the required degree of forging reduction and cracking sensitivity at heat treatment; improvement of polishedness and ductile properties [9].

MATERIALS AND EXPERIMENTAL PROCEDURE

In order to determine the degree of refining of heat-resistant nickel-based alloys and to optimize the technology of their production, PWI performed melting

Figure 1. Charge billets: *a* — KhN60VT; *b* — KhN38VT

of ingots of KhN38VT and KhN60VT grades. Nickel-based KhN60VT alloy is widely used in the aircraft industry. Ingots were produced by the technology of cold hearth EBM with portioned feed of liquid metal into a water-cooled crucible.

Test melts were conducted in UE5812 electron beam unit fitted with a cold hearth [10].

The technological sequence of melting the ingots consisted of the following stages: taking samples for control chemical analysis of the initial charge, preparation of the equipment and technological fixture for melting; forming the consumable billet; melting process; taking samples for chemical and gas analysis of the produced ingot.

SE "STC "Titan" of the E.O. Paton Electric Welding Institute of the NAS of Ukraine" performed melting of a batch of ingots of KhN60VT and KhN38VT grades.

Charge billets for producing ingots of KhN60VT and KhN38VT grades were ingots of primary induction remelting (Figure 1).

The head parts of the initial billets had a certain amount of crystallized slag in their composition (Figure 2).

Figure 2. Appearance of the head part of the initial charge billet

Compared to a VAR ingot, an EBM ingot does not require any additional surface treatment (cutter turning or surface melting by an arc), or removal of the ingot crop part.

Experience of producing nickel-based heat-resistant alloys by cold hearth EBM showed that at a sufficiently large amount of slag in the initial charge it penetrates into the cold health. When slag accumulates in the cold hearth, the drain spout is blocked, thus creating the conditions which make pouring of the liquid melt into the crucible more complicated. Moreover, the cold hearth is not capable of holding up the all the liquid slag accumulated during melting, and its certain amount penetrates into the liquid metal melt in the crucible. At pouring of the next melt portion into the crucible, slag entrapment in the liquid melt at the cold walls of the crucible may occur, thus impairing the ingot surface quality.

Thus, in order to prevent ingress of a large amount of slag into the ingot melting and crystallization zone, the initial billets are loaded into the unit so that remelting occurred from the bottom part at the start of melting to the head part at the end of melting.

The consumable billet was loaded into the electron beam unit box by the shop crane.

After loading in the charge billet and preparation of the unit for melting, it was sealed and pumped down. Upon reaching the working pressure in the melting chamber of $1.33\cdot10^{-2}$–$6.66\cdot10^{-3}$ Pa, leakage into the chamber working volume was determined. The admissible leakage value is not higher than 30 μm·l/s.

The essence of the process (Figure 3) consisted in the horizontal feed of consumable billet *6*, at a set speed into the melting zone, its melting by the electron beams above cold hearth *7*. As the cold hearth was filled, the liquid metal was poured into crucible *8*, where ingot *9* of the required length was formed.

Deposition of a new layer of the skull in the cold hearth was performed for each ingot (Figure 4).

During melting, the initial charge was continuously fed into the working area above the cold hearth,

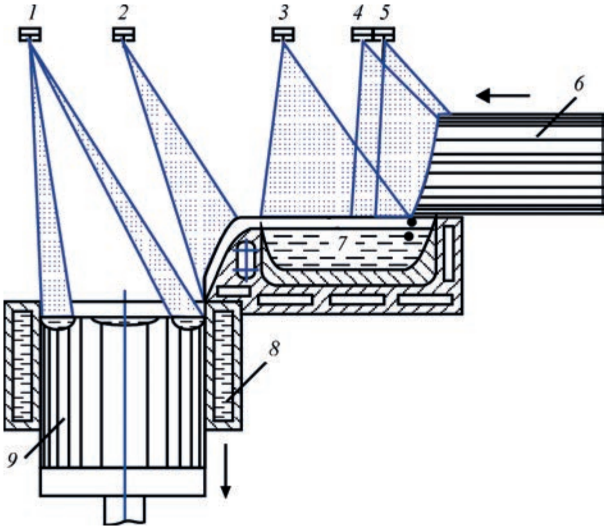

Figure 3. Schematic of cold hearth electron beam melting: *1–5* — electron beam guns; *6* — consumable charge billet; *7* — cold hearth; *8* — crucible; *9* — ingot

Figure 4. Appearance of skull

where its smelting occurred under the effect of electron beam heating. The melting process was stable, however, precipitation of a considerable amount of slag was observed, which stayed in the cold hearth in the melting zone. Slag penetration into the liquid melt in the crucible in small amounts was also observed (Figure 5).

In order to improve the processes of refining from impurities and inclusions at melting of ingots of nickel-based heat-resistant alloys, the time of liquid metal soaking in the cold hearth and the crucible was extended, due to lowering the melting productivity from 280 to 240 kg/h.

During melting, in keeping with the conducted calculations for determination of optimal melting modes, the following technological parameters were kept constant: melting rate, time between portion pouring, and portion height in the crucible. Ingot heating in the crucible was conducted by scanning over the surface with the beam of electron beam guns. During melting the electron beam moved over the upper end face of the formed ingot in the zone of the melt contact with the working surface of the crucible inner part, providing deeper penetration of the ingot surface, melting up of the present casting defects and compensation of heat removal into the crucible that had a positive impact on the structure. Numerical values of the technological parameters for ingots of 400 mm diameter are given below.

Technological parameters of melting 400 mm diameter ingots

Melting rate, kg/h	240
Time between pouring the portions, s	60
Height of portions in crucible simultaneously, mm	4
Power of the 1st gun, kW	90
Power of the 2nd gun, kW	90
Power of the 3rd gun, kW	90
Power of the 4th gun, kW	150
Power of the 5th gun, kW	150

Rate and power of metal deposition into the cold hearth and crucible were kept constant. The process of smelting the initial charge billets was continued up to approaching the zone of the head part melting. This moment was clearly observed at penetration of slag into the melting zone, located in the head part of the initial billet. Here, intensive metal sputtering and bright glowing of the melting slag were observed (Figure 6). At that moment the process of melting of the initial charge billet stopped.

At the end of melting, removal of the shrinkage cavity was performed by gradually lowering the power of heating the ingot upper end face in the crucible.

Ingots of nickel-based heat-resistant KhN60VT and KhN38VT alloys with outer diameter of 400 mm

Figure 5. Process of EBM of nickel-based heat-resistant KhN60VT alloy

Figure 6. Melting of slag contained in the initial charge billet

and up to 2000 mm length were produced as a result of the conducted melting operations (Figure 7).

The ingot surface quality as regards the presence of pores, cavities, nonmetallic inclusions and cracks was determined visually, without application of magnifying instruments. The side surface of the produced ingots after cooling for 6 h in vacuum was clean, without traces of tarnishing colours. The depth of surface defects of casting origin did not exceed 6 mm, defects in the form of tears, cracks or lacks-of-fusion were absent. Individual slag embedments were observed in the ingot surface layer (Figure 8).

Ingot facing was performed on a band saw.

The surface of the produced ingots was machined to remove casting defects. The ingots were stripped on DIP-500 lathe (Figure 9).

Thus, a technology of melting high-quality ingots of nickel-based heat-resistant alloys by the method of electron beam melting was optimized, which allows producing ingots with a satisfactory surface quality. The possibility of EBM application instead of VAR for remelting ingots of open induction melting is shown.

Figure 8. Quality of the cast surface of 400 mm dia ingot from heat-resistant KhN60VT alloy

Samples for ICP analysis were taken from the head, middle and bottom parts of the produced ingots. Samples were taken from the ingot side surface at its machining as follows: preliminary drilling to 2–3 mm depth, surface layer chips were thrown away. The sample was taken at further turning to the depth of 7–10 mm. Chip overheating when taking the samples was not allowed. No lubricating-cooling liquids were used when taking the samples. The selected samples were placed into paper bags with indication of melt number and sampling area. The weight of each sample was at least 20–30 g. Element content in the ingots was taken to be equal to mean arithmetic values of the results of measurements for all the samples.

The same procedure was used to select one point in the central part of each initial charge billet.

Chemical element content was determined by the method of inductively-coupled plasma-optical emission spectrometry (ICP-OES) in ICP-spectrometer ICAP 6500 DUO.

Figure 7. Finished ingots of 400 mm diameter from heat-resistant alloys: *a* — KhN60VT; *b* — KhN38VT

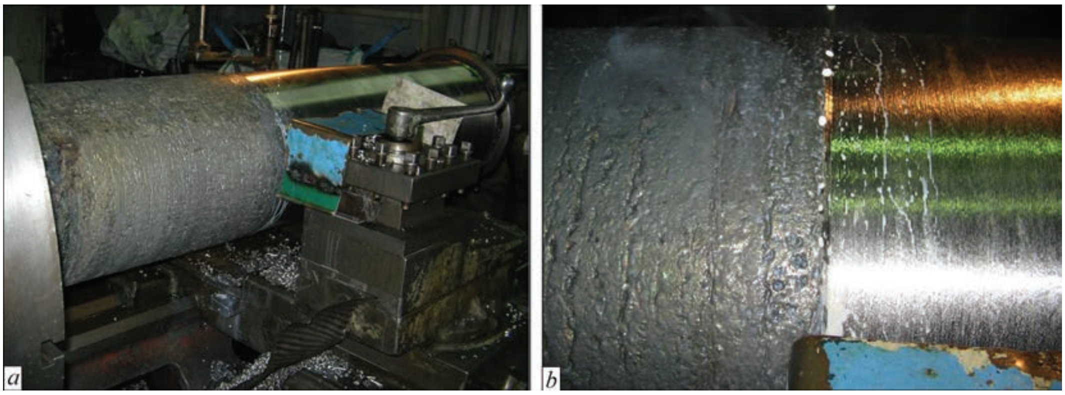

Figure 9. Machining of 400 mm dia. ingot from heat-resistant KhN60VT alloy

Table 1 shows the results of measurement of chemical composition of the initial charge billets and finished ingots by the main elements and impurities to GOST 5632–71.

In addition, measurements of the content of other impurities and modifiers were conducted (Table 2).

Analysis of the obtained results showed that at EBM of the initial billets manganese content decreases by 35 % for KhN38VT alloy and by 57 % for KhN60VT alloy. A significant lowering of the content of magnesium by 95 % and of silicon by 50 % also takes place in KhN60VT alloy. A certain increase of phosphorus content in KhN38VT alloy should be noted. As to the content of other chemical elements, there is no significant change in ingots of KhN60VT and KhN38VT alloys after electron beam remelting.

MI-99 samples of a cylindrical shape, in 4 mm diameter and length were prepared to determine the content of oxygen and nitrogen. Samples were made from blanks, cut out of the ingot end face chamfer.

Nitrogen and oxygen content in KhN60VT and KhN38VT ingots was determined in TC-500 analyzer. The principle of operation of the analyzer for nitrogen/oxygen determination consists in melting the analyzed sample in the graphite crucible of the furnace in a helium flow. Reaction of the released oxygen with

Table 1. Chemical composition of EBM ingots from KhN60VT, KhN38VT steels, wt.%

Grade	Sampling location	Fe	C	Si	Mn	Ni	Cr
KhN38VT	Initial	34.209	0.07	0.343	0.674	36.351	21.521
After EBM	1	34.709	0.11	0.357	0.435	35.802	21.131
	2	34.358	0.09	0.361	0.462	35.757	21.068
–	GOST 5632–72	31.08–41.44	0.06–0.12	<0.80	<0.70	35.0–39.0	20.0–23.0
KhN60VT	Initial	0.214	0.08	0.393	0.455	58.83	23.526
After EBM	1	0.218	0.09	0.198	0.194	59.13	23.363
	2	0.207	0.10	0.177	0.189	59.25	23.417
–	GOST 5632–72	<4.00	<0.10	<0.80	<0.50	50.874–63.200	23.50–26.50

Table 1 (Cont.)

Grade	Sampling location	W	Ti	Al	Ce	S	P
KhN38VT	Initial	3.450	0.856	0.460	<0.03	0.001	0.0065
After EBM	1	3.490	0.891	0.464	–»–	–»–	0.010
	2	3.370	0.926	0.461	–»–	–»–	0.013
–	GOST 5632–72	2.80–3.50	0.70–1.20	<0.50	–»–	<0.020	<0.030
KhN60VT	Initial	14.670	0.488	0.356	–»–	0.010	0.0081
After EBM	1	14.460	0.429	0.379	–»–	0.003	0.0050
	2	14.980	0.433	0.400	–»–	–»–	0.0060
–	GOST 5632–72	13.0–16.0	0.30–0.70	<0.50	–»–	<0.013	<0.013

Table 2. Content of impurities and modifiers in EBM ingots of KhN60VT, KhN38VT steels, wt.%

Grade	Sampling location	As	Ca	Cd	Ce	Co	Cu
KhN38VT	Initial	<0.001	0.010	<0.001	<0.03	0.020	0.047
After EBM	1	–»–	0.013	–»–	–»–	0.019	0.039
	2	–»–	0.011	–»–	–»–	–»–	0.040
KhN60VT	Initial	–»–	0.032	–»–	–»–	0.003	0.002
After EBM	1	–»–	0.009	–»–	–»–	0.002	–»–
	2	–»–	0.012	–»–	–»–	–»–	–»–

Table 2 (Cont.)

Grade	Sampling location	Mg	Mo	Nb	Pb	Sb	V
KhN38VT	Initial	0.005	0.155	0.013	0.003	0.017	0.010
After EBM	1	0.004	0.158	0.012	0.002	0.015	0.011
	2	–»–	0.160	0.016	0.003	–»–	–»–
KhN60VT	Initial	0.344	0.003	<0.001	0.004	0.013	<0.001
After EBM	1	0.014	0.006	0.002	0.003	0.017	–»–
	2	–»–	0.007	0.004	–»–	0.013	–»–

graphite results in formation of CO and partially CO_2. These gases, together with helium, are carried away and pass through a catalyst (CuO-based), where CO is oxidized to CO_2. The mixture passes through an infrared cell, which measures the lowering of the intensity of infrared radiation caused by CO_2 absorption that is proportional to oxygen content being determined.

The gas flow from the IR cell passes through "Lecosorb" catalyst, where CO_2 and H_2O are retained, while the remaining nitrogen is carried out in the helium flow to the thermoconductometric cell, where nitrogen content is determined by the principle of different conductivity of the two gases (detected mixture of nitrogen and helium against pure helium).

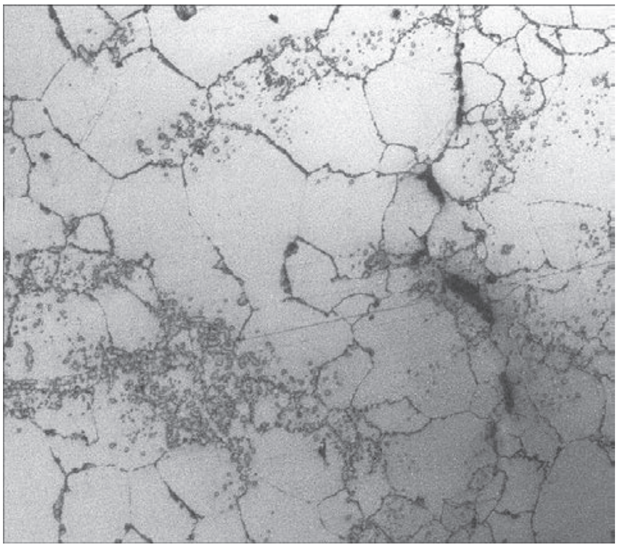

Figure 10. Macrostructure of a bar billet of 165 mm diameter from KhN60VT alloy (×100)

Table 3 shows the results of measuring oxygen and nitrogen content in KhN60VT and KhN38VT alloys.

As one can see from the Table, oxygen content decreases by 10–14 % for KhN38VT and KhN60VT alloys. Nitrogen content decreases by 8 % for KhN38VT metal and by 42 % for KhN60VT metal.

Research on fabrication of semi-finished products in the form of KhN60VT bars was conducted with the purpose of further study of metal quality.

Bars of 165 mm diameter were produced by forging from 400 mm dia ingots. Deformation processing of the ingots was conducted in the temperature range of 1170–900 °C.

Investigations of the produced bar billet of 165 mm diameter from KhN60VT alloy showed that the microstructure is austenitic, with grain size corresponding to 1–2 number of DERZHSTANDART 5639 (Figure 10).

Studies of mechanical properties of the produced metal were conducted by tensile testing of samples at

Table 3. Gas content in EBM ingots of KhN60VT, KhN38VT steels, wt.%

Grade	State	[O]	[N]
KhN38VT	Initial	0.0048	0.0084
	After EBM	0.0043	0.0078
KhN60VT	Initial	0.0048	0.026
	After EBM	0.0041	0.015

Table 4. Mechanical properties of 165 mm bars from KhN60VT alloy produced by EBM

Sample number	δ, %	ψ, %	σ_y, MPa	σ_t, MPa
1	68.4	70.2	311	749
2	67.4	65.9	323	756
3	67.6	70.9	303	745
TU 14-1-286–72	45–60	52–60	295–390	740–880

$T = 20$ °C. Results of the conducted tests (see Table 1) show that the metal of semi-finished products in the form of bars, obtained as a result of the performed work, meets the standard requirements. The bars are characterized by higher ductility. This may be related to the fact that the EBM process provides deeper removal of nonmetallic inclusions and lower values of gas content.

Performed work showed that the electron beam melting method allows producing sound defect-free ingots of nickel-based heat-resistant alloys that meet the standard requirements, and it can be used instead of secondary vacuum-arc remelting. At application of ingots of primary induction remelting as the initial charge billet, there is no need for adding to the charge the alloying elements with a high vapour pressure to ensure the chemical composition, meeting the requirements of GOST 5632–72. It should be further emphasized that the level of mechanical properties of the bars from KhN60VT alloy practically completely meets the requirements of TU 14-3-571–2004 for “Seamless cold-deformed pipes from the KhN60VT (EI868) alloy and KhN60VT-VD alloy for the aviation industry”.

REFERENCES

1. Bratkovsky, E.V., Zavodany, A.V. (2008) *Electrometallurgy of steel and special electrometallurgy*. Novotroitsk, NF MISiS [in Russian].
2. Zhouhua, J., Yanwu, D., Kuangdi, X. (2023) Vacuum Metallurgy. In: *The ECPH Encyclopedia of mining and metallurgy.* Ed. by Xu, K. Springer, Singapore. DOI: https://doi.org/10.1007/978-981-19-0740-1_1388-1
3. Voskoboynikov, V.G., Kudrin, V.A., Yakushev, A.M. (2002) *General metallurgy*: Textbook for universities. 6th Ed. Moscow, ICC Akademkniga [in Russian].
4. Kudrin, V.A. (2003) *Theory and technology of steel production*. Moscow, Mir [in Russian].
5. Paton, B.E., Trigub, N.P., Kozlitin, D.A. et al. (1997) *Electron beam melting*. Kyiv, Naukova Dumka [in Russian].
6. Ladokhin, S.V., Levitskyi, M.I., Chernyavskyi, V.B. et al. (2007) *Electron beam melting in foundry production*. Kyiv, Stal [in Russian].
7. Paton, B.E., Trigub, N.P., Akhonin, S.V. (2008) *Electron beam melting of refractory and highly reactive metals*. Kyiv, Naukova Dumka [in Russian].
8. Trigub, N.P., Akhonin, S.V. (1996) Optimization of smelting of steel and alloy ingots in an electron beam installation with an cold hearth. *Problemy Spets. Elektrometallurgii*, **2**, 12–17 [in Russian].
9. Movchan, B.A., Trigub, N.P., Gromov, V.I. et al. (1975) Purity and properties of SH15, 18H2N4VA and H18N10T steels, premelted in an electron beam furnace with an cold hearth. *Problemy Spets. Elektrometallurgii*, **1**, 48–50 [in Russian].
10. Trigub, N.P., Zhuk, G.V., Kornejchuk, V.D. et al. (2007) Industrial electron beam installation UE-5812. *Sovrem. Elektrometall.*, **1**, 11–14 [in Russian].

ORCID

S.V. Akhonin: 0000-0002-7746-2946,
V.O. Berezos: 0000-0002-5026-7366,
M.I. Medvedev: 0000-0002-1230-420X,
O.S. Bobukh: 0000-0001-7254-3854,
D.S. Ivanov: 0009-0000-6916-8109,
O.G. Yerokhin: 0000-0003-2105-5783

CONFLICT OF INTEREST

The Authors declare no conflict of interest

CORRESPONDING AUTHOR

V.O. Berezos
E.O. Paton Electric Welding Institute of the NASU
11 Kazymyr Malevych Str., 03150, Kyiv, Ukraine.
E-mail: titan.paton@gmail.com

SUGGESTED CITATION

S.V. Akhonin, V.O. Berezos, M.I. Medvedev, O.S. Bobukh, D.S. Ivanov, O.G. Yerokhin (2025) Mastering the technology of producing ingots from heat-resistant alloys KhN38VT and KhN60VT by the electron beam melting method.
The Paton Welding J., **1**, 21–27.
DOI: https://doi.org/10.37434/tpwj2025.01.04

JOURNAL HOME PAGE

https://patonpublishinghouse.com/eng/journals/tpwj

Received: 06.08.2024
Received in revised form: 11.09.2024
Accepted: 23.01.2025

DOI: https://doi.org/10.37434/tpwj2025.01.05

PRODUCTION OF FERROVANADIUM UNDER THE CONDITIONS OF ELECTROSLAG MELTING

Yu.V. Kostetskyi, E.O. Pedchenko, M.O. Vdovin, G.O. Polishko, V.L. Petrenko, V.A. Zaytsev

E.O. Paton Electric Welding Institute of the NASU
11 Kazymyr Malevych Str., 03150, Kyiv, Ukraine

ABSTRACT

The electroaluminothermic process is considered for ferrovanadium production from a vanadium-containing charge mixture by reducing vanadium oxide with aluminium in a slag layer with simultaneous electrical heating of the slag bath. The key factors influencing the fundamental parameters of the process have been identified. Samples of final slag were examined, and chemical composition and metal particle distribution in the slag layer were determined.

KEYWORDS: electroslag process, ferrovanadium, electroaluminothermic reduction, slag, chemical composition, metal, inclusions

INTRODUCTION

More than 90 % of all the vanadium mined in the world is used in the metallurgical industry for production of special steels and doping titanium alloys [1–4]. Vanadium addition to chemical composition of steel promotes an increase in wear resistance, strength and hardness of the metal [2, 5]. Vanadium binds nitrogen and reduces the steel sensitivity to aging, while simultaneously increasing its heat resistance. Vanadium microalloying became widely applied in structural steels, greatly improving their consumer qualities [6, 7]. Vanadium is also used for cast iron alloying [8]. Titanium alloys containing up to 4 % vanadium are widely applied in the aerospace industry to manufacture parts of jet engines and flying vehicle airframes [3].

World tendencies in metallurgy and related sectors are indicative of a stable growth in demand for vanadium-containing steels and alloys [4]. During steel smelting vanadium is added to the metal predominantly in the form of ferrovanadium [2, 9]. Other vanadium-containing alloys, so-caller master alloys, are used more seldom. Ferrovanadium grades with vanadium content from 35 to 85 % are available in the market [9, 10]. The majority of ferrovanadium, however, is produced and consumed in the form of FeV80 ferroalloy. On the one hand, during its manufacture the higher vanadium content in the alloy reduces the specific production costs per a product unit, making production more cost-effective. On the other hand, metallurgical enterprises, as consumers, also give preference to FeV80, so as to minimize the total quantity of the ferroalloy that needs to be spent during steel alloying.

Vanadium oxides are the main raw material for ferrovanadium production [9–11]. Vanadium reduction from its oxides may be performed with carbon, silicon and aluminium. Carbon application as a reducing agent, leads to production of an alloy with higher carbon content. Therefore, silicon and aluminium are used in industry for vanadium reduction from its oxides. However, silicathermic method does not allow producing ferrovanadium with high vanadium content and low carbon content [9, 10]. On the other hand, aluminium reduces vanadium more completely than silicon does, owing to a higher thermodynamic strength of the aluminium oxide. Therefore, low-carbon ferroalloys with more than 70 % vanadium content are produced only by aluminothermic reduction. Alloys with lower vanadium content are often produced by silicathermic method [9, 10].

The reaction of vanadium reduction with aluminium from pentoxide is highly exothermic:

$$3V_2O_5 + 10Al \rightarrow 6V + 5Al_2O_3,$$
$$\Delta G^\circ(T) = -441707 + 24.7T,\ \text{J/mol } O_2. \quad (1)$$

The heat released during this reaction, is sufficient not only for melting the iron added to produce the alloy, but also for ensuring an effective separation of the produced metal and slag, enriched in aluminium oxide [12].

All the production processes with vanadium oxide reduction with aluminium can be divided into aluminothermic (thermite) and electroaluminothermic [7, 10].

In out-of furnace aluminothermic process (thermite) the charge consists of iron scrap (or iron oxide), granules of vanadium pentoxide, aluminium and such fluxes as soda ash or fluorspar [9, 12]. Aluminium is added to the charge in the amount of 100–102 % of that required for reduction of vanadium pentoxide by the stoichiometry. Before loading into the reactor, the charge materials are thoroughly mixed in the mixing drum. The reduction process is performed in reactors lined with magnesite. The thus produced ferrovanadium usually contains 82–85 % V, up to 2 % Si, 1.5 % Mn and 0.06 % C. Under production conditions, 90–95 % of vanadium passes into the alloy from the charge. Final slag contains up to 4.5 % vanadium oxides. The main disadvantages of this process are the high reaction intensity accompanied by considerable dust and gas emissions, and significant metal consumption with remains in the slag after the reaction.

To increase vanadium extraction into the alloy, the melting scheme with additional electric heating of the slag during ferrovanadium production is used [6, 9, 10]. Additional heating of the slag promotes a more complete reduction of vanadium and improves the conditions for melting product separation, as the slag remains sufficiently liquid during the entire melting operation. The electroslag process is less active and more controlled, accordingly, than the thermite one, while vanadium extraction under certain conditions increases up to 95–97 %. The electroaluminothermic method also allows using lower vanadium oxides (V_2O_3, V_2O_4) for ferrovanadium production, where the reduction reactions are accompanied by smaller thermal effect [10].

This work is an experimental study of the electroaluminothermic process of ferrovanadium production for vanadium-containing raw materials by reducing vanadium oxide with aluminium in a slag layer, with simultaneous electric heating of the slag bath.

Experiments were conducted in a laboratory electroslag furnace of USh-114 type and in semi-industrial flux-melting furnace of A-550 type. The vanadium source in the charge was granulated commercial vanadium pentoxide of 3–5 mm fraction with the following chemical composition, wt.% 82–86 V_2O_5, 3–8 Al_2O_3, 4–7 CaO, up to 2 Fe_2O_3, 1.5 TiO_2, 0.3 SiO_2, 0.5 of other impurities. Crushed aluminium wastes with particle size of 3–5 mm were used as a reducing agent. The charge composition also included powder of 1 mm fraction. Lime and calcium fluoride were used to adjust the slag pool chemical composition. A starting point for determination of the charge composition was stoichiometric calculation in keeping with reaction (1). In order to obtain a ferroalloy with the specified vanadium content (C_V, %), it is necessary to add iron to the charge composition in the amount which can be calculated by the following formula:

$$m_{\mathrm{Fe}} = \frac{100 - C_V}{C_V} m_V = \frac{100 - C_V}{C_V} 0.56 m_{V_2O_5}, \text{ kg.}$$

Thus, in order to produce a ferroalloy with 50 % vanadium content from 10 kg of vanadium pentoxide, it is necessary to add 4.9 kg of aluminium and 5.6 kg of iron to the charge, and to produce a ferroalloy with 80 % vanadium, 1.4 kg of iron should be added. Here, the total calculated quantity of the produced alloy will be equal to 11.2 and 7.0 kg, respectively. The total amount of slag which will form from Al_2O_3 and CaO will be equal to 12.3–13.3 kg. Since commercial vanadium oxide containing impurities, is used in the charge, 0.36–0.95 kg of aluminium oxide and 0.48–0.83 kg of calcium oxide will enter the slag together with it. In addition, up to 0.24 kg Fe_2O_3 and 0.18 kg TiO_2 will enter the slag with vanadium pentoxide, which can be reduced with aluminium to the respective metals and can go into the ferroalloy. For instance, under the condition of total reduction of titanium oxide, ferrovanadium with 80 % vanadium can have up to 1.5 % titanium in its chemical composition. In view of the possible aluminium consumption for reduction of iron and titanium oxides, the amount of aluminium in the charge should be increased by 1–2 % of that required for reduction of all the vanadium oxide in the charge.

Lime and calcium fluoride are added to the charge to produce slag of the desired composition. To have liquid slag, in keeping with the equilibrium diagram of CaO–Al_2O_3 system [13], lime content in it should be equal to 48–53 % of Al_2O_3 content. A rational quantity of calcium fluoride in the charge was determined experimentally, as it is not only the slag diluent, but also a regulator of its electric resistance. During the laboratory experiments in USh-114 furnace, the slag mixture was formed on the base of flux of ANF-28 type [14], which contains 41–49 % CaF_2, 26–32 % CaO, 20–21 % SiO_2 and up to 5 % Al_2O_3. The reduction process was performed in a graphite crucible. The general scheme of organizing the melting is shown in Figure 1.

Melting was begun with a solid start with melting of part of the slag-forming materials in the crucible. After the liquid slag bath formation, the charge mixture was loaded in portions into the space between the

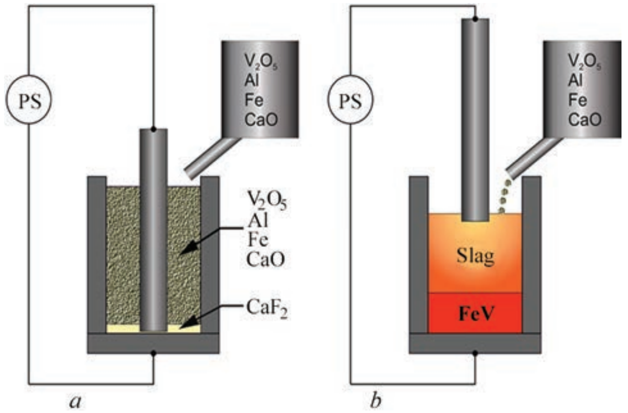

Figure 1. Schematic of realization of the process of reduction electroslag melting of ferrovanadium: *a* — process initiation; *b* — charge melting

Table 1. Composition of laboratory melt charge, g

Experiment	V_2O_5	CaF_2	ANF-28	Fe	Al	Total
10	400	20	100	50	200	770
11	200	–»–	–»–	–»–	100	470
12	500	–»–	–»–	–»–	170	840
13	–»–	70	–»–	–»–	140	860
14	510	150	–	–»–	–»–	850

Table 2. Chemical composition of the produced metal, wt.%

Experiment	V	Al	Si	Ti	Fe
10	41.38	14.7	2.51	1.63	38.48
11	24.45	7.21	1.43	N/D	62.35
12	65.15	4.17	2.66	0.64	25.45
13	61.29	7.38	4.0	0.44	23.03
14	67.0	11.0	N/D	N/D	15.0

graphite electrode and the crucible wall. Slag-forming components were added periodically, to adjust the chemical composition of the slag. The speed of the charge loading was regulated in keeping with its melting rate. After melting of the entire charge, the slag bath was kept for some time with power supply on, for completion of the reduction reactions and achievement of a more complete separation of the metal and the slag. After completion of the soaking, the power source was disconnected, and the molten products of melting were poured out of the crucible into the prepared metal mould. After their solidification and cooling, the weight of the produced metal and slag was measured on the laboratory scales and samples were taken for chemical analysis. During melting the electric mode was adjusted manually.

A series of melts were conducted under the laboratory conditions in electroslag furnace of USh-114 type, during which the features of running of the main reduction electroslag process and state of the slag bath were experimentally studied, and the conditions were determined for achievement of the best results. Tables 1, 2 give the composition of the charge and the chemical composition of the produced metal for the five final laboratory melts.

Experimental melts in a small volume allowed adjustment of the charge composition to obtain a slag bath of the required density and electric resistance, so as to ensure an appropriate running of the process of reduction and separation of the slag and the metal. However, because of the small volume of the melt and short melting duration, which was not longer than 5 min, the melting crucible did not have time to heat enough for all the produced metal to stay in the liquid state up to process completion in the entire volume of the melting zone. As a result, a certain part of the metal could not be poured out of the crucible after melting was over. Considerable specific losses of heat from the melting space, as a manifestation of the scale factor, also negatively influenced the completeness of the reduction process, which is illustrated by increased aluminium content in the produced metal (Table 2), even under the condition of its actual lack in the charge compared to the calculated value by the stoichiometry. Increase of the slag bath temperature promoted an increase of vanadium extraction into the metal (melts 12-14, Table 2).

Table 3. Composition of the charge for an experiment on electroslag melting of ferrovanadium, %

V_2O_5	Al	Fe	CaF_2	CaO	Total
55	22	5	2	16	100

Analysis of the laboratory melt data was the basis to develop a charge mixture for smelting ferrovanadium by the electroslag technology without application of ANF-28 flux. Charge composition shown in Table 3 was selected for experimental melting on a larger scale, performed in a furnace of A-550 type.

The ratio of the slag-forming components in the charge was selected so as to obtain at the start of melting a liquid slag bath, consisting of CaF_2 and CaO, and, later on, maintain CaO percentage content in the slag at the level of 48–53 %, with aluminium oxide entering the slag as a result of running of reaction (1).

During melting, the charge melted rather quickly, but without a pronounced pyroeffect. The total amount of the charge was 23.6 kg per melt. The duration of the process of charge melting was close to 16 min, and the bath was kept under current for another 4 min. After completion of the process, the melting products were poured into a steel mould (Figure 2). Here, no remains of the metal or the slag were left in the melting

Figure 2. Appearance of slag and ferroalloy in the mould

crucible. The overall weight of the melting products was 23.05 kg, of which 7.15 kg were ferrovanadium and 15.9 kg were slag (2.22 kg of slag per kilogram of metal). Evaporation losses were 0.55 kg. The quantity of the produced ferrovanadium is equal to 84.3 % of the total calculated quantity of vanadium and iron in the charge. Here, the specific power loss is equal to 1.958 kW·h/kg or 14 kW·h per one experiment.

Chemical composition of the produced alloy is given in Table 4. A too high carbon content in the metal is due to conducting the reduction process in a graphite crucible. However, application of a crucible with lining from a refractory material, not containing any carbon, will ensure production of an alloy with carbon content meeting the requirements. Extraction of the charge vanadium into the metal was equal to 72 %. Here, reduction was performed with actual lack of aluminium in the charge compared to the theoretically required one, in order to determine the degree of its utilization and absorption by the metal. Analysis of the obtained data showed that 89 % of aluminium from the charge was consumed directly for reduction of vanadium passing into ferrovanadium, and 3.9 % of aluminium from the charge entered the alloy. The rest of the aluminium was consumed in iron and titanium oxide reduction, and was lost to evaporation and oxidation. The process of metallic aluminium interaction with the slag bath obviously requires additional study. However, in any case, to increase vanadium extraction into the alloy, it is necessary to increase the aluminium fraction in the charge, taking into account the respective stoichiometric relationships.

Slag from experimental melt, entering the mould together with the metal, was studied. The thickness of the slag layer in the mould was approximately 0.05 mm (Figure 2). The slag was of gray colour and had a dense fibrous structure (Figure 3). A thin yellowish-white layer was observed on the slag surface, corresponding to slag-metal interface. Studies showed that it does not contain any vanadium oxide at all. On the other hand, the slag proper contains up to 4 % of vanadium oxide, 52–59 % aluminium oxide and 32–36 % calcium oxide. These data show that in order to improve this result, it is necessary to not only increase the aluminium fraction in the charge, but also add lime to the slag bath before soaking in such an amount, that the lime/aluminium oxide ratio was equal to 1:1 in the slag.

Figure 3. General view of a layer of slag in section (below is the slag-metal interface)

Electron microscopy studies of the slag samples revealed clusters of fine metallic inclusions along the slag-metal interface in a layer approximately 8 mm thick (Figure 4). Average size of the detected metal particles was 120–125 nm (Figure 5). By their chemical composition they are vanadium (97–98 %) with aluminium admixture (Figures 5, 6). Analysis of the slag chemical composition in this layer showed that it consists predominantly of aluminium oxide, calcium oxide and a small amount of vanadium oxide (Figure 6).

Average size of metal particles detected in the slag layer, gradually decreases from 125 nm near the metal-slag interface to 70 nm (Figure 7, *a*) in the middle of the layer and to 10 nm near the slag-atmosphere boundary (Figure 7, *b*). Here, aluminium content in its chemical composition becomes higher (Figures 6, 7). Residual vanadium content in the slag layer in the direction away from the slag-metal interface (lower layers) towards the slag-atmosphere surface (upper layers) is doubled from 1.08 to 2.15 % near the surface. In the middle layers the residual vanadium content is

Table 4. Chemical composition of the produced ferrovanadium, wt.%

V	Si	Al	C	Mn	Ti
72.68–74.27	0.6–1.17	1.67–2.93	2.08	0.08–0.11	0.3

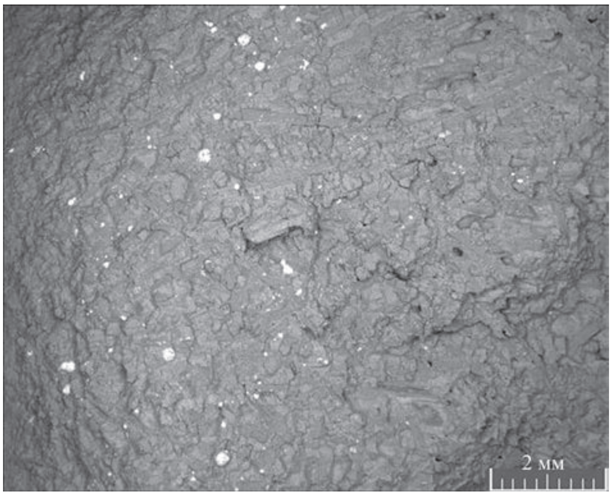

Figure 4. Clusters of metal particles in the slag layer near the slag-metal interface (surface on the right)

equal to 1.79 %. Such a picture is the result of continuation of the reduction process running in the slag layer after its penetration into the mould with simultaneous precipitation of metal drops in the liquid slag under the impact of the force of gravity. Reaction (1) is strongly exothermic, so that with temperature lowering the equilibrium in it is shifted further towards vanadium reduction. In view of that it may be rational to take measures aimed at slowing down the slag cooling in the mould during production.

It should be noted that coarse metal inclusions were not detected in the studied slag samples which is an indication of rather good separation of the melting products. All the metal particles detected in the slag layer consist of vanadium and aluminium and do not contain any iron. It can be assumed that during melting of the charge iron (in the experiment this was powder of 1 mm fraction), the forming coarse drops of molten iron are not fragmented in the slag pool and rather quickly separate from it, passing into the liquid metal pool. At the same time, vanadium reduction occurs predominantly on aluminium drops. They have smaller specific weight than the iron ones and lower precipitation rate, accordingly, and they can be entrapped by liquid slag flows. Moreover, running of a highly exothermic reaction of vanadium reduction significantly heats the reaction zone that leads to

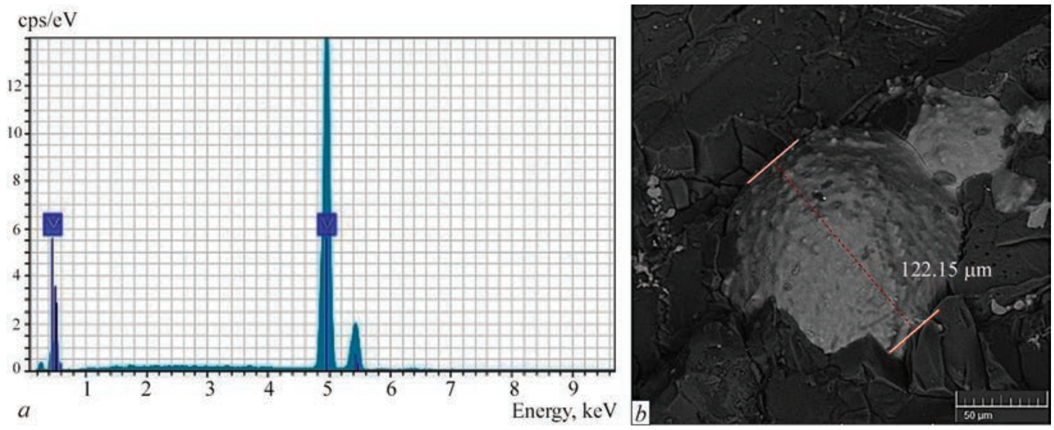

Figure 5. Size (*a*) and chemical composition (*b*) of the metallic inclusion in the slag near the slag-metal interface

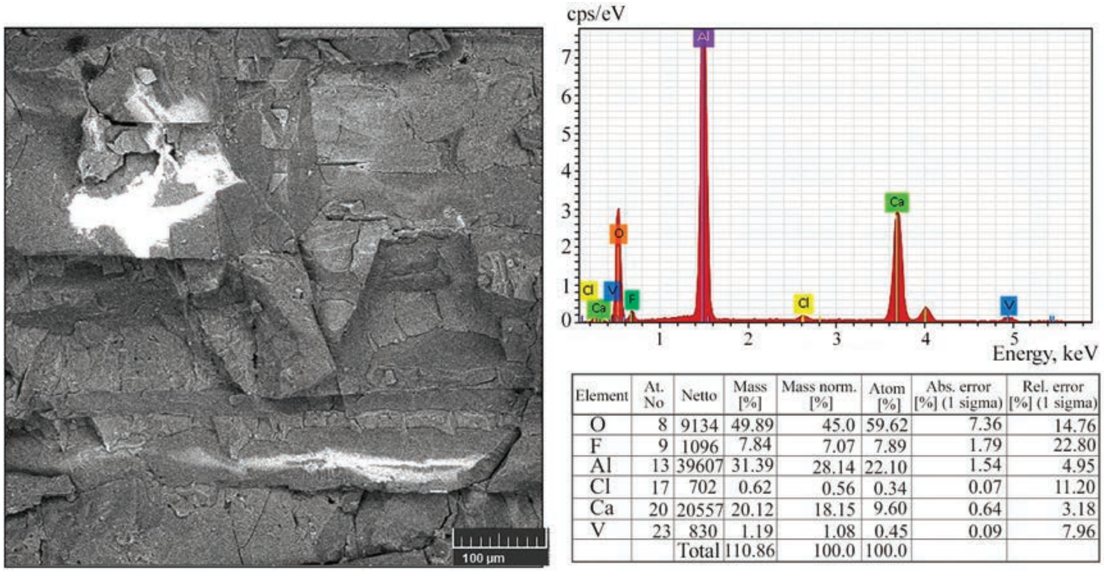

Element	At. No	Netto	Mass [%]	Mass norm. [%]	Atom [%]	Abs. error [%] (1 sigma)	Rel. error [%] (1 sigma)
O	8	9134	49.89	45.0	59.62	7.36	14.76
F	9	1096	7.84	7.07	7.89	1.79	22.80
Al	13	39607	31.39	28.14	22.10	1.54	4.95
Cl	17	702	0.62	0.56	0.34	0.07	11.20
Ca	20	20557	20.12	18.15	9.60	0.64	3.18
V	23	830	1.19	1.08	0.45	0.09	7.96
		Total	110.86	100.0	100.0		

Figure 6. Composition of slag in the layer saturated with metal inclusions near the slag-metal interface

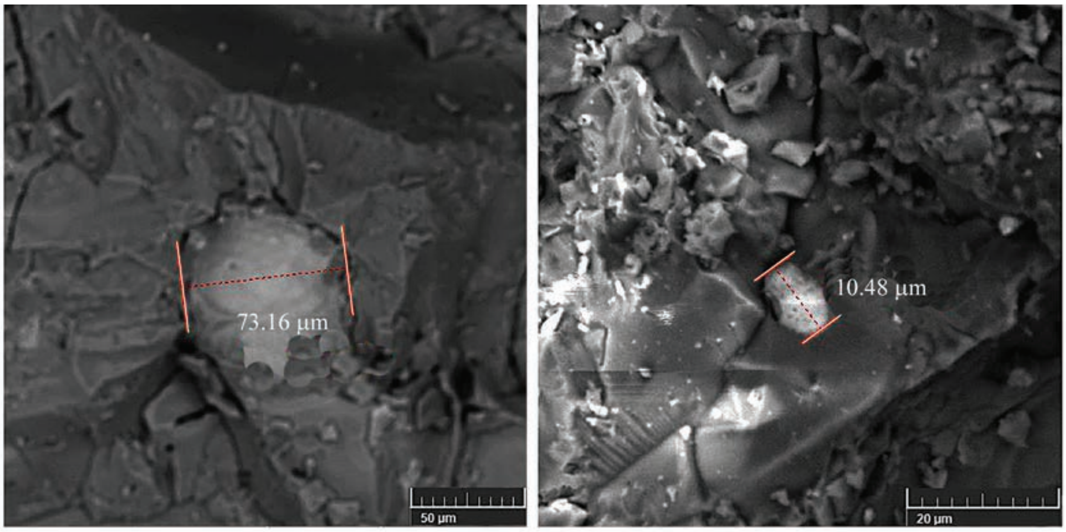

Element	At. No	Netto	Mass [%]	Mass norm. [%]	Atom [%]	Abs. error [%] (1 sigma)	Rel. error [%] (1 sigma)
O	8	1290	3.80	4.42	11.99	1.29	33.87
Al	13	6559	7.39	8.61	13.84	0.41	5.56
Ca	20	700	0.67	0.78	0.84	0.07	10.92
V	23	53282	73.32	85.83	72.73	2.05	2.79
Fe	26	294	0.66	0.77	0.59	0.10	15.24
		Total	85.83	100.0	100.0		

a

Element	At. No	Netto	Mass [%]	Mass norm. [%]	Atom [%]	Abs. error [%] (1 sigma)	Rel. error [%] (1 sigma)
F	9	375	6.87	7.46	16.40	2.19	31.86
Al	13	2545	4.31	4.69	7.25	0.28	5.39
S	16	6656	7.39	8.02	10.45	0.32	4.36
Ca	20	1434	2.02	2.20	2.29	0.12	5.16
V	23	34128	71.47	77.53	63.61	2.02	2.82
		Total	92.07	100.0	100.0		

b

Figure 7. Size and chemical composition of metal particles in the middle of the slag layer (*a*) and near the slag-atmosphere boundary (*b*)

reduction of the surface tension value of the present substances, dilution of the liquid phases and this way it promotes dispersion of the metal phase in the slag as a result of drop deformation under the impact of dynamic pressures of the environment, which are greater than the interphase tension forces [15]. Thus, the movement, coalescence and dispersion of the metal drops of different composition in the slag layer have a significant role in separation of the melting products and alloy formation.

CONCLUSIONS

1. The process of producing ferrovanadium by electroaluminothermic method, during which vanadium is reduced from its oxide with aluminium in a slag layer in the electroslag furnace, is less active and, therefore, more controlled than the aluminothemic (thermite) process. At such organization of the reduction process it is easier to control the slag viscosity, separation of the melting products, dissolution of the refractory lining and achievement of high product quality. Owing to the possibility of flexible adjustment of the charge composition, it is possible to produce ferroalloys with vanadium content from 40 up to 80 %, depending on the demand. Another important advantage of the electroaluminothermic process is simplified requirements to raw material preparation.

2. During the experiment on testing the developed procedure of producing ferrovanadium performed in electroslag melting furnace of A-550 type under the conditions close to the industrial ones, 7.15 kg of ferrovanadium with vanadium content of 73–74 % and 15.9 kg of slag with up to 4 % residual vanadium oxide content were produced from the charge of 23.6 kg weight. Here, vanadium extraction into the metal phase was equal to 72 %, and power consumption was 1.958 kW·h/kg.

3. Metal inclusions detected in the final slag, are of the size of 10–125 nm and by their chemical composition they consist of vanadium with a small aluminium addition. Their distribution by size and chemical composition in the slag layer shows that vanadium reduction and melting product segregation go on also in the mould during slag cooling.

4. Work on further improvement of the tested technology and its adaptation to the conditions of the specific production require solving the tasks on increasing the degree of vanadium extraction into the alloy and optimization of the specific power losses.

REFERENCES

1. Moskalyk, R.R., Alfantazi, A.M. (2003) Processing of vanadium: A review. *Minerals Engineering*, 16(**9**), 793–805. DOI: https://doi.org/10.1016/S0892-6875(03)00213-9
2. Yang, B., He, J., Zhang, G. et al. (2021) Chapter 11 — Applications of vanadium in the steel industry. *Vanadium*. Elsevier, 267–332. DOI: https://doi.org/https://doi.org/10.1016/B978-0-12-818898-9.00011-5
3. Simandl, G.J. (2022) Vanadium as a critical material: Economic geology with emphasis on market and the main deposit types. *Applied Earth Sci.*, 131(**4**), 218–236. DOI: https://doi.org/10.1080/25726838.2022.2102883
4. Swinbourne, D.R., Richardson, T., Cabalteja, F. (2016) Understanding ferrovanadium smelting through computational thermodynamics modelling. *Mineral Processing and Ex-*

tractive Metallurgy, 125(**1**), 45–55. DOI: https://doi.org/10.1179/1743285515Y.0000000019

5. Liu, Z., He, B., Lyu, T., Zou, Y. (2021) A review on additive manufacturing of titanium alloys for aerospace applications: Directed energy deposition and beyond Ti–6Al–4V. *JOM*, 73(**6**), 1804–1818. DOI: https://doi.org/10.1007/S11837-021-04670-6
6. Villalobos, J.C., Del-Pozo, A., Campillo, B. et al. (2018) Microalloyed steels through history until 2018: Review of chemical composition, processing and hydrogen service. *Metals*, 8(**5**), 351. DOI: https://doi.org/10.3390/met8050351
7. Baker, T.N. (2016) Microalloyed steels. *Ironmaking & Steelmaking*, 43(**4**), 264–307. DOI: https://doi.org/10.1179/1743281215Y.0000000063
8. Kim, S., Baek, E., Jang, B. (2021) The effect of vanadium addition on the fracture and wear resistance of indefinite chilled cast iron. *Materials Today Communications*, 26(**3**), 101819. DOI: https://doi.org/10.1016/j.mtcomm.2020.101819
9. Gasik, M. (2013) Technology of vanadium ferroalloys. *Handbook of Ferroalloys*. Elsevier, 397–409. DOI: https://doi.org/10.1016/C2011-0-04204-7
10. Yang, B., He, J., Zhang, G., Guo, J.B. (2021) Chapter 10 — Ferrovanadium. *Vanadium*. Elsevier, 243–266. DOI: https://doi.org/10.1016/B978-0-12-818898-9.00010-3
11. Gasik, M., Dashevskii, V., Bizhanov, A. (2021) *Ferroalloys: Theory and practice*. Springer. DOI: https://doi.org/10.1007/978-3-030-57502-1
12. Lyakishev N.P., Pliner Yu.L. (1978) *Aluminothermy*. Moscow, Metallurgiya [in Russian].
13. Hallstedl, B. (1990) Assessment of the CaO–Al_2O_3 system. *J. of the American Ceramic Society,* 73(**1**), 15–23. DOI: https://doi.org/10.1111/j.1151-2916.1990.tb05083.x
14. GOST 30756–2001: *Fluxes for electroslag technologies. General specifications.* Minsk, Interstate Council for Standardization, Metrology and Certification.
15. Nekrasov, O.P., Veretenchenko, B.A. (2018) *Surface phenomena and disperse systems*. Kharkiv, NTU KhPI.

ORCID

Yu.V. Kostetsky: 0000-0003-0742-0684,
E.O. Pedchenko: 0000-0002-8824-4389,
M.O. Vdovin: 0009-0007-4848-4154,
G.O. Polishko: 0000-0001-7543-280X,
V.L. Petrenko: 0000-0003-2440-1901,
V.A. Zaytsev: 0000-0003-2498-8191

CONFLICT OF INTEREST

The Authors declare no conflict of interest

CORRESPONDING AUTHOR

Yu.V. Kostetskyi
E.O. Paton Electric Welding Institute of the NASU
11 Kazymyr Malevych Str., 03150, Kyiv, Ukraine.
E-mail: y.kostetsky@paton.kiev.ua

SUGGESTED CITATION

Yu.V. Kostetskyi, E.O. Pedchenko, M.O. Vdovin, G.O. Polishko, V.L. Petrenko, V.A. Zaytsev (2025) Production of ferrovanadium under the conditions of electroslag melting. *The Paton Welding J.*, **1**, 28–34.
DOI: https://doi.org/10.37434/tpwj2025.01.05

JOURNAL HOME PAGE

https://patonpublishinghouse.com/eng/journals/tpwj

Received: 15.08.2024
Received in revised form: 30.09.2024
Accepted: 28.01.2025

DOI: https://doi.org/10.37434/tpwj2025.01.06

MATHEMATICAL MODELLING OF THE PROCESSES OF COMPONENT DIFFUSION IN THE CORE–GRAPHITE ELECTRODE SYSTEM IN AN INDUSTRIAL ARC STEELMAKING DC FURNACE OF THE DSP PS-12 TYPE

O.V. Makhnenko, O.S. Kostenevich, G.Yu. Saprykina, O.G. Bogachenko, I.O. Goncharov, I.O. Neilo

E.O. Paton Electric Welding Institute of the NASU
11 Kazymyr Malevych Str., 03150, Kyiv, Ukraine

ABSTRACT

The work shows the possibility of using the method of mathematical modelling to predict the distribution of chemical components in the core-electrode system during operation in an arc steelmaking furnace, taking the diffusion processes into account. The diffusion coefficients for each component were determined on the basis of the developed two-dimensional finite element model of the process of component diffusion in this system, and taking into account the experimental data on the residual distribution of the component content in the cross-section of the cored electrode. These coefficients were used to conduct modelling of the diffusion process in order to assess the possible distribution of the component content in the cored electrodes of an increased diameter and to demonstrate the modelling results, taking into account different initial concentrations.

KEYWORDS: arc steelmaking furnaces, graphite cored electrodes, specific electrical resistance, components, concentration, diffusion, mathematical modelling

INTRODUCTION

The composition of graphite electrode cores can vary widely depending on the type of furnace, the type and quality of the charge, steel grade, electrical conditions, etc. [1, 2]. The core in the initial state consists of a mixture of graphite with impurities of components containing Li, Na, K, etc.

Optimisation of the initial chemical composition of the core for electrodes of different type size (diameter) and purpose can be performed by numerical experiments (mathematical modelling) of the process of mutual diffusion of chemical elements (components) in the core-electrode system at high temperatures in a furnace, taking into account the known data on the diffusion coefficients of these elements in graphite. However, such data, taking into account high temperatures in a furnace (1800–2300 °C) and the near-arc region of the electrode itself of up to 4000 °C, is almost not publicly available. For example, the works [3–5] present experimental data on the diffusion coefficients of some elements (Li, Na, K) in graphite, but at low temperatures (25 and 960 °C) [6]. Therefore, one of the ways to solve these issues is to determine or approximately evaluate the values of diffusion coefficients of the core components as a result of processing the existing experimental data according to the residual content of these components in the core-electrode system.

This work presents the results of the first attempt of mathematical modelling of the diffusion processes of the core components for an electrode with an initial diameter of 350 mm and electrodes of an increased diameter of 508 and 600 mm of two compositions (symbolic designation F_0 and F_0').

A general view of an industrial cored electrode with an outer diameter of 350 mm used in a 12-t industrial DC furnace of the DSP PS-12 type is shown in Figure 1. In the work, the samples were used in the study taken from the lower (near-arc) region of the electrode after its 18 h operation in the furnace and a further cooling to room temperature. The samples were taken at a distance of 35 mm from the core axis and 80 and 105 mm from the core-electrode interface to determine the actual distribution of the core components in the body of this electrode (Figure 2).

PROCEDURE FOR THE DETERMINATION OF DIFFUSION COEFFICIENTS OF COMPONENTS IN THE CORE-ELECTRODE SYSTEM

The distribution of the diffusion component content in the cross-section of the cored electrode can be determined by solving the diffusion equation in a two-dimensional formulation:

$$\frac{dc}{dt} = D_C\left(\frac{d^2c}{dx^2} + \frac{d^2c}{dy^2}\right), \tag{1}$$

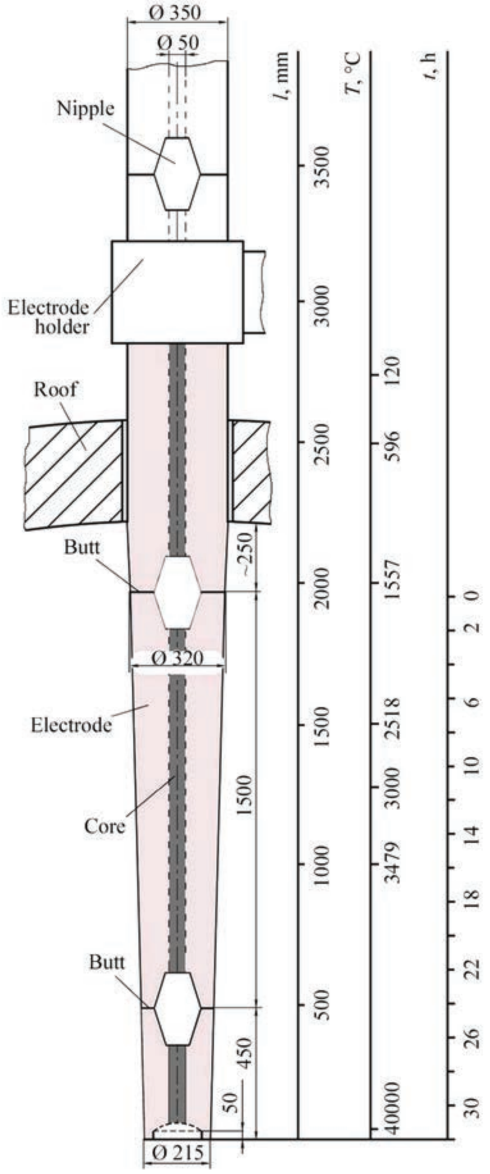

Figure 1. Temperature distribution and changes of geometric parameters in real time of the furnace operation for the cored electrode with an initial diameter of 350 mm

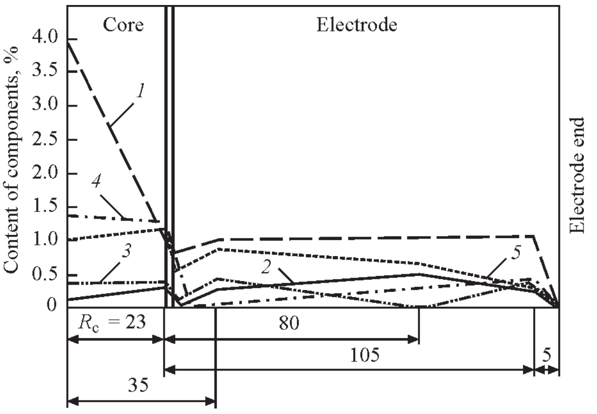

Figure 2. Distribution of the component content in the cross-section of the core and electrode with an outer diameter of 350 mm; *1* — Cu; *2* — K; *3* — Cr; *4* —Ba; *5* —Ti

Table 1. Initial content of components in the core (composition of F_0) for the calculation of diffusion coefficients, wt.%

Time, h	Cu	K	Cr	Ba	Ti
0	15.6	2.0	2.75	2.1	9.4
3	Data in Figure 2				

where c is the concentration of the diffusion components; D_C is the diffusion coefficient of the diffusion components; t is the time; x, y are the coordinates.

The initial boundary conditions:

$$c(t = 0) = c_0 \text{ — in the core at}$$

$$0 < r = \sqrt{x^2 + y^2} < D_c;$$

$$c(t = 0) = 0 \text{ — in the electrode at}$$

$$D_c < r = \sqrt{x^2 + y^2} < D_{el}. \tag{2}$$

The initial data for modelling were the actual data on the content of components in the core in the initial state (Table 1) and in the core and electrode after operation of the cored electrode with an initial diameter of 350 mm in the furnace (Figure 2). After use in the furnace, the diameter of the electrode decreased as a result of oxidation to 215 mm (Figure 1).

A two-dimensional finite element model of diffusion in the cross-section of the cored electrode was developed (Figure 3). In the core ($r < R_c = 23$ mm), the initial concentration (content) of each component was set (Table 1), in the rest of the electrode (23 mm $< r <$ 105 mm), the initial concentration was set to zero.

Due to the lack of data on the values of diffusion coefficients of the considered components in graphite at high temperatures, it was assumed that the diffusion coefficients on the electrode temperature in the temperature range of 30–4000 °C could be determined as averaged. The time of electrode operation was set to 3 h, based on the fact that after some time from the start of the electrode operation in the furnace, as a result of diffusion, the content of the core and electrode components corresponds to that shown in Figure 2. As a result of the carried out numerical experiments, the diffusion coefficients for each component were determined under the condition of maximum coincidence with the experimental data on the distribution of the component content by the electrode radius at the end of its operation. The iterative selection of diffusion coefficients was performed at the smallest square deviations [6]:

$$\sum_{i=1}^{n} (f_i - f_x)^2 \to \min, \tag{3}$$

where $(f_i - f_x)^2$ is the square deviation between the actual value f_i and the corresponding estimated f_x; n is the number of pairs of compared values.

The additional verification and correction of the experimental data on the distribution of the component content in the electrode was carried out. The total amount of the components (gain of content per volume) in the electrode after 3 h of operation should not exceed the initial amount in the core and remain approximately the same (excluding burnout losses and diffusion into the environment). The amount of the components before and after operation in the furnace can be estimated by the initial content of the components in the core and the residual total content in the core and electrode.

RESULTS OF THE DETERMINATION OF DIFFUSION COEFFICIENTS OF THE CORE COMPONENTS

Using the presented procedure, the diffusion coefficients for each component contained in the core were iteratively selected. Figure 4 shows the results of correcting the experimental data on the distribution of the content of the Ti component after operation in the furnace, provided that the amount of the component before and after the operation of the cored electrode in the furnace is maintained, as well as several calculated distributions of the content of the Ti component after the furnace operation for different iterations to determine the diffusion coefficient, indicating the standard deviation from the corrected experimental data. As a result of the iterative selection, the diffusion coefficient for the Ti component is 540 mm^2/h (mean-square deviation is 0.024).

Figure 5, *a* shows the predicted calculated component distributions in the cross-section of the cored electrode with an initial diameter of 350 mm after use in the furnace, the diameter of which was reduced as a result of burning to 215 mm in accordance with the determined diffusion coefficients. It can be seen that the distributions of all components are quite uniform with a slight increase towards the centre of the electrode.

Based on the determined calculated values of the diffusion coefficients of the components and their different initial concentrations in the core, the diffusion process was modelled to predict the possible distribution of their content in the cored electrodes of an increased diameter (508 and 600 mm) after 3 h of operation in the furnace. The modelling results (Figure 5, *b*, *c*) showed that the initial component concentration in the core of the electrodes of an increased diameter, as in the electrode with a diameter of 350 mm, did not ensure the distribution of a uniform content of these components over the entire cross-section of graphite electrodes. In the cross-section of the electrode, closer to its outer surface, the content of the components

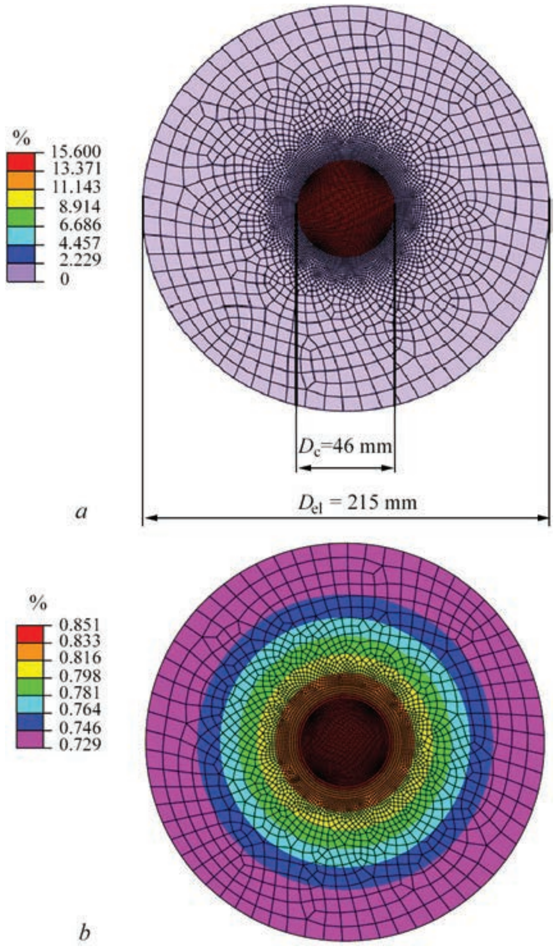

Figure 3. Two-dimensional finite element model of diffusion in the cross-section of the cored electrode: *a* — concentration of the Cu component in the initial state; *b* — after 3 h of electrode operation

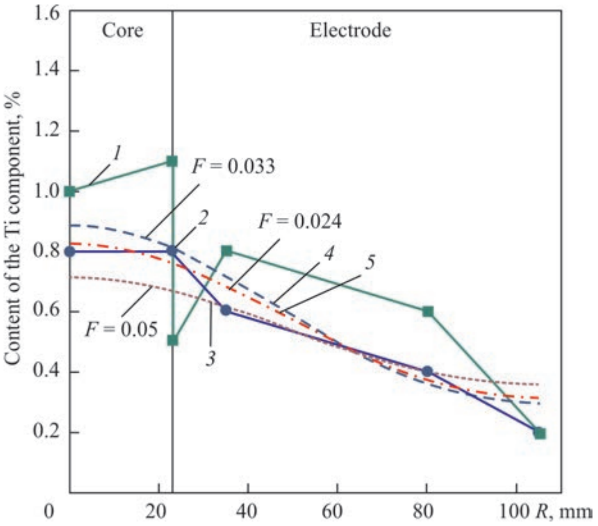

Figure 4. Experimental and calculated distributions of the content of the Ti component depending on the radial coordinate of the electrode with an initial diameter of 350 mm after 3 h of the furnace operation: *1*, *2* — initial and corrected experimental data; *3* — calculated data at D = 650 mm^2/h; *4*, *5* — at D = 500 and 540 mm^2/h

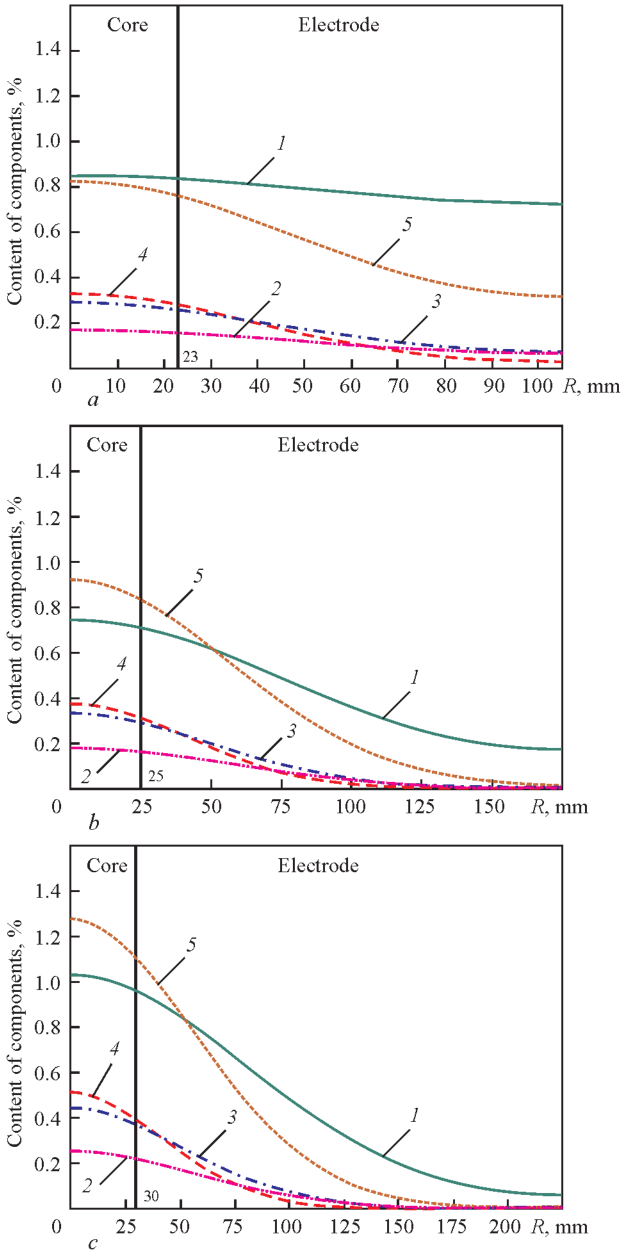

Figure 5. Estimated distributions of the content of core components depending on the radial coordinate of electrodes with initial diameters of 350 mm (*a*), 508 mm (*b*), 600 mm (*c*) after 3 h of the furnace operation and components and corresponding values of diffusion coefficients *D*, mm^2/h: *1* — (Cu) 1170; *2* — (K) 620; *3* — (Cr) 460; *4* — (Ba) 290; *5* — (Ti) 540

(except for the Cu component) after 3 h of operation remains almost zero, which is a negative factor for ensuring the effective operation of the electrode.

Table 2. Limit parameters of an increased initial content of components of F_0' in the core of electrodes with the diameters of 508 and 600 mm, wt.%

Time, h	Cu	K	Cr	Ba	Ti
0	15.6	4.0	5.5	6.6	9.4
Note. The initial content of components in the electrode is equal to zero.					

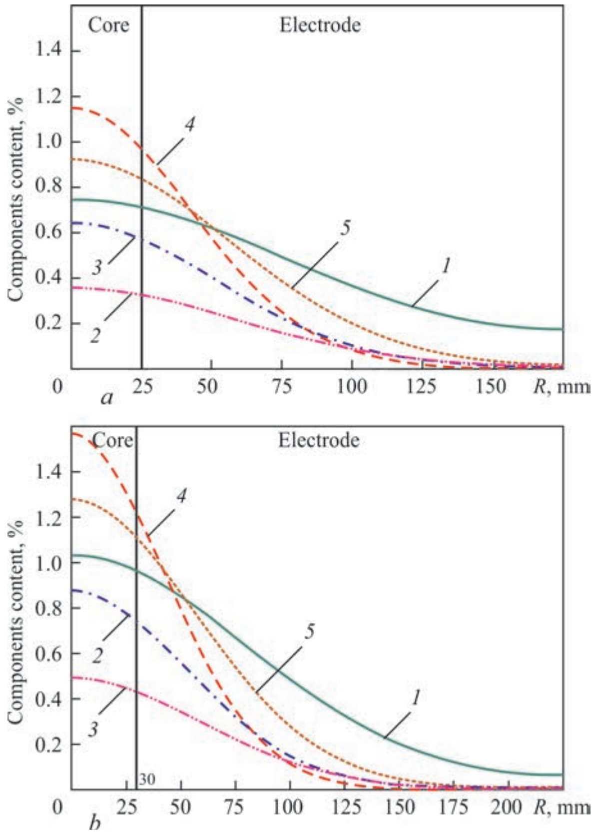

Figure 6. Distribution of the component content in the radial direction of the electrode with a diameter of 508 (*a*) and 600 mm (*b*) after 3 h of operation and components and corresponding values of diffusion coefficients *D*, mm^2/h: *1* — (Cu) 1170; *2* — (K) 620; *3* — (Cr) 460: *4* — (Ba) 290; *5* — (Ti) 540 with an increase in the initial content of individual components in the core

Taking into account that as a result of modelling, a rather low component content was obtained in the electrodes of increased diameters (508 and 600 mm) after 3 h of operation in the furnace, it was decided to increase the initial concentration (content) of individual components in the core F_0' for these electrode diameters (Table 2).

Based on the obtained calculated values of the diffusion coefficients of the components and increased initial concentrations of the individual components (K, Cr, Ba) in the core, the diffusion processes were modelled in the core to evaluate the possible distribution of the component content in the cored electrode with a diameter of 508 and 600 mm after 3 h of operation in the furnace (Figure 6, *a*, *b*). The modelling results showed that even a significant increase in the initial component content in the core by 2–3 times did not ensure a uniform distribution of these components in the cross-section of a graphite electrode of an increased diameter after 3 h of operation. On the periphery, closer to the outer surface of the electrode, the content of components remained very low. Only copper, due to the highest value of the diffusion coefficient, has a non-zero content distribution over the entire cross-section of the electrode.

CONCLUSIONS

1. For the first time, it was shown that mathematical modelling can be used to predict the distribution of components in the core-electrode system during operation in an arc furnace, taking into account the diffusion processes.

2. Due to the lack of data on the values of the considered components of the diffusion coefficients in graphite at high temperatures, it was assumed that the diffusion coefficients can be determined as averaged from the electrode temperature in the temperature range of 30–4000 °C. The time of electrode operation was set to three hours.

3. Based on the developed two-dimensional finite element model of the process of the component diffusion in the core-electrode system in the cross-section of the cored electrode and experimental data on the distribution of the content of components (Cu, K, Cr, Ba, Ti) in the initial state and after three hours of operation of the cored electrode with an initial diameter of 350 mm, in the course of numerical experiments, diffusion coefficients for each component were iteratively determined, provided that the maximum coincidence with the least square deviations with the experimental data at the end of the electrode operation in a DC arc furnace.

4. Based on the determined calculated values of the diffusion coefficients of the components and their different initial concentrations in the core, the diffusion process was modelled to predict the possible distribution of their content in the cored electrodes of an increased diameter (508 and 600 mm) after three hours of operation in the furnace. The modelling results showed that even a significant increase in the initial component content in the core by 2–3 times did not ensure a uniform distribution of the content of these components in the cross-section of graphite electrodes of an increased diameter, and at the periphery, closer to the outer surface of the electrode, the content of components after 3 h of operation is close to zero. Only copper, due to its rather high content in the core and a high diffusion coefficient, has a non-zero distribution of the content across the electrode cross-section.

5. To consider it necessary to continue the works on mathematical modelling of diffusion processes in the core-electrode system in relation to arc steelmaking furnaces.

REFERENCES

1. Bogachenko, A.G., Mishchenko, D.D., Braginets, V.I. et al. (2016) Saving electricity on arc DC steelmaking furnaces with graphitized wick electrodes. *Sovrem. Elektrometall.,* **1**, 58–64. DOI: ttps://doi.org/10.15407/sem2016.01.09
2. Paton, B. E., Bogachenko, O. G., Kyiko, S. G. et al. (2021) Experience of application of graphitized wick electrodes in an industrial arc steel-making furnace. *Suchasna Elektrometal.,* **1**, 48–53. DOI: https://doi.org/10.37434/sem2021.01.06
3. Hua-jun Guo, Xin-hai Li, Xin-ming Zhang et al. (2007) Diffusion coefficient of lithium in artificial graphite, mesocarbon microbeads, and disordered carbon. *New Carbon Materials*, **1**, 7–11. DOI: https://doi.org/10.1016/S1872-5805(07)60006-7
4. Persson, K., Sethuraman, V. A., Hardwick, L.J. et al. (2010) Lithium diffusion in graphitic carbon. *J. Phys. Chem. Lett.*, 1(**8**), 1176–1180. DOI: https://doi.org/10.1021/jz100188d
5. Wang, Z., Ratvik, A. P., Grande, T., Selbach, S.M. (2015) Diffusion of alkali metals in the first stage graphite intercalation compounds by vdW-DFT calculations. *The Royal Society of Chemistry Advances*, **5**, 15985–15992. DOI: https://doi.org/10.1039/c4ra15529g
6. Dedenko, L. G., Kerzhentsev, V. V. (1977) *Mathematical processing and presentation of experimental results*. Moscow, Moscow State University Publ. House [in Russian].

ORCID

O.V. Makhnenko: 0000-0002-8583-0163,
O.S. Kostenevich: 0000-0002-7427-2805,
G.Yu. Saprykina: 0000-0003-1534-7253,
O.G. Bogachenko: 0000-0002-3306-6626

CONFLICT OF INTEREST

The Authors declare no conflict of interest

CORRESPONDING AUTHOR

O.V. Makhnenko
E.O. Paton Electric Welding Institute of the NASU
11 Kazymyr Malevych Str., 03150, Kyiv, Ukraine.
E-mail: makhnenko@paton.kiev.ua

SUGGESTED CITATION

O.V. Makhnenko, O.S. Kostenevich,
G.Yu. Saprykina, O.G. Bogachenko, I.O. Goncharov,
I.O. Neilo (2025) Mathematical modelling of the processes of component diffusion in the core–graphite electrode system in an industrial arc steelmaking DC furnace of the DSP PS-12 type.
The Paton Welding J., **1**, 35–39.
DOI: https://doi.org/10.37434/tpwj2025.01.06

JOURNAL HOME PAGE

https://patonpublishinghouse.com/eng/journals/tpwj

Received: 15.08.2024
Received in revised form: 30.09.2024
Accepted: 23.01.2025

DOI: https://doi.org/10.37434/tpwj2025.01.07

MODIFICATION AND MICROALLOYING OF THE METAL OF WELDS ON HSLA STEELS PRODUCED BY FUSION WELDING METHOD (REVIEW)

M.P. Reminnyi[1], **V.A. Kostin**[2], **V.V. Zhukov**[2]

[1]Kyiv Academic University
36 Acad. Vernadskyi Blvd, 03142, Kyiv, Ukraine
[2]E.O. Paton Electric Welding Institute of the NASU
11 Kazymyr Malevych Str., 03150, Kyiv, Ukraine

ABSTRACT

The paper considers various aspects of the modification and microalloying of weld metal of high-strength low-alloy (HSLA) steels with dispersed particles of various compounds. The essence and relationship of the processes is highlighted in the context of improving the mechanical properties of the weld metal. The methods and technologies of modification of the structure of HSLA steels and their welded joints were analyzed. The use of various technologies and methods of introducing modifiers into the liquid weld pool is considered, with determination of their effectiveness and impact on the quality of the final product. The influence of different types of modifiers on structure formation, features of the kinetics of phase transformations, structural and chemical liquation and mechanical properties of the resulting welded joints have been analyzed. Particular attention is paid to the aspects of nanomodification of weld metal, determining its advantages and disadvantages.

KEYWORDS: high-strength low-alloy steels, modification, microalloying, microstructure, mechanical properties, automatic welding, weld metal, liquation, nanoparticles

INTRODUCTION

Welding in modern industry is an indispensable part of production processes, which creates an integral element of construction and manufacture. The ability to produce joints ensuring the strength and ductility, makes welding a critical stage of the production cycle. However, with advance of technology and expansion of quality requirements, the need to improve the techniques and materials used in the welding process becomes greater.

In particular, welding of high-strength low-alloy (HSLA) steels with a low content of alloying elements, faces the challenge of ensuring not only strength, but also toughness of the weld metal structure.

Controlling the formation of primary microstructure of the weld metal is given a lot of attention in literature. Grain refinement [1], solid solution alloying and microalloying [2], as well as formation of nonmetallic inclusions of a certain size, composition and morphology (also by addition of dispersed high-melting particles into the weld pool) [3] are the main factors, allowing providing of weld metal strength and toughness. Among these methods, application of weld metal modification by second phase particles is becoming and integral part for achieving optimal results.

“Microalloying” term should be understood as a method to influence the structure and properties of the metal (alloy) only by adding small quantities (≤0.1 %) of elements or their compounds to its composition, which have a considerable impact on the processes running in the solid phase.

“Modification” term should be understood as a set of any chemical, physical or complex processes, influencing the end structure and properties of the metal (alloy). This is a process of active regulation of primary crystallization and/or changing the degree of dispersity of the crystallizing phases. Metal modification can be conducted by adding modifiers to the melt, or by active influence of various physical (mechanical) methods on the melt.

“Nanomodification” term should be understood to mean adding nanoparticles or nanomaterials of less than 100 nm size to the liquid weld pool with the purpose of influencing the formation of weld metal microstructure to improve its properties.

Dispersion strengthening, where second phase particles are used, as a mechanism of grain growth prevention, similar to the mechanism of refinement of microstructural components, is particularly important for weldable steels. Refinement of the structure of the majority of steels and alloys has a favourable impact on the entire complex of their mechanical properties [4].

There is a large number of materials and methods for realization of modification in modern technological processes. One of them is addition of high-melting exogenic inclusions into the liquid melt (inoculation). Two main mechanisms of the influence of exogenic inclusions on melt crystallization are usually considered [5]. In keeping with the first one, the particles are independent crystallization centers, performing “direct” heterogeneous nucleation, or form such centers as a result of interaction with the melt. By the second mechanism, the particles block the growth of crystallites or structural elements, which form during cooling.

Modification results in refinement of the grains or structural components. In a number of cases, direct combination of both the processes is possible, which leads to transformation of the phases with an acicular or lamellar structure into a more equilibrium globular one that increases the metal strength, ductility and toughness, preventing internal stress concentration and cracking.

Over the recent years, application of specially prepared nanopowder inoculators or modifiers to increase the cast metal quality is attracting a lot of interest. These are nanopowders with particle sizes of <100 nm from refractory compounds (oxides, nitrides, carbides, borides, etc.) [6, 7]. At addition to the melt, they are distributed over the liquid metal volume, and serve effective crystallization centers.

Wide prospects of dispersed powder application for modifying influence on the melt in metallurgy allow looking in a new way at the possibilities of controlling the process of liquid pool crystallization in arc processes of fusion welding [8, 9].

Modification is widely used in production of materials for construction, transportation, mechanical engineering and other industries, as a result of improvement of the strength, ductility and impact toughness of metal products operating under high loads and extreme service conditions [4].

Alongside the indubitable advantages of application of the modification method, however, use of modifying for welded joints may face certain challenges and potentially negative consequences. This is, primarily, formation of macro- and microdefects, cavities, pores, cracks and other defects, appearance of regions of chemical heterogeneity and liquation in the weld. Secondly, the particles can completely dissolve in the liquid pool without any modifying effect that necessitates application of additional specific requirements to control of temperatures and technical parameters of welding. Thirdly, nonuniform distribution of particles in the weld metal will lead to heterogeneity in the microstructure, and, consequently, to lowering of the mechanical properties in individual regions of the weld.

The objective of this work is analysis of literature data on modification and microalloying of the metal of welds, influence of modifying particles of different compounds on the structure and mechanical properties, as well as of the prospects for nanoparticle application for welding high-strength low-alloy steels.

MODIFICATION AND MICROALLOYING OF THE WELD METAL

Addition of powderlike material into the weld pool (Figure 1) may lead to different consequences, namely primary modifier particles remain in the weld metal (modification); the particles may dissolve completely, changing the solid solution composition (microalloying) [10]; new particles precipitate in the form of dispersed nonmetallic inclusions (dispersion hardening); the particles coagulate and/or stick to each other, forming complex phase precipitates (coagulation); particles change the morphology and composition of nonmetallic inclusions already existent in the metal.

Changes of chemical composition of weld metal and particles can also influence the kinetics of transformation in the solid state, transformation temperature and the forming microstructure. Influence of modifiers at liquid metal crystallization may influence the primary dendritic structure of the weld metal, the width and type of the weld dendritic structure [11]. The microstructure will be influenced by the composition, distribution and size of modifying and secondary particles [12].

As a result of the dispersed particles interacting with the liquid metal, when they are used for modification, their complete or partial dissolution is possible, leading to metal microalloying in individual regions of the weld. Therefore, at modification by fine particles this process cannot be considered without regard to microalloying.

It is widely known that the microcontent of chemical elements or their compounds in the metal or the welded joint can have an essential influence on the nature of metal crystallization, shape and composition of nonmetallic inclusions, structure of grain boundaries and near-boundary zones, weldability, hardening, heat- and wear resistance, etc., i.e. on a whole set of technological and service properties [13].

One of the effective methods to control the liquid metal composition during electric arc welding is

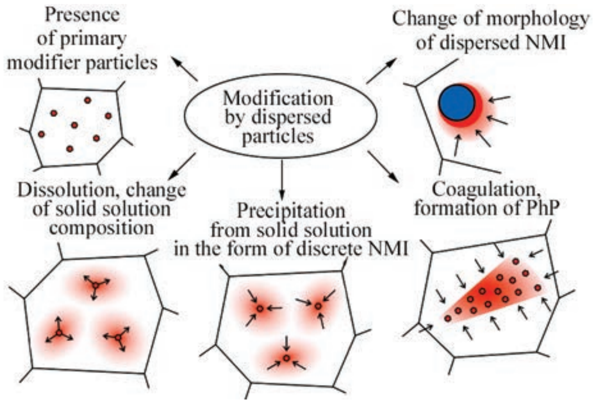

Figure 1. Modification influence on the nature of transformations of dispersed particles [31]

its modification and microalloying through welding consumables which is effective in terms of cost and technology. Literature sources quite widely cover the problem of microalloying of steels and their welded joints [14].

Although the content of individual elements at microalloying is not higher than 0.1 wt.%, they have a considerable effect on the processes running in the solid phase (structural-phase transformations, phase composition, size of the primary austenitic grain, structure and cleanliness of the boundaries and near-boundary zones, etc.) [15].

So, microalloying with chromium increases the hardness, strength, toughness, wear resistance, improves the corrosion resistance, as well as ductility, but decreases the heat conductivity. Vanadium improves the hardness, strength, toughness, resistance to dynamic stresses and wear, reduces temper brittleness, refines the structure and improves the resistance to overheating at quenching. Molybdenum increases the hardness, strength, hardenability, treatability by cutting, heat resistance; promotes formation of a fine-grained structure, improves the weldability and mechanical properties of the welded joints. Titanium microadditive improves the hardness, strength, and wear resistance, but lowers the hardenability. Titanium is used in the form of its compounds with carbon, nitrogen and boron. Titanium carbonitrides Ti(C, N) are the most often used as modifiers, leading to grain refinement. Application of WC tungsten carbide in the metal of low-alloy steel leads to formation of a more homogeneous microstructure, increasing the ductile characteristics [16]. Boron microadditives are used to improve the set of mechanical properties of steels, subjected to hardening with tempering. Here, boron influence is associated with increase of hardenability and refinement of austenitic grain. In some cases not free boron, which is difficult to add to the liquid metal, but its compounds TiB_2, LaB_6, CaB_6, etc. are used.

Recently, such nanomaterials, as nanoparticles of carbon [17, 18], graphene [19] or fine oxides of refractory metals [20] also began to be used for modification.

Modification of welded joint metal allows effective use of the modes of postweld heat treatment to produce the desired structural components and mechanical properties.

In the general case it can be noted, that application of microalloying and modification leads to grain refinement and to producing a more homogeneous structure that has a positive impact on the toughness and ductility characteristics of the welded joints, and influences the technological and other properties of the metal [20, 21].

TECHNOLOGIES OF ADDING MODIFIERS

Different modification technologies are traditionally used in metallurgical production, namely: chemical, electrochemical and physical (microcoolants) and combined, by adding modifiers into the solution, or applying different physical (mechanical) methods to the solution. Widely applied among the modification technologies are the chemical methods, using the chemical state of the modifiers for modifying the metal structure. This is achieved by adding powders of different chemical compounds to the liquid pool in the form of flux-cored wires, bands, aerosols or predeposition of powder onto the surface (adhesion bonding). This approach allows refining the metal structure and forming new strengthening phases, which, in its turn, promotes an improvement of its service properties [22, 23].

The physical impact methods having a modifying effect include the following: ultrasonic treatment, high-frequency peening, temperature-time treatment, superposition of an electromagnetic field on the melt, etc. Of great interest are the processes related to pressure application to the metal of crystallizing castings. In particular, in the technological schemes of casting with alloy crystallization under pressure (die casting — DC) the pressure applied to the melt during solidification, has a significant influence on the nature of crystallization.

At present there are few references in literature to the use of combined technologies of adding modifiers, which influence the metal structure components and thus improve its performance [24].

Among the modern methods of adding modifiers to cast iron and steel melt, the following should be singled out: method of processing with balls of the matching master alloys; submerged block method; processing with lump ferroalloys, processing by powderlike wire and blowing with powderlike ferroalloys.

Application of combined ultrasonic methods of welded joint surface modification using nanosized modifiers can improve the modification effectiveness. Reduction of the dimensions of modifying particles leads to reduction of mean dimensions of weld metal grains and stress intensity factor [24]. Use of nanodispersed particles having higher specific surface energy increases the probability of chemical interaction between the particles and the metal, leading to formation of strong bonds and more effective refinement of the deposited metal structure (Figure 2).

Similar to metallurgical production, the methods of modification of welded joint metal can also be divided into three main groups: chemical (addition of modifiers), physical (application of external physical

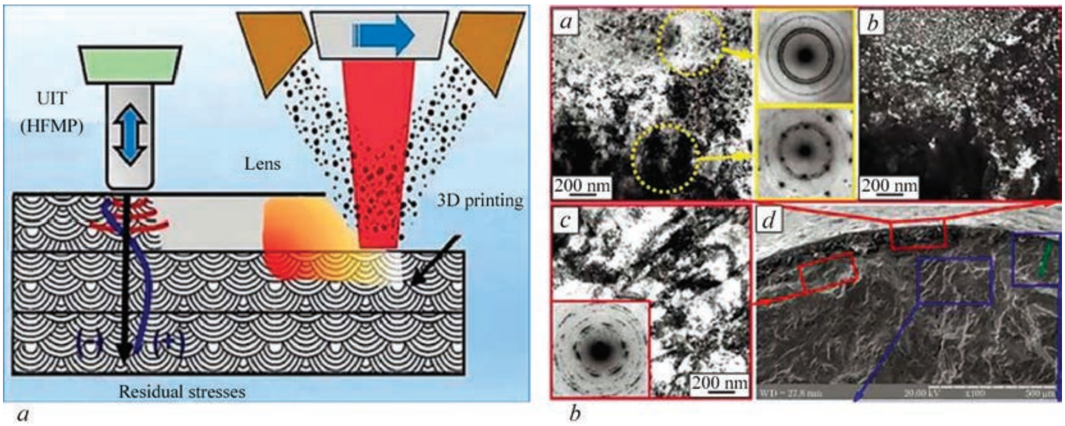

Figure 2. Scheme of combined application of ultrasonic methods of surface modification: *a* — ultrasonic impact treatment (HFMP); *b* — surface microstructure and X-ray patterns of the studied regions [24]

impacts) and combined [14], while all the modifiers can be divided into three classes, depending on the manner of their influence on weld metal crystallization [22].

Modifiers of the first kind improve the wettability of one alloy component by another one, i.e. they reduce the energy of surface tension on the interface, thus facilitating the nucleation of the new solid phase, contacting the liquid (Figure 3). Modifiers of the 2nd kind are directly the crystallization nuclei. They, however, can be such rather conditionally — in the case, when the melt temperature is so close to that of modifiers solidification that it will be insufficient for melting the modifiers added to the liquid pool. Modifiers of the 3rd kind (inoculators) change the weld metal structure by lowering the temperature of overheating of the liquid metal being solidified [14]. The higher cooling rate increases the crystallization rate and promotes an increase in development of the liquation processes which is favourable for the weld metal microstructure.

Moreover, the modifiers can be divided into two types: those, which do not change the surface properties of the crystallizing phase, and those changing the surface tension on the melt-particle interface [14]. Additives of the second type are usually called surface-active, and they are selectively concentrated on the surface of the crystals (dendrites). Surfactants are capable of creating a continuous adsorption layer. It means that at practical absence of surface-active modifier solubility in the solid phase a shell of a liquid enriched in modifier elements forms around it [14].

Complex modifiers are a system consisting of two and more modifiers of the same or different types of elements from those given above. Such a complex application of modifiers allows significantly decreasing the liquation processes in the weld metal and the HAZ, which will lead to a more uniform distribution of the alloying elements, lowering of concentration gradients and homogenizing of the properties (Figure 4) [25]. The effect of such modifiers, depending on their type, is usually manifested in a more inten-

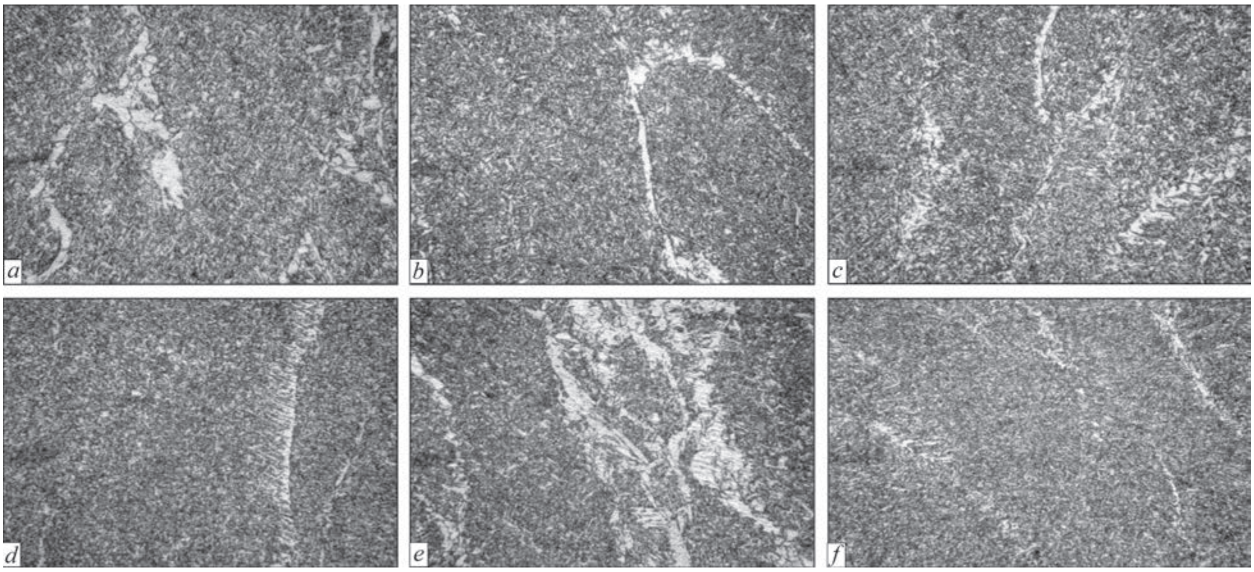

Figure 3. Microstructure (×500) of weld metal of HSLA steel 14KhGNDTs with modifier addition: *a* —without addition; *b* — MgO; *c* — ZrO_2; *d* — TiO_2; *e* — Al_2O_3; *f* — SiC

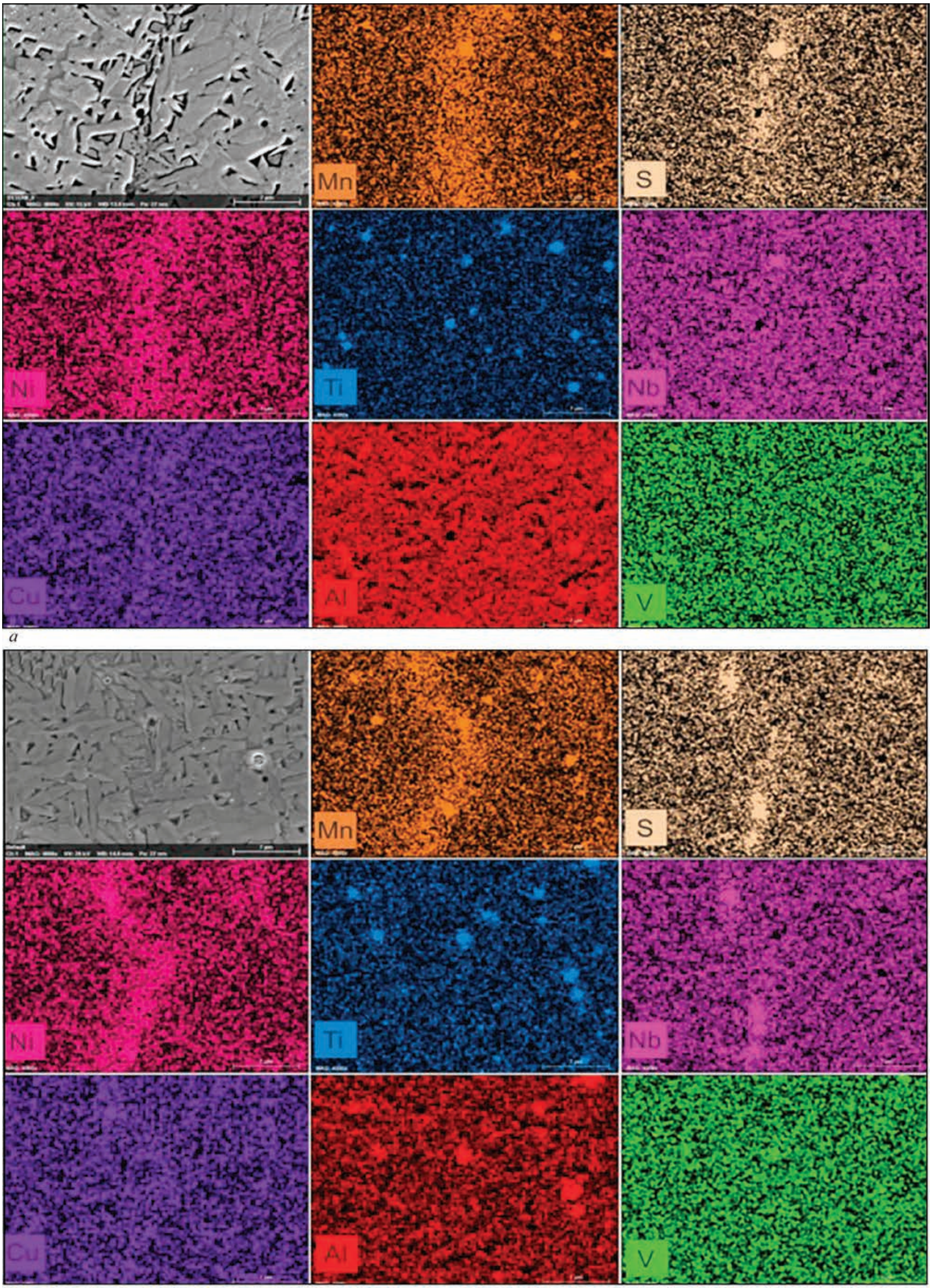

Figure 4. Influence of modifying additives (Nb, V, Ti, Ni) on alloying element liquation in weld metal of HSLA steels: *a* — A572 G50; *b* — A656 G80 steel [25]

sive and complex way, simultaneously influencing the mechanical, technological and service properties of the weld metal [26].

The physical methods of modification include those, which are based on the influence of physical processes on the processes of crystallization and formation of the weld metal structure. This is, in particular, application of vibrations during welding, pulsed application of energy from the heat source; pulsed feed of electrode or filler wire; application of sources with welding current modulation, as well as in a number of cases use of additional heat sources influencing the HAZ close to the weld fusion line; external electromagnetic influence, etc. [14, 27]. In work [28] the authors used a combined method of treatment of welded joints of 40Kh steel. The nitride layer was applied by plasma nitriding, and then treated by a scanning electron beam. It was found that hardness (850 *HV*) increased more than three times, compared to the initial material. Application of this combined method (PN + EBT) improves the steel wear resistance at abrasive wear by more than two times, compared to plasma nitriding.

INFLUENCE OF MODIFIERS ON THE STRUCTURE AND PROPERTIES OF WELD METAL OF HSLA STEELS

Flux-cored wires with different degree of filling with particles of oxides, carbides and nitrides of predominantly refractory metals are often used as modifiers in welding HSLA steels. The following compounds are often used for these purposes: TiC, SiC, NbC, TiO_2, Al_2O_3, ZrO_2, MgO, TiN, TiB. Appearance of modifier powders is given in Figure 5.

In work [29] it was established that carbide modifiers (TiC, SiC, NbC) influence the transformation kinetics and formation of secondary crystalline structure due to their dissolution and change of the metal chemical composition, while oxide modifiers (TiO_2, Al_2O_3, ZrO_2, MgO) and modifiers based on titanium compounds dissolve and precipitate on the surface of nonmetallic inclusions, as well as in the form of individual nonmetallic inclusions and phase precipitates, influencing structure formation and mechanical properties of the modified weld metal.

It was shown [29] that at modification by particles based on titanium compounds new nonmetallic inclusions are formed, appearing inside the weld metal grains with high dislocation density (10^{-10}–10^{-11} cm^{-2}) around the inclusions, which has a negative impact on the ductility indices of the welded joint metal.

Oxide-based modifiers have a complex impact on structure formation processes and they can be recommended for industrial applications. Proceeding from the obtained results the authors ranged by the degree of modifiers influence on weld metal strength and ductility: ZrO_2–MgO–TiO_2–Al_2O_3. It was found that modification by ZrO_2 powders should be recommended to improve the ductility and impact toughness, and Al_2O_3 powders should be used for higher strength.

In work [30] it was established that modification with ZrO_2 and MgO particles leads to a certain increase of the temperatures of the beginning of transformation for cooling rates below 17 °C/s. Modification by TiC, SiC, NbC, TiO_2, Al_2O_2 and TiN particles leads to lowering of critical transformation temperatures. Modification by carbide modifiers and TiN leads to formation of a pronounced martensite phase at dilatometric and metallographic investigations. The highest martensite content and the highest values of metal microhardness were produced for samples modified by TiN particles.

Dependence of transformation temperature on the cooling rate demonstrates a lowering of the transformation temperature for all the studied samples. It should be noted that modification by ZrO_2 and MgO

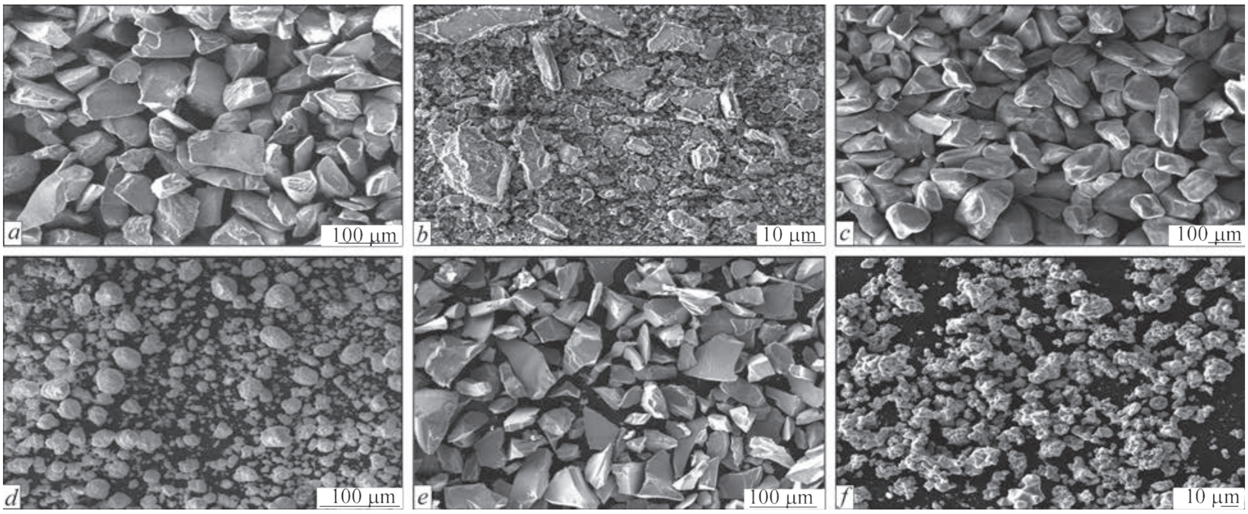

Figure 5. Appearance of modifier powders: *a* — Al_2O_3; *b* — MgO; *c* — TiO_2; *d* — ZrO_2; *e* — SiC; *f* — TiC

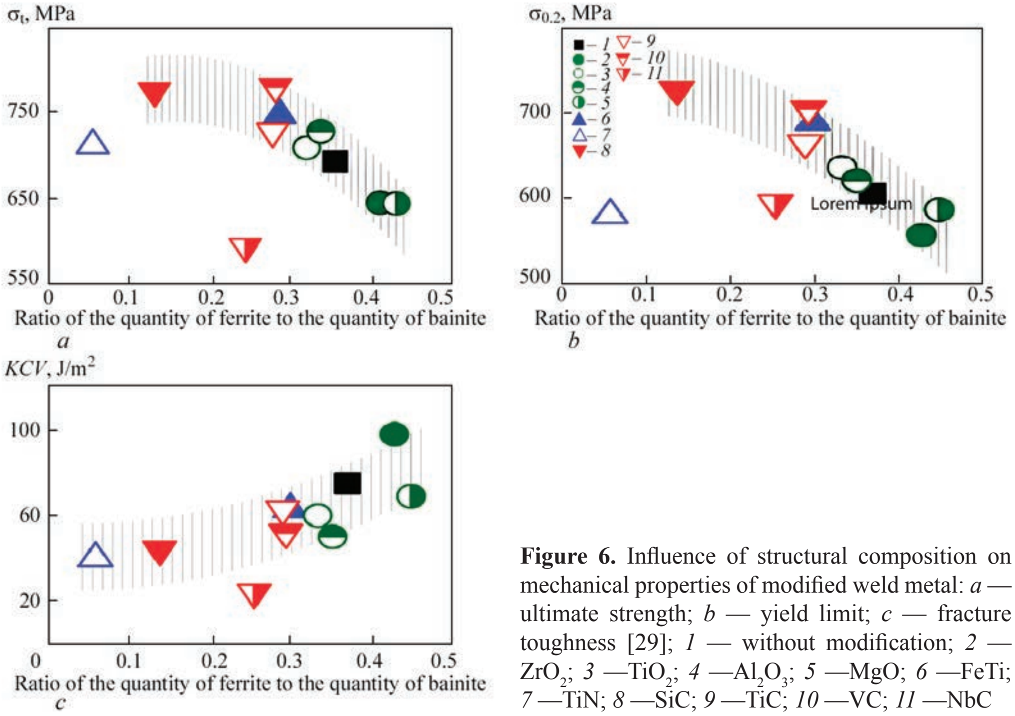

Figure 6. Influence of structural composition on mechanical properties of modified weld metal: *a* — ultimate strength; *b* — yield limit; *c* — fracture toughness [29]; *1* — without modification; *2* — ZrO_2; *3* —TiO_2; *4* —Al_2O_3; *5* —MgO; *6* —FeTi; *7* —TiN; *8* —SiC; *9* —TiC; *10* —VC; *11* —NbC

particles leads to improvement in the transformation temperature by 50–75 °C, and on the whole the values of transformation temperature for MgO, ZrO_2, TiO_2, Al_2O_3 oxide modifiers are higher than those for SiC, VC, NbC carbide particles. The lowest temperature transformation values are observed for a sample modified by TiN titanium nitride [30].

Influence of modifying particle type on the mechanical properties of weld metal of HSLA steels (Figure 6) shows a lowering of strength and increasing of ductility characteristics at increase of the ratio of the quantity of ferrite phase to that of bainite phase.

At the same time, an opposite dependence was established at weld metal modification by TiN and NbC particles, which was accounted for by the presence of a martensite phase in the structure of weld metal of these samples, as a result of dissolution of carbide-forming modifiers.

NANOMODIFICATION. ADVANTAGES AND DISADVANTAGES

Application of finer particles or powders of refractory metals became a further development of the technology of metal structure modification. Use of such particles of less than 100 nm size on the one hand allows controlling the metal structure already at the micro- or even atomic level, and on the other hand it requires development of special technologies and equipment for their realization. Application of such nanoparticles allows more thoroughly influencing the growth of primary grains during liquid metal crystallization; controlling the grain-boundary processes; forming a complex subgrain microstructure; influencing the distribution of dislocations, impurities and level of chemical heterogeneity, i.e. improving the metal structure in some way and increasing its metal properties.

At the same time, scientists are faced serious difficulties of both technological and research nature. From the view point of technology, equipment should be developed for adding nanopowders into the weld pool and for preventing their dissolution at the stage of weld metal crystallization. Their dissolution has to be prevented that is a more complex task, compared to traditional particles of larger size, used for modification. Moreover, a uniform distribution of the nanoparticles should be ensured, disregarding their tendency to combine — to form clusters and aggregations.

Therefore, the majority of the works, devoted to welded joint modification by nanoparticles are devoted to solid-phase welding, i.e. welding, where no melting occurs. Now, in those works, where fusion welding methods (TIG, MIG/MAG) are used, the nanoparticles solubility is almost not controlled.

In work [29] an attempt was made to assess the change in nanoparticle size during welding of HSLA steel. Analysis of the distribution of particles and size of inclusions in the metal of welds without modifiers and with their application reveals a reduction of the fraction of fine inclusions, and increase of the fraction of inclusions large than 0.36 μm.

An important technological aspect of nanomodification is addition of nanoparticles to the weld pool. The high specific surface energy of the nanoparticles associated with a large overall surface area, leads to nonuniform distribution of the nanoparticles (Fig-

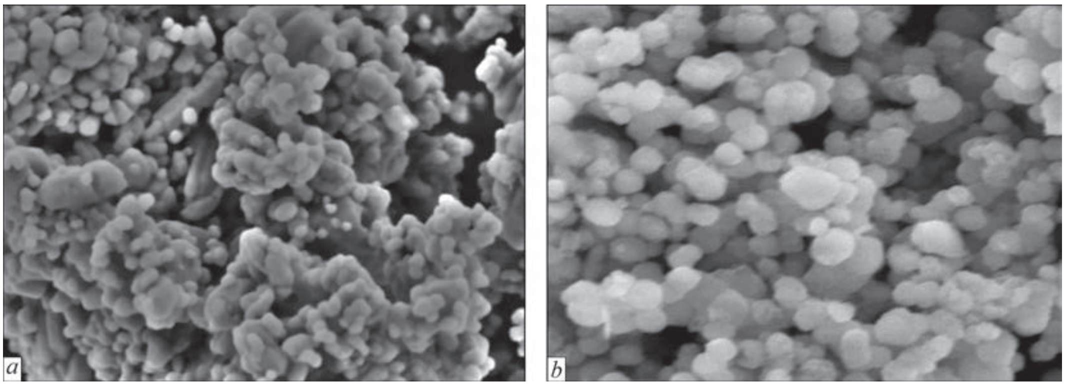

Figure 7. General appearance of nanopowders: *a* — Al_2O_3; *b* — TiO_2 (×100000)

ure 7) [31, 32]. They most often coalesce, forming conglomerates or clusters of nanoparticles, or precipitate at the bottom of the weld pool. Moreover, in welding processes the temperature in the zone of heat source impact is higher than the melting temperature of many refractory nanodispersed compounds causing their dissociation and further dissolution of the products in the weld pool melt [33].

In work [15] the influence of titanium-containing nanoparticles on crystallization of acicular ferrite and mechanical properties of metals for multipass arc welding was studied. In the study particle dispersion was conducted, using ultrasonic treatment. However, achievement of a uniform distribution of nanoparticles in liquid glass for further coating of the electrodes requires treatment for 6 hours that is not practical in serial production. The authors also determined that the percentage of acicular ferrite in the weld metal becomes higher with increase of the amount of nanoparticles of TiO_2 titanium oxide in the electrode coating.

In work [34] the influence of TiO, SiO_2, Al_2O_3 and Mn_2O_3 nanoparticles on the features of destruction of Charpy impact V-notch specimens produced by submerged-arc welding was studied. Increase of strength and impact toughness of the welds as a result of greater surface density of acicular ferrite at decrease of the lath thickness as a result of modification by TiO_2, SiO_2, Al_2O_3 or Mn_2O_3 nanoparticles was found.

In work [35] SiC and TiO_2 nanoparticles were used at friction stir welding of AA7075 and AA2024 aluminium alloys. It was established that the nanoparticles are dispersed in the welding one, forming a refined microstructure and preventing formation of harmful defects. This distribution improves the load-carrying capacity, effectively increasing the tensile strength of the joint. The nanoparticles promote a more uniform stress distribution and slow down crack initiation and propagation.

Work [36] is a study of the influence of SiO_2 nanoparticles, graphene nanoplatelets (Gnps) and biocoal, added to the weld pool at FSW of AISI-SAE 1010 steel and CDA 101 copper. It was found that additions of a considerable quantity of nanoparticles resulted in undesirable values of the strength intensity factor. At the same time, the microstructure of the weld with application of nanoparticles was quite favourable. The grains in the HAZ and TMAZ were considerably refined, due to application of nanoparticles. The result showed that biocoal nanoparticles obtained naturally have a potential to replace expensive nanofillers in metal welding.

Cracking during weld pool solidification was a serious problem in fusion welding of high-strength and high alloys for many years. It has been established recently that application of TiC nanoparticles as filler materials is an effective method of preventing cracks at solidification during TIG welding of sheet aluminium alloy AA7075. Experimental results showed that filler metal with TiC nanoparticles effectively prevents cracks at crystallization. Evaluation of microstructure reveals an equiaxed morphology of the grains in the fusion zones [37].

Thus, application of nanomodification in welding offers a number of advantages. First, this is structure improvement: nanomodifiers allow producing a more dispersed structure in the weld metal, and under appropriate conditions reaching a more homogeneous structure, reducing its defectiveness, lowering the level of residual hydrogen, improving the brittle fracture resistance, and reducing porosity. Secondly, this is increase of mechanical characteristics: during primary crystallization the nanoparticles will slow down the growth of crystallites, concentrating predominantly on their boundaries, and this will lead to refinement of the secondary microstructure, which will promote an increase of hardness, strength, and, most importantly, impact toughness at negative test temperatures. Thirdly, this is improvement of the weld metal resistance to the influence of the environment: nanoparticles can improve the weld metal resistance to oxidation, corrosion and other aggressive factors, acting under extreme conditions.

CONCLUSIONS

1. Performed analysis of literature sources showed that modification and microalloying of the metal of welds by feeding flux-cored wire with dispersed particles of oxide compounds is a promising technological measure of controlling the structure and improving the mechanical properties of weld metal of HSLA steels, which can be used under production conditions.

2. In modern modification technologies, application of refractory chemical compounds of various elements is designed for active regulation of primary crystallization processes, change of the degree of the solidifying phase dispersity and formation of a fine secondary structure.

3. Nanomodification of weld metal of HSLA steels and other alloys can be used with success for different welding methods (TIG, MIG/MAG, FSW) which allows significantly influencing the weld metal structure, refining both the primary and secondary structure, reducing the grain size, lowering liquation and improving their functional characteristics of strength, ductility, toughness and wear resistance.

REFERENCES

1. Morrison, W. (2000) Past and future development of HSLA steels. In: *Proc. of HSLA Steels, 30 October – 2 November 2000, Xi'an, China, Beijing*, 11–19.
2. Golovko, V.V., Kostin, V.A., Zhukov,V.V., Pribitko, I.A. (2010) Influence of manganese and titanium alloying on peculiarities of austenite decomposition in low-alloyed weld metal. *Vestnik Chernig. GTU,* **45**, 125–133 [in Russian].
3. Suzuki, T., Inoue, J., Koseki, T. (2008) Effect of oxides and their volume fraction on intragranular ferrite formation in steel. Trends in Welding Research. In: *Proc. of 8th Inter. Conf., June 1–6, 2008, Callaway Gardens Resort, Pine Mountain, Georgia, USA*, 292–296.
4. Goldshtejn, Ya.E., Mizin, V.G. (1986) *Modification and microalloying of cast iron and steel*. Moscow, Metallurgiya [in Russian].
5. Kalinin, N.A., Shumilov, A.A., Bilonik, I.M. (2012) Analysis of possibility of ultradispersed particle application for modification of metal in electroslag surfacing with flux-cored electrode. *Metalurgiya: Zbirnyk Naukovykh Prats,* 26(**1**), 35–42 [in Russian].
6. Trotsan, A.I., Kaverinskiy, V.V., Brodetskyi, I.L., Karlikova, Ya.P. (2011) Modification of melt by dispersed particles alloying for their size distribution. *Visnyk PDTU, Seriya Tekhnichni Nauky,* **22**, 144–150 [in Russian].
7. Shash, A.M., El-Fawkhry, K., Rahman, Sh.A.A.E. et al. (2017) Improvement of mechanical properties and structure modifications of low carbon steel by inoculations with nano-size silicon nitride. *J. of NanoResearch*, **47**, 24–32. DOI: https://doi.org/10.4028/www.scientific.net/JNanoR.47.24
8. Grigorenko, G.M., Kostin, V.A., Golovko, V.V. et al. (2015) Influence of nanopowder inoculators on the structure and properties of cast metal of high-strength low-alloyed steels. *Sovrem. Elektrometall.*, **2**, 32–41. http://nbuv.gov.ua/UJRN/sovele_2015_2_7
9. Grigorenko, G.M., Kostin, V.A., Golovko, V.W., Zukov, V.W. (2016) Effect of nanoparticles on the structure and properties of welds made of high strength low-alloy steels. *Biuletyn Instytutu Spawalnictwa*, **6**, 65–69. DOI: http://dx.doi.org/10.17729/ebis.2016.6/9
10. Nejmark, V.E. (1977) *Modified steel ingot.* Moscow, Metallurgiya [in Russian].
11. Holovko, V.V., Yermolenko, D.Yu., Stepanyuk, S.M. et al. (2020) Influence of introduction of refractory particles into welding pool on structure and properties of weld metal. *The Paton Welding J.*, **8**, 8–14. DOI: https://doi.org/10.37434/tpwj2020.08.01
12. Bhadeshia, H.K.D.H. (2001) *Bainite in steels — transformation, microstructure and properties*. 2nd Ed. London, Institute of Materials Communication Ltd.
13. Manyak, N.A., Manyak, L.K. (2002) Influence of boron on structure and toughness of low-alloyed steel. *Metall i Litiyo Ukrainy,* **5–6**, 23–25 [in Ukrainian].
14. Babinets, A.A., Ryabtsev, I.O. (2021) Classification of methods of modification and microalloying of deposited metal (Review). *The Paton Welding J.*, **9**, 2–8. DOI: https://doi.org/10.37434/tpwj2021.09.01
15. Lobanov, L.M., Syzonenko, O.M., Holovko, V.V. et al. (2021) Pulsed-discharge treatment of the Al–Ti–C system modifier. *The Paton Welding J.*, **5**, 24–29. DOI: https://doi.org/10.37434/tpwj2021.05.04
16. Aleshin, N.P., Grigor'ev, M.V., Kobernik, N.V. et al. (2018) Modification of weld metal with tungsten carbide and titanium nitride nanoparticles in twin submerged arc welding. *High Energy Chemistry*, 52(**5**), 440–445. DOI: https://doi.org/10.1134/S0018143918050028
17. Tsekhmistrenko, S.I., Bityutskyi, V.S., Tsekhmistrenko, O.S. et al. (2022) Application of nanoparticles. In: *Ecological biotechnologies of "green" synthesis of nanoparticles of metals, metal oxides, metalloids and their application.* Bila Tserkva, BNAU, 167–249 [in Ukrainian].
18. Novikov, S. (2018) *Influence of TiC nanopowder on operational characteristics of deposited layer.* In: Syn. of Thesis for Master Degree. Kyiv [in Ukrainian].
19. Shim, J.-H., Cho, Y.W., Chung, S.H. et al. (1999) Nucleation of intragranular ferrite at Ti_2O_3 particle in low carbon steel. *Acta Materialia*, **47**, 2751–2760.
20. Cuixin Chen, Haitao Xue, Huifen Peng et al. (2014) Inclusions and microstructure of steel weld deposits with nanosize titanium oxide addition. *J. of Nanomaterials*, **2014**, 1–7. DOI: https://doi.org/10.1155/2014/138750
21. Seliverstov, V., Dotsenko, Yu., Dotsenko, N. (2016) Prospects of application of complex technological solutions for improvement of mechanical properties of Al-Si casting alloys. In: *Proc. of Conf. Titan-2016 on Production and Use in Aircraft Manufacturing,* 23–25.
22. Dotsenko, Yu.V., Selivyorstov, V.Yu., Dotsenko, N.V. et al. (2015) Study of influence of modern complex technology on properties of castings of Al–Si system alloys. *Young Scientist*, 1(**16**), 13–16.
23. Aikin, M., Shalomeev, V., Lukyanenko, O. (2021) Study of influence of cooling high speeds on structure and properties of Mg–Zr–Nd alloy system. *Innovative Materials and Technologies in Metallurgy and Mechanical Eng.*, **1**, 25–33. DOI: https://doi.org/10.15588/1607-6885-2021-1-4
24. Mordyuk, B.M. (2022) Ultrasonic methods of surface modification and diagnostics of advanced metallic materials. *Visnyk NANU*, **4**, 42–53 [in Ukrainian]. DOI: http://dx.doi.org/10.15407/visn2022.04.042
25. Mohammad Saadati, Amir Keyvan Edalat Nobarzad, Mohammad Jahazi (2019) On the hot cracking of HSLA steel welds: Role of epitaxial growth and HAZ grain size. *J. of Manufac-*

turing Proc., **41**, 242–251. DOI: https://doi.org/10.1016/j.jmapro.2019.03.032
26. Xu, H. et al. (2024) New method for the production of medium-Mn steel with micro-segregation bands induced by sub-rapid solidification. *The Minerals, Metals & Materials Series*, *Cham*. DOI: https://doi.org/10.1007/978-3-031-50304-7_22
27. Sidun, K.Yu. (2024) *Technological ensuring surface integrity and improvement of corrosion resistance of die steel by combined laser-ultrasonic surface treatment*: Syn. of Thesis for Master Degree. Kyiv [in Ukrainian].
28. Razmyshlyaev, A.D., Ageeva, M.V. (2018) On mechanism of weld metal structure refinement in arc welding under action of magnetic fields (Review). *The Paton Welding J*., **3**, 25–28. DOI: https://doi.org/10.15407/tpwj2018.03.05
29. Zhukov, V.V. (2021) *Peculiarities of structure and mechanical properties of 14KhGNDTs steel welds modified by dispersed particles of carbides, oxides and titanium-based compounds*: Syn. of Thesis for Cand. of Tekh. Sci. Degree, Kyiv, PWI [in Ukrainian].
30. Kostin, V.A., Zhukov, V.V., Berdnikova, O.M. et al. (2021) Effect of modification of weld metal of high-strength low-alloy steels on their structure and properties. *The Paton Welding J*., **5**, 57–64. DOI: https://doi.org/10.37434/tpwj2021.05.10
31. Morozov, V.P. (2006) Peculiarities of process of primary structures formation of welds of different system aluminium alloys. *Izv. Vuzov, Mashinostroenie*, **9**, 51–64 [in Russian].
32. Aftandilyants, E. (2021) Effect of alloying and modification on properties of heat-resistant steel castings. In: *Proc. of Sci-Pract. Online Conf. on Current Problems and Prospects of Development of Mechanical Engineering in Ukraine. National Un-ty of Bioresources and Nature Management, 23 September, 2021. Kyiv* [in Ukrainian].
33. Kuznetsov, V.D., Smyrnov, I.V., Stepanov, D.V., Shapovalov, K.P. (2013) Effect of modification by oxide nanoparticles on structure formation of welds of low-alloyed steels. *Mizhvuzivskyi Zb. Naukovi Notatky,* Lutsk, 61–69 [in Ukrainian]
34. A Jiménez-Jiménez et al. (2021) CVN impact energy and fracture characteristics correlations with different oxide nanoparticles improving submerged arc welds. *Materials Research Express*, 8(**1**), 2053–1591. DOI: https://doi.org/10.1088/2053-1591/abdaf2
35. Mouria, P.K., Singari, R.M., Wattal, R. (2023) Microstructural and mechanical response of SiC and TiO_2 particles reinforced friction stir welded AA7075 and AA2024. *Inter. J. Interact. Des. Manuf*., **3**, 1331–1343. DOI: https://doi.org/10.1007/s12008-023-01667-0
36. Giridharan, K., Sevvel, P., Ramadoss, R., Stalin, B. (2022) Stalin friction stir processing of nanofiller assisted AISI 1010 steel-CDA 101 copper dissimilar welds: A strength factor approach. *Metall. Res. Technol*., 119(**5**), 505. DOI: https://doi.org/10.1051/metal/2022065
37. Abdollahi, A., Nganbe, M., Kabir, A.S. (2023) Fusion weldability of Al7075 sheets with TiC nanoparticle-enhanced filler metal with different welding parameters. In: *Proc. of 62nd Conf. on Metallurgists, COM 2023*. Springer, Cham. DOI: https://doi.org/10.1007/978-3-031-38141-6_55

ORCID

M.P. Reminnyi: 0009-0004-1786-2560,
V.A. Kostin: 0000-0002-2677-4667,
V.V. Zhukov: 0000-0002-3358-8491

CONFLICT OF INTEREST

The Authors declare no conflict of interest

CORRESPONDING AUTHOR

V.A. Kostin
E.O. Paton Electric Welding Institute of the NASU
11 Kazymyr Malevych Str., 03150, Kyiv, Ukraine
E-mail: valerykkos@gmail.com

SUGGESTED CITATION

M.P. Reminnyi, V.A. Kostin, V.V. Zhukov (2025) Modification and microalloying of the metal of welds on HSLA steels produced by fusion welding method (Review). *The Paton Welding J*., **1**, 40–49.
DOI: https://doi.org/10.37434/tpwj2025.01.07

JOURNAL HOME PAGE

https://patonpublishinghouse.com/eng/journals/tpwj

Received: 03.09.2024
Received in revised form: 02.10.2024
Accepted: 30.01.2025

ELECTRON BEAM PRODUCTION OF HARD ALLOY TOOLS

Having combined the expertise of the E.O. Paton Electric Welding Institute and NTUU “Sikorsky Kyiv Polytechnic Institute, the “PlasmaTec” Company founded an R&D Center in 2018. The objective of the Center is creation of competitive innovative developments and technological solutions to provide the industry with fundamentally new production methods. The technological core of the Center is material processing with a high-energy electron beam in electron beam remelting units. The potential and R&D resources of the Center allow conducting a full range of work, including:

- performance of scientific research;
- product design and forecasting their operating life;
- individual development of technologies for hard alloy part production.

D — 31 mm
d — 22 mm
H — 14 mm

R&D Center Mission

Ensure the best quality and the longest service life, compared to similar steel parts.

D — 26 mm
d — 18 mm
H — 20 mm

R&D Center advantages

D — 82 mm
d — 62 mm
H — 24.5 mm

- technology of a complete cycle of secondary raw material recycling and manufacturing new parts based on WC–Co hard alloys;
- our own research and production laboratory ensuring control of the process of technology development and production at each stage;
- high level specialized expertise in electron beam technologies: welding, heat treatment, sintering, coating.

D — 56 mm
d — 28 mm
H — 45 mm

Parts produced on a regular basis

- hard-alloy rollers for wire winding machines:
- metallurgical guide rollers and scale breakers for wire rolling mills (material WC–Co);
- rollers with WC–Co carbide inserts for wire drawing mills.

We develop all the solutions individually in accordance with the customer requirements
https://plasmatec-weld.com.ua/